

Dissertation zur Erlangung des Doktorgrades der Fakultät für
Chemie und Pharmazie der Ludwig-Maximilians-Universität München

Structural basis of the mitochondrial
voltage-dependent anion channel VDAC I

Thomas Meins

aus München

2008

Erklärung

Diese Dissertation wurde im Sinne von §13 Abs. 3 bzw. 4 der Promotionsordnung vom 29. Januar 1998 von Herrn Prof. Dr. Dieter Oesterhelt betreut.

Ehrenwörtliche Versicherung

Diese Dissertation wurde selbstständig, ohne unerlaubte Hilfe erarbeitet.

München, am 08. September 2008

.....
Thomas Meins

Dissertation eingereicht am: 08.09.2008

1. Gutachter: Prof. Dr. Dieter Oesterhelt

2. Gutachter: Prof. Dr. Karl-Peter Hopfner

Mündliche Prüfung am: 27.10.2008

Meinen Eltern & Verena

TABLE OF CONTENTS

1 Summary.....	6
2 Introduction.....	7
2.1 Mitochondrial structure and function.....	7
2.2 The mitochondrial outer membrane	8
2.3 The voltage dependent anion channel.....	8
2.3.1 General function of VDAC.....	9
2.3.2 The different isoforms of the VDAC.....	10
2.3.3 Conductance, voltage dependency and ion selectivity of the VDAC.....	10
2.3.4 The general structure of the VDAC.....	12
2.3.5 Fold and architecture of bacterial β -barrel membrane proteins	15
2.3.6 Evidence for a β -barrel fold of VDAC	16
2.3.7 Model of the proposed VDAC structure and its gating mechanism.....	17
2.3.8 The role of VDAC in mitochondrial complexes.....	19
2.3.8.1 Involvement of VDAC in complexes of the energy metabolism.....	20
2.3.8.2 Involvement of VDAC in the mitochondrial phase of apoptosis.....	20
2.4 Conceptual formulation.....	22
3 Materials and methods.....	24
3.1 Materials.....	24
3.1.1 General Instruments:.....	24
3.1.2 Consumables.....	24
3.1.3 Kit systems.....	25
3.1.4 Fine Chemicals.....	25
3.2 Strains and vectors	26
3.2.1 Strains.....	26
3.2.2 Vectors.....	26
3.3 Growth Media.....	26
3.3.1 Antibiotics.....	26
3.3.2 LB agar plates.....	27
3.3.3 LB broth.....	27
3.3.4 TB broth.....	27
3.3.5 Minimal medium.....	27
3.3.6 Algal extract supplemented media (AES media)	28

3.4 General Molecular Biological Techniques.....	29
3.4.1 Preparation of electro-competent <i>E. coli</i> cells.....	29
3.4.2 Transformation of <i>E. coli</i> cells.....	30
3.4.3 Determination of DNA concentrations.....	30
3.4.4 Plasmid amplification	30
3.4.5 Isolation of plasmid DNA from <i>E. coli</i> cells.....	31
3.4.6 Analysis of plasmid DNA by agarose gel electrophoresis.....	31
3.4.7 Sequencing of PDS56/RBSII-VDACIHis.....	31
3.4.8 Site directed mutagenesis of HVDAC1	32
3.4.9 Preparation of <i>E. coli</i> DL39 [prep4].....	34
3.5 Protein expression and purification.....	34
3.5.1 Heterologous expression of HVDAC1 in <i>E. coli</i>	34
3.5.1.1 Overproduction of HVDAC1 in <i>E. coli</i> M15 [prep4].....	34
3.5.1.2 Overproduction of selenomethionine labelled HVDAC1 in <i>E. coli</i> M15 [prep4].....	34
3.5.1.3 Overproduction of ² H, ¹⁵ N and ¹³ C labelled HVDAC1 in <i>E. coli</i> M15 [prep4].....	34
3.5.1.4 Overproduction of selective amino acid labelled HVDAC1 <i>E. coli</i> in DL39 [prep4].....	35
3.5.2 Purification and refolding of HVDAC1 inclusion bodies.....	35
3.5.2.1 Purification of HVDAC1 inclusion bodies.....	35
3.5.2.2 Refolding of denatured HVDAC1.....	36
3.5.3 Purification of refolded HVDAC1 for NMR investigations.....	36
3.5.3.1 Preparation of HVDAC1 NMR samples.....	36
3.5.3.2 MTSL-labeling of HVDAC1 NMR samples.....	37
3.5.4 Preparation of refolded HVDAC1 for crystallisation.....	37
3.5.4.1 Purification of refolded HVDAC1 for crystallisation trials.....	37
3.5.4.2 Detergent exchange.....	37
3.5.4.3 Crystallisation of HVDAC1.....	38
3.5.5 Overproduction and purification of mouse His6-BID	39
3.5.5.1 Overproduction of mouse His6-BID in <i>E. coli</i> BL21 (DE3)-RIPL.....	39
3.5.5.2 Overproduction of ² H and ¹⁵ N labelled His6-BID in <i>E. coli</i> BL21 (DE3)-RIPL.....	39
3.5.5.3 Purification of His6-BID.....	39
3.5.5.4 Cleavage of His6-BID by Caspase8.....	40
3.5.6 Purification of bovine adenosine nucleotide translocator (ANT) from bovine heart.....	40
3.5.6.1 Purification of mitochondria from bovine heart.....	40

3.5.6.2 Purification of BANT from bovine heart mitochondria.....	41
3.5.7 Further utilised proteins.....	41
3.6 Protein analytical methods.....	41
3.6.1 Determination of protein concentrations.....	41
3.6.2 SDS-Polyacrylamide gel-electrophoresis (SDS-PAGE) of proteins.....	42
3.6.3 N-terminal sequencing.....	42
3.6.4 Protein mass spectrometric analysis	42
3.6.4.1 High performance liquid chromatography/mass spectrometry (HPLC/ESI-MS).....	42
3.6.4.2 Peptide mass fingerprint analysis	43
3.6.5 Secondary structure determination by circular dichroism spectroscopy	43
3.6.6 Reconstitution of HVDAC1 in planar bilayer membranes and conductivity measurements....	43
3.6.7 Analysis of protein-protein interactions by chemical and light-induced crosslinking.....	44
3.6.7.1 Chemical crosslinking.....	44
3.6.7.2 Light-induced crosslinking.....	44
3.6.8 NMR spectroscopy.....	45
3.6.9 X-ray data collection and analysis.....	46
3.6.10 Alignments, secondary predictions and homology modelling.....	47
4 Results.....	48
4.1 Biochemical properties of HVDAC1.....	48
4.2 Overproduction, purification and refolding of HVDAC1.....	49
4.2.1 Overproduction of HVDAC1.....	49
4.2.2 Isolation of HVDAC1 inclusion bodies.....	50
4.2.3 Refolding of denatured HVDAC1	51
4.2.4 Purification of refolded HVDAC1 by Ni ²⁺ -affinity chromatography.....	52
4.3 Characterisation of refolded HVDAC1.....	53
4.3.1 Mass determination of HVDAC1.....	53
4.3.2 Evaluation of refolded HVDAC1 by circular dichroism (CD) spectroscopy.....	54
4.3.3 Voltage dependent conductance of HVDAC1.....	55
4.4 Structure determination of HVDAC1.....	57
4.4.1 Structure determination of HVDAC1 by NMR spectroscopy.....	57
4.4.1.1 Optimization of HVDAC1 NMR samples.....	57
4.4.1.2 Resonance assignment and secondary structure determination.....	59
4.4.1.3 NMR topology model of HVDAC1.....	64

4.4.1.4 Spatial position of the N-terminal α -helix	65
4.4.2 Structure determination of HVDAC1 by X-ray crystallography	66
4.4.2.1 Crystallisation of HVDAC1	66
4.4.2.2 Structure determination of HVDAC1.....	69
4.4.2.3 Overall dimensions of the barrel shaped structures.....	72
4.4.2.4 Density improvement by B-factor sharpening.....	73
4.4.2.5 Map interpretation	74
4.4.3 Combination of X-ray and NMR data	76
4.4.4 Topology of HVDAC1.....	77
4.5 Interaction between HVDAC1 other proteins and compounds.....	81
4.5.1 Preparation of mouse Bid and the bovine adenine nucleotide translocator.....	81
4.5.1.1 Expression and purification of mouse BID (mBid).....	81
4.5.1.2 Purification of the adenine nucleotide translocator (ANT) from heart mitochondria.....	82
4.5.2 Interaction between HVDAC1 and the Bcl-2 family proteins Bid, Bcl-XL and Bax.....	82
4.5.3 Interaction between HVDAC1, ANT and the N-terminal α -helix of hexokinase II.....	86
4.5.4 Interaction between HVDAC1 and small molecules.....	88
4.5.4.1 ADP-titration.....	88
4.5.4.2 Fluoxetine-titration.....	89
4.5.4.3 Calcium (II) chloride an gadolinium (III) chloride titration.....	89
5 Discussion.....	91
5.1 Overexpression and refolding of HVDAC1.....	92
5.2 Structure determination of HVDAC1.....	94
5.2.1 Determination of the 2D topology of HVDAC1 by NMR spectroscopy	94
5.2.2 Determination of the global HVDAC1 architecture by X-ray crystallography.....	96
5.2.3 Improved model interpretation by the integration of local and global structure information....	98
5.3 Structural basis of HVDAC1.....	98
5.3.1 The HVDAC1 architecture is common to all VDAC proteins.....	100
5.3.1.1 The secondary structural distribution is conserved across all VDAC proteins.....	100
5.3.1.2 The HVDAC1 structure in respect to the effects of charge altering point mutations	102
5.3.1.3 VDAC proteins exhibit a positively charged channel lining.....	103
5.3.1.4 A conserved indentation pattern is characteristic of all VDAC proteins.....	103
5.3.2 HVDAC1 reveals a common β -barrel fold.....	105
5.3.2.1 HVDAC1 retains the sidedness of bacterial b-barrel membrane proteins.....	105

5.3.2.2 HVDAC1 conserves the spatial distribution of specific amino acids along the surface	105
5.3.2.3 HVDAC1 is specifically adapted to the outer mitochondrial membrane.....	107
5.3.3 The structural design of HVDAC1 is reminiscent of the bacterial porin architecture.....	108
5.3.4 The alternative pore restriction seems to be attributed to the voltage dependent behavior..	109
5.3.5 HVDAC1 exhibits a comparatively large pore diameter.....	110
5.3.6 Oligomeric structure of HVDAC1.....	111
5.3.6.1 HVDAC1 dimerises via the β -barrel junction.....	111
5.3.6.2 Implications on the stability of HVDAC1.....	112
5.4 Interaction between VDAC1 pro- and anti-apoptotic proteins and hexokinase II.....	113
5.4.1 The signature pattern forms the structural scaffold for MOM targeting proteins.....	114
5.4.2 Bid and Bcl-XL target the porin signature pattern via an α -helical hairpin motif.....	115
5.4.3 The channel wall as a signal transferring element.....	118
5.4.4 Influence of the oligomeric state of HVDAC1.....	118
6 References.....	120
7 Abbreviations.....	128
8 Acknowledgement	129

1 Summary

The voltage-dependent anion channel, VDAC, is the major constitutive protein of the outer mitochondrial membrane. Owing to the ability to switch between anion and cation selective states in conductance measurements, this channel is referred to as voltage-dependent. Structurally, the channel has a bacterial origin by evolution and is functionally related to the bacterial porins. As such VDAC plays a decisive role for the metabolic flux across the the outer mitochondrial membrane. Beyond this function VDAC is described to interact with a growing number of proteins, most of which are involved in energy metabolism and the mitochondrial phase of apoptosis. Among these interactions, the most prominent concerns the interplay between VDAC and pro- and anti-apoptotic proteins like Bid and Bcl-XL in multicellular organisms. As a target of these proteins the channel is connected to a critical process known as mitochondrial outer membrane permeabilisation (MOMP) which is involved in the release of apoptogenic factors from the mitochondrial inter membrane space and hence inevitable cell death. Linked to this crucial stage of the apoptotic process, VDAC becomes a promising target to fight severe diseases including neurodegenerative disorders and of course cancer which have a dysfunction of the apoptotic program in common. Efforts concerning this matter led indeed to an encouraging set of VDAC targeting molecules the therapeutic efficacies of which currently have to prove true in clinical trials.

As a basis for a more thorough understanding of the functional role of VDAC this study set out to characterise the molecular architecture of the most prominent isoform from human, HVDAC1, by biophysical techniques including NMR and X-ray crystallography. Conjointly, the local information from NMR spectroscopy and the global information from X-ray crystallography led to the elucidation of an advanced three-dimensional model presenting a β -barrel architecture composed of 18 anti-parallel strands with an α -helix located horizontally midway within the pore. A bioinformatic analysis indicates that this architecture is common to all VDAC proteins. Subsequent interaction studies by NMR demonstrate that HVDAC1 offers the structural scaffold for the docking of cell death suppressing (hexokinase II, Bcl-XL) and cell death promoting (Bid) proteins to mitochondria, thereby regulating apoptotic events and energy metabolism. The fact that all of these proteins compete for the same binding site within a highly conserved signature pattern of HVDAC1 rationalises the inhibitory effects of HK II and Bcl-XL on Bid induced MOMP and apoptosis. The structural insights gained in the course of this study offer a novel perspective for our understanding of these processes and provide a starting point for structure-based lead design efforts in the future.

2 Introduction

2.1 Mitochondrial structure and function

Eukaryotic cells typically contain a variable number of mitochondria. These organelles are involved in numerous metabolic and cellular processes^[1]. Besides the citric acid cycle and the oxidative phosphorylation, these processes also include the urea cycle and the β -oxidation of fatty acids. Other reactions carried out and orchestrated are the biosynthesis of heme, several amino acids and vitamin cofactors, as well as the formation and export of iron-sulphur clusters^[2]. Beyond these metabolic functions, mitochondria are also involved in intracellular calcium signalling^[3], the programmed cell death^[4], and in case of their dysfunction in ageing^[5] and several diseases^[6].

Mitochondria are widely accepted to have originated from a single ancient endosymbiotic event. By this occasion, a prokaryotic ancestor, in all probability related to the α -proteobacterial subfamily *Rickettsiaceae*, became internalised by a amitochondriate (pro-eukaryotic) host^[7]. During evolution, a distinct gene transfer from the endosymbiont to the nucleus takes place and is suggested as been responsible for the transition from an autonomous endosymbiont to the present organelle^[8].

The organelle is compartmentalized by two membranes into four compartments. A smooth outer membrane (OMM) surrounds and isolate the organelle from the cytosol while the inner membrane (IMM) with several invaginations, called cristae, divides them further into the mitochondrial inter-membrane space (MIMS) and the matrix. The organization of the inner membrane was dissected in recent studies using improved electron microscopic and tomographic techniques^{[9][10]}. The images, obtained from rat liver and pancreas mitochondria, exemplify besides the outer membrane an inner boundary membrane which is connected by several tubular junctions to the cristae, thereby creating a distinction between the intermembrane and the intercrystal space (Fig.2-1a). This basic concept of the IMM is structurally dynamic with respect to cristae connection to each other or with the inner membrane and can be considerably vary among different organisms tissues or physiological conditions^[9].

The fact that many central processes in eukaryotic cells are functionally linked to this double membrane shielded organelle requires an interface between the mitochondrial compartment and the cytoplasm.

To achieve this intracellular exchange the two membranes include a variety of transport and receptor proteins^{[11][12][13]} as well as a specific subset of translocases involved in the import and assembly of mitochondrial proteins^[14].

2.2 The mitochondrial outer membrane

The outer mitochondrial membrane mainly consists of the phospholipids phosphatidylcholine, phosphatidylethanolamine, phosphatidylinositol and a variety of distinct integral and peripheral membrane proteins. Compared to the inner membrane the outer membrane contains minor amounts of cholesterol, almost no cardiolipin and shows a higher lipid to protein ratio^{[15][16]}.

Concerning the total mitochondrial protein, only about 5% are directed to the outer membrane whereas the inner membrane contains tissue specific a minimum of about 20%^[17]. With respect to around 1000 predicted mitochondrial proteins a set of at least 30 distinct ones were recently revealed by the outer membrane proteome analysis of the yeast *Neurospora crassa*^[18]. Functionally, these are divided into four groups involved in protein import, fission and fusion of the mitochondria, several biosynthetic pathways and the metabolic exchange. While the majority of the identified proteins belong to the first three groups there is only one that is responsible for the metabolite transport detected so far. This protein, known as mitochondrial porin or voltage dependent anion channel 1 (VDAC1), is with an average of 10^3 to 10^4 copies per μm^2 ^[19] one of the the most abundant proteins in the outer membrane (Fig.2-1b).

Recently obtained atomic force microscopy topographies revealed varying distributions of VDAC pores in different areas of the outer membranes of *S. cerevisiae*^[20]. Besides a few individual channels the vast majority of the channels are observed to be either clustered in small arrays or extensively assembled in densely but non-crystalline packed domains (Fig. 2-1 c-d). At several points within the ScVDAC arrays, the images also expose a variety of distinct protrusions which are most likely assumed as peripheral VDAC bound proteins^[20].

2.3 The voltage dependent anion channel

A channel forming protein which was implicated with the pore-like structures observed in electron micrographs of the outer mitochondrial membranes^[21] was described for the first time in 1979^[22]. Due to its voltage dependent selectivity behavior in conductance measurement this protein was termed as voltage dependent anion channel.

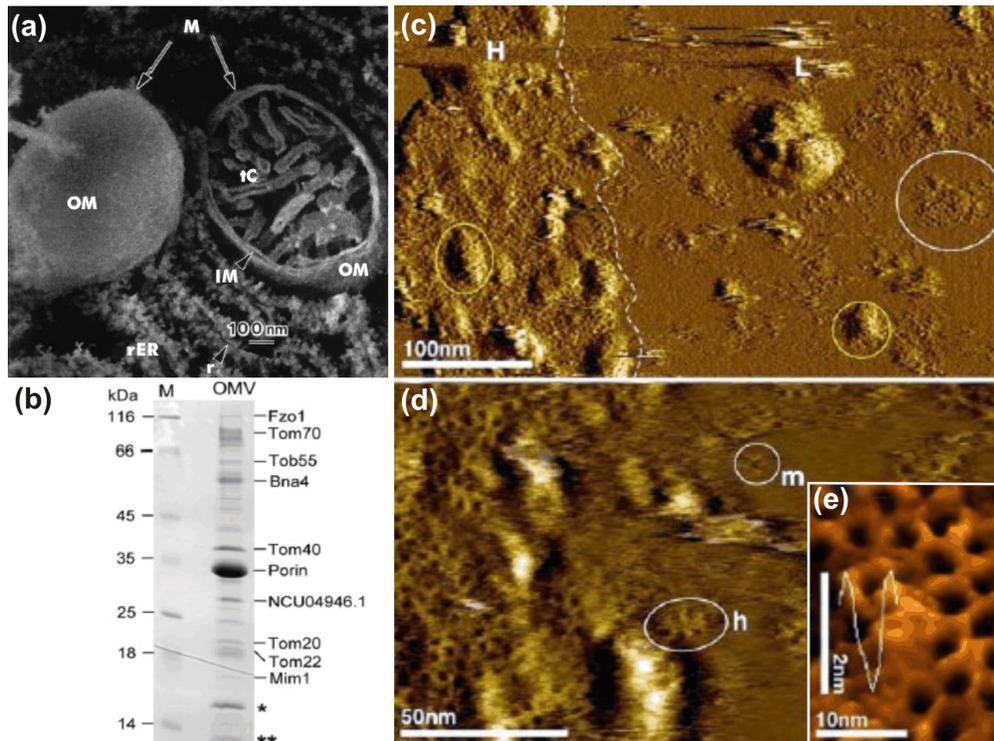


Figure 2-1: Organisation and surface topology of the outer mitochondrial membrane.

(a) Exposure of the surface (left) and interior structure (right) of mitochondria obtained by high-resolution scanning electron microscopy^[10]. Observed structures are marked as follows; (M) mitochondria, (OM) outer mitochondrial membrane, (IM) inner mitochondrial membrane, (C) cristae, (tC) tubular cristae, (rER) rough endoplasmic reticulum, (r) ribosome. (b) The protein pattern of outer membrane vesicles (OMV) analysed by SDS-PAGE identifies VDAC (Porin) as the most abundant protein in the outer membranes of *N. crassa*^[16]. Indicated proteins are involved in protein import (Tom70, Tob55, Tom40, Tom20, Tom22, Mim1), fission and fusion (Fzo1), nicotinic acid biosynthesis (Bna4) or metabolic exchange (Porin/VDAC). (*) labelled proteins are unknown or of unknown function (NCU04946.1). (c-e) Surface topographies of the *S. cerevisiae* OM revealed by atomic force microscopy^[18]. (c) Medium resolution topograph. Rugged areas refer to higher (H) and lower (L) ScVDAC containing domains of about 80% and 20% protein density, respectively. Larger protrusions (yellow encircled) indicate peripheric proteins, presumably attached to ScVDAC. (d) and (e) High-resolution AFM topographs. ScVDAC pores are either monomeric (m) or assembled to densely packed arrays (h). The estimated pore sizes averages to bores of 3.8×2.7 nm in which the tip could enter up to 2 nm.

2.3.1 General function of VDAC

While the inner mitochondrial membrane contains several distinct carriers, transporters and channels^{[11][12][13]}, only VDAC is known to facilitate the metabolic exchange across the outer mitochondrial membrane. Except for the nuclear encoded mitochondrial proteins which were translocated by the TOM machinery and a few membrane permissible compounds like molecular oxygen all metabolites have to pass the outer mitochondrial membrane through this channel^[23].

However, it was also shown that the TOM holo complex from *N. crassa* forms large open pores permeable to molecules up to 6 kDa^[24]. Hence, it must be assumed, that the TOM and most probably also the SAM complex contribute to the metabolic exchange across the outer mitochondrial membrane, albeit to a much lower extent due to their expression level.

2.3.2 The different isoforms of the VDAC

VDAC proteins are ubiquitously expressed in all mitochondria containing organisms. However, depending on the organism and its complexity several isoforms were detected. For instance, *Neurospora crassa* possesses only one isoform, *Saccharomyces cerevisiae* two and animals and plants normally up to three^[25].

Among these, the archetypal one is often referred to as VDAC1^[22]. Based on alignments of their primary structure, mammalian VDACS of the same isoform are highly conserved as indicated by a sequence identity of at least 98%. The autologous isoforms still have a sequence identity of about 70%. Additionally, VDAC2 can contain splice variant dependent N- and C-terminal extensions which are not present in the other isoforms. In contrast, VDAC sequences of mammals, fungi and plants exhibit similarities of approximately 40% at most. Nevertheless, despite the low similarity on the primary structure level the vast majority of the isolated VDAC homologs share the same fundamental properties regarding conductance, anion selectivity and voltage dependence^[26]. Moreover, the complementation of a VDAC-deficient yeast strain with the mouse genes *vdac1* and *vdac2* demonstrate the functional compatibility among certain orthologs^[27].

2.3.3 Conductance, voltage dependency and ion selectivity of the VDAC

Depending on the transmembrane potential the vast majority of the channel homologs exhibit two separated conductance states when reconstituted into planar lipid bilayers, a phenomenon known as voltage gating. At zero or low membrane potentials the channel resides in a high conductance state. This so called open state is characterised by a conductivity of about 4 nS in 1 M KCl consistent with an estimated pore diameter of about 3 nm. Applying potentials of more than 30 mV lead to a 50-60% reduced channel conductance which is referred to as closed state and consistent with a pore diameter of approximately 1.8 nm. The observed conductivity transition is reversible and responds symmetrically to both positive and negative potentials as indicated by a bell shaped steady state conductance curve (Fig. 2-3).

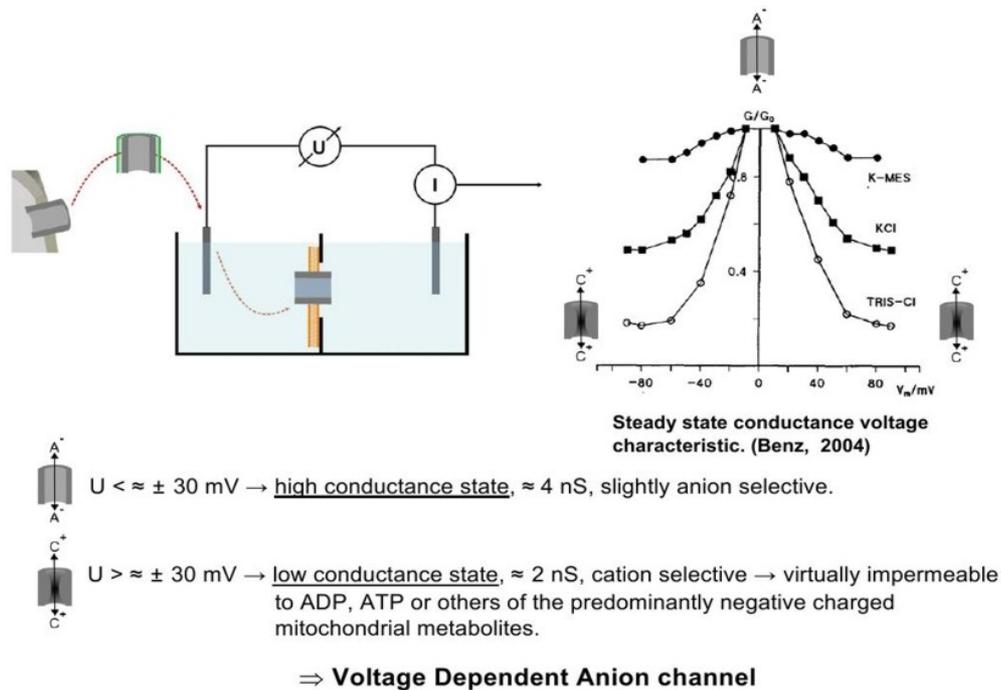


Figure 2-3: Conductance, voltage dependency and ion selectivity of VDAC.

Depending on the transmembrane potential the channel exhibits two different conductance states when reconstituted into planar lipid bilayers. The aqueous phase contains either 0.5 M KCl, 0.5 M K-MES or 0.5 M Tris-HCl. Although K^+ and Cl^- exhibit a similar aqueous mobility the single channel conductance for Tris-HCl in comparison to K-MES is significantly lower. Therefore the closed state is considered cation selective^[28].

The fact that VDAC adopts switchable states with a different permeability to mitochondrial metabolites suggests that the protein may not only facilitate, but also control the metabolic exchanges across the outer membrane. This assumption is consistent with the capability of the outer mitochondrial membrane to limit the flow of adenine nucleotides as observed in rat heart mitochondria^[29]. Nevertheless, concerning the voltage dependency of the channel, this assumption requires an outer membrane potential for its physiological relevance. Evidence for such a potential is given by an observed pH difference between the inter membrane space and the cytoplasm, although the outer membrane is highly permeable to protons^{[30][31]}. The observed difference of approximately 0.3 pH units were established by the ionic strength dependent fluorescence of FITC-BSA in isolated rat liver mitochondria. 0.3 pH units correspond to a potential of about 15 mV which is close to the range of VDAC's voltage sensitivity. A cause of this potential might be the Donnan equilibrium in addition to a metabolically derived potential emerging from mitochondrial activity^[32].

Moreover, it was shown that the sensitivity of different VDAC homologs considerably shifts to lower voltages in presence of several compounds. Among these compounds are NADH and certain polyanions which were observed to modulate the voltage sensitivity of HVDAC1^{[33][34]} and concerning the polyanions also of NcVDAC1^[35]. Interestingly, these compounds were further shown to modulate the ADP flux of the outer mitochondrial membrane *in organello*^[33]. NADH for instance, reduced the outer membrane permeability of isolated tomato mitochondria by a factor of 5 with respect to ADP^[36]. A similar result was observed in response to a polyanion in rat liver mitochondria. Furthermore, the voltage sensitivity of RVDAC1 and NcVDAC1 was found to be down shifted upon application of a colloidal osmotic pressure^[37]. This observations suggest that in addition to the membrane potential also hydration/dehydration forces may contribute to the conductance state of the channels.

To summarize, there is evidence that the channel exists in two interchangeable conformations which are responsible for the controlled and limited exchange across the outer mitochondrial membrane. However, due to the missing evidence for the factual existence of an outer membrane potential it is still not clear how the observed transition between the two states is actually driven *in vivo*.

2.3.4 The general structure of the VDAC

VDAC proteins are supposed to form large pores. A general insight into the global channel architecture was gained by electron microscopic studies of two dimensional VDAC1 crystals.

Crystals of NcVDAC were obtained by phospholipase A2 treatment of outer mitochondrial membranes from *N. crassa*^[38]. Images of these crystals exhibit large pores surrounded by a thin (~1 nm) protein wall. The inside of the wall forms an aqueous channel whose diameter of about 2.8 nm is in agreement with the pore diameter derived from the open state conductance. A reconstructed three dimensional NcVDAC surface further indicates that the observed channel wall resembles primarily a right-circular barrel with an average diameter of 3.7 nm. The attained height of this barrel is in the range of the assumed membrane bilayer thickness of about 4 to 4.5 nm. Moreover, there are also some anomalous features deviating from the cylindrical form of the channel wall. Among these irregular features are indentations of the barrel edges on either side, resulting in an uneven height of the cylinder (Fig. 2-4, sites B,D). In addition, a vertical and a diagonal groove of the lateral barrel surface are also found (Fig. 2-4, sites A,C).

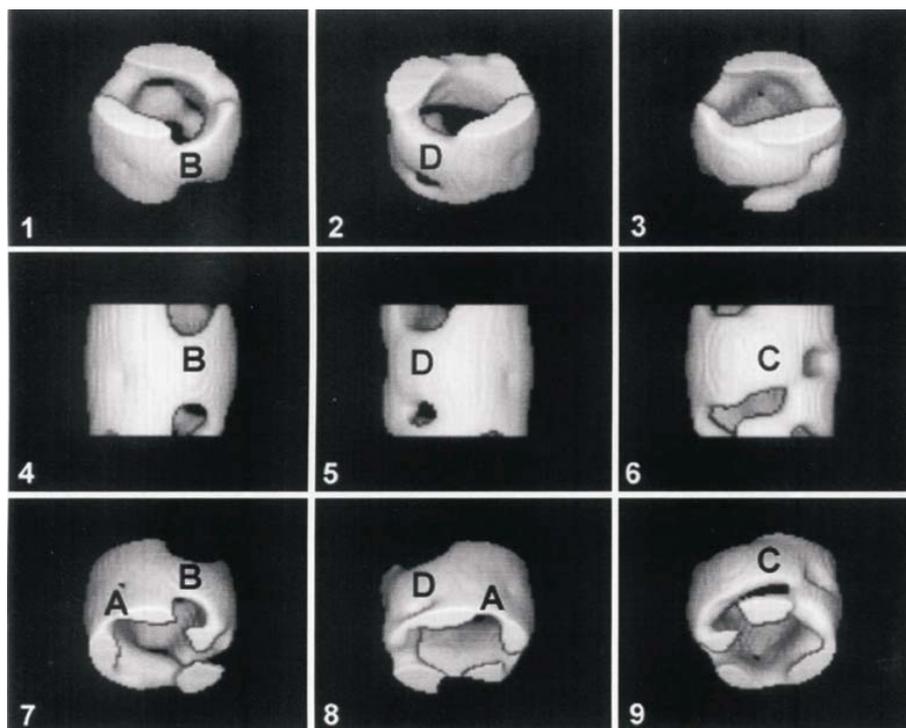


Figure 2-4: Three dimensional NcVDAC1 surface as reconstructed from tilted crystal projections ^[39].

3D images of NcVDAC1 in three different rotations about the z axis. The channel is represented in the following orientations. Untilted (middle row), forward tilted by 40° (upper row) backward tilted by 40° (lower row). Labels B and D refer to sites of an uneven height of the barrel wall. Labels A and C refer to a vertical (A) and a diagonal (C) groove in the barrel wall, respectively.

By negative stain electron microscopy of single particles and two dimensional crystals of human VDAC1 quite similar dimensions were observed^[40]. Unlike NcVDAC1, these experiments were conducted on pure HVDAC1 fractions produced by heterogeneous expression and refolding. Micrographs which were obtained from detergent dissolved HVDAC1 revealed small particles with diameters of approximately 0.35 to 0.4 nm and among them several with a stain-filled pore. Interestingly, subsequent crystallisation led to an array showing always two opposite oriented HVDAC1 molecules per asymmetric unit. Both channels exhibited diameters of 0.37 nm but revealed either an oval or triangular shape of their pore entrances. Regarding the oval bore an inner diameter of 17–20 Å has been determined. A striking difference to NcVDAC crystals concerns the observed surface structure of HVDAC1. The relief reconstruction of the HVDAC1 crystals revealed protein domains protruding from the bilayer surface. The surface topographs of NcVDAC, by contrast, showed a protein deeply embedded into the membrane bilayer ^[41]. Thus, a distinct difference in surface topology across the diverse VDAC1 species must be assumed.

The approximate molecular weights of VDAC proteins range from 28 to 36 kDa^[42]. With respect to NcVDAC1, the channel is composed of a single polypeptide chain as calculated from the surface density of the 2D crystals scanned by transmission electron microscopy^[41]. A monomeric topology is also confirmed for ScVDAC1 as revealed by the non-appearance of hybrid channels after parallel expression of mutant and wild type ScVDAC1 in yeast^[43].

Recently, a phylogenetic study with a large set of VDAC sequences of different origin (including plants, animals, fungi) was conducted^[42]. In the scope of this study also secondary structural predictions were made and aligned. Remarkably, all of the sequences revealed a secondary structural pattern composed of 19 β -strands and a preceding N-terminal α -helix (Fig. 2-5). Due to the distribution of several β -strands across the whole sequence a topology similar to various outer membrane proteins of Gram-negative bacteria can be assumed.

Across the different kingdoms VDAC homologs share only rather low sequence similarities of about up to 40% at its best. The most striking features concern the N-terminal α -helix, a highly conserved GLK-motif at the 6th β -strand, and a region which encompasses the eukaryotic porin signature pattern (PROSITE entry: PS00558)^[42] at β -strand 16 (Fig. 2-5). This signature pattern is highly significant for VDAC proteins and allows with minor exceptions the reliable detection of this channel in a large number of different eukaryotic genomes.

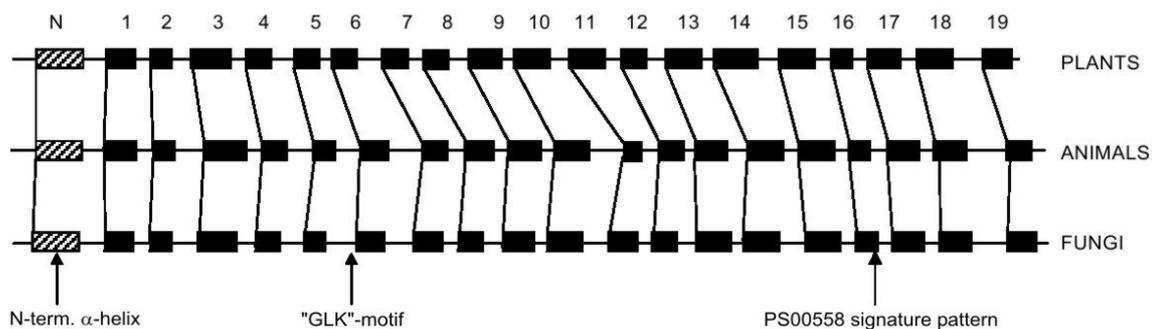


Figure 2-5: Similar secondary structural pattern of homolog VDAC proteins from different organisms^[42].

Despite of a low sequence similarity VDAC homologs of animals, plants and fungi exhibit an uniform secondary structural pattern composed of an N-terminal α -helix (hatched bar) and 19 β -strands (black boxes). The positions of the most conserved segments are indicated by their position along the sequence (black arrows).

2.3.5 Fold and architecture of bacterial β -barrel membrane proteins

A characteristic for bacterial proteins of the outer membrane is a central β -sheet cylinder composed of an even number of tilted antiparallel β -strands which originate either from one or several polypeptides. Adjacent strands are linked consecutively by short connections on the periplasmatic side and longer flexible loops at the extracellular side of the membrane (Fig. 2-6 A). Furthermore, most β -strands exhibit an intrinsic sequence pattern of alternating nonpolar and predominantly polar residues, resulting in an exclusively hydrophobic surface on one side of the strand (Fig. 2-6 A). This pattern is framed by aromatic amino acids, the so called aromatic girdle, a hallmark feature of all known membrane proteins (Fig. 2-6B). The diameter of the barrel varies by the number of strands and their inclination versus the barrel axis. Among the so far structurally described β -barrel membrane proteins the strand numbers and tilt angles vary from 8 to 22 strands and 35 to 50 degrees.

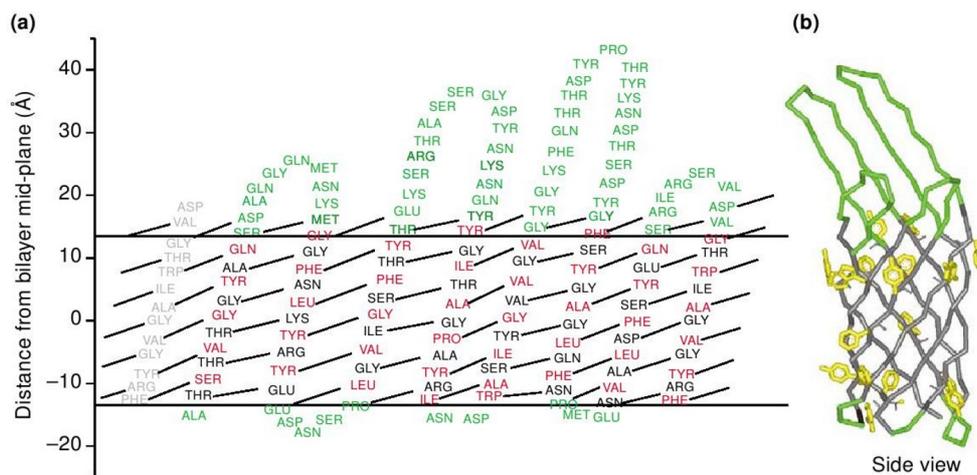


Figure 2-6: Fold and architecture of bacterial β -barrel membrane proteins^[44].

(a) Two dimensional topology representation of the bacterial β -barrel protein OmpX. The membrane embedded part of the protein is shown in between the two horizontal lines. This part is covered by eight tilted antiparallel β -strands which are stabilised by a hydrogen bonding network. The individual strands are linked by short connections on the periplasmatic and longer flexible loops at the extracellular side (shown in green). Residues of membrane embedded strands exhibit a intrinsic sequence pattern of alternating outward facing unipolar (red) and inward facing predominantly polar residues (black). (b) Lateral view of the three dimensional structure of OmpX on the same y-scale. The twofold aromatic girdled surface is indicated by the incident aromatic residues (shown in yellow).

Another aspect of this fold is the allowed degree of sequence variability within the mentioned strand pattern and particularly in the loop regions. The latter are mostly involved in the functional characteristics of this membrane protein group^[45]. For instance, by folding into the barrel lumen these loops are jointly responsible for the permeability and selectivity of several bacterial porins.

With exception of the phospholipase OmpLA and the exclusively trimeric porins all other currently known representatives of the bacterial β -barrel proteins exist as monotopic β -barrels in the membrane. OmpLA also represents an exception in the sense that it is found in an inactive monomeric and an active dimeric form^[46].

So far, the occurrence of β -barrel proteins is restricted to the outer membrane of Gram-negative bacteria^[47]. This membrane rarely contains polytopic membrane proteins of the α -helical type. The only structurally described polytopic outer membrane protein of the α -helical type is Wza, an integral α -helical barrel protein which is responsible for group 1 capsule export in *E. coli*^[48]. By contrast, there are no indications that β -barrel proteins exist also in other membrane systems such as the cytoplasmic membrane. Therefore, the evolution of the β -barrel membrane proteins seems to be closely related to the constitution and function of the outer membrane of these bacteria.

Due to the endosymbiotic theory, however, it is assumed that this membrane protein type exists also in the outer membranes of chloroplasts and mitochondria^[49]. Even if many of the mitochondrial outer membrane proteins like Tom40 and VDAC only exhibit a low sequence similarity to bacterial β -type membrane proteins^[8], they are predicted to adopt an equal topology.

2.3.6 Evidence for a β -barrel fold of VDAC

Concerning Tom40 and VDAC, the suggested β -barrel fold is in addition to the sequence analyses also confirmed by circular dichroism (CD) and attenuated total reflection fourier transform infrared (ATR-FTIR) spectroscopy^{[50][51][52]}.

The CD spectra of NcVDAC are for instance hardly distinguishable from the spectra of the bacterial porin OmpF^[52]. According to this, they also agree in their estimated β -sheet contents of about 60%^[52]. Values in the same range were again calculated from CD spectra of recombinant in inclusion bodies produced and refolded HVDAC1^[53]. However, other CD studies of native as well as recombinant ScVDAC1 and NcVDAC1 revealed lower, but still significant, values in the range of 30 to 45% β -sheet content^[54].

Further evidence for the proposed β -barrel fold is derived from recorded ATR-FTIR spectra of two VDAC isoforms from *Phaseolus vulgaris* (PvVDAC31, PvVDAC32) which to a large extent also coincide with the corresponding spectra of OmpF^[50]. Furthermore, the ATR-FTIR analysis strongly indicates that the β -strands of the two isoforms run antiparallel and are inclined by an angle of approximately 45 degrees^[50]. However, slight spectral distinctions also indicate certain structural differences between the PvVDAC isoforms and OmpF. One of them is related to the length of the individual strands which seems to be shorter than the averaged 12 amino acids in the bacterial protein as determined from a shift of the amide I band^[50]. Another difference concerns the increased α -helical contents of the PvVDAC isoforms, a fact that is attributed to their predicted N-terminal α -helices^[50]. Moreover, ATR-FTIR measurements were also applied on recombinant produced isoforms of HVDAC1 and HVDAC2. Both spectra also were strongly indicative for a topology composed of anti-parallel β -strands and estimated β -sheet contents of 48% for HVDAC1 and 41% for HVDAC2^[55].

2.3.7 Model of the proposed VDAC structure and its gating mechanism

In consideration of the pore diameter, the secondary structural content and the common β -barrel geometries, a number of potential VDAC models have been proposed. All of them coincide in a β -barrel and an N-terminal α -helix, but differ substantially in their topology (Fig. 2-5).

One model favours a channel wall composed of a transmembrane α -helix in addition to 13 β -strands^{[56][26][57]}. In combination with an analysis of the primary sequences of NcVDAC1 and ScVDAC1^[58], this model is based on a variety of selectivity altering point mutations in ScVDAC1^[56]. Initially developed with 12 β -strands, the model was later extended by a further β -strand, due to the results obtained by biotin modification of ScVDAC1 cysteine mutants^[59]. Even if a β -barrel closed by an α -helix represents a unique membrane protein fold, this was hypothesized on the basis of several biochemical observations. For instance, charge altering point mutations concerning the N-terminal α -helix and the first following β -strands affected only the ion selectivity of the open state^[56]. Hence, it was concluded that channel closure is accomplished through removal of the corresponding transmembrane parts and subsequent relocking of the remained β -strands. Such a mechanism was further confirmed by streptavidin induced trapping of the closed state after insertion and biotinylation of several cysteines into the assumed mobile transmembrane part^[57]. According to this mechanism it was assumed that just this unusual fold “might provide the right amount of structural energy facilitating the large conformation associated with channel gating”^[60].

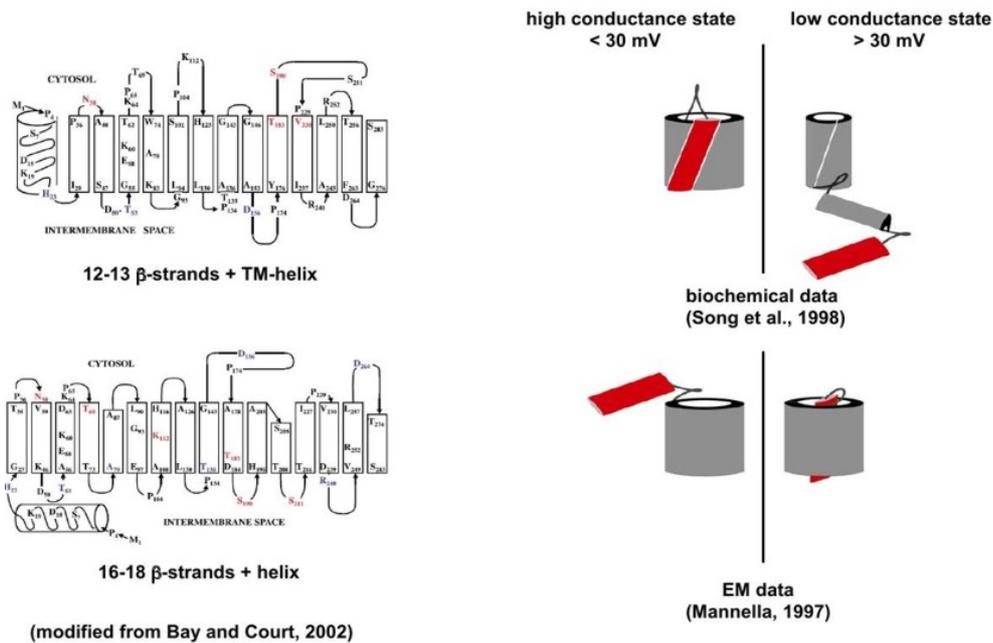


Figure 2-7: Model of the proposed VDAC structures^[61] and its gating mechanisms.

Two topology models of VDAC are proposed so far. One model suggests a topology of 13 β -strands in combination with a transmembrane α -helix, an alternative model is based on 18 β -strands and an α -helix located outside the barrel. Gating mechanisms are proposed for both topologies. In case of the first model channel closure is accomplished through removal of a certain transmembrane part including the α -helix and subsequent relocking of the remaining β -strands to form a smaller barrel^[57]. In case of the second model gating is mechanically accomplished by reorientation of the α -helix, most likely from the barrel exterior into the lumen^[62]. Presented cartoons were drawn in accordance to the proposed mechanisms.

Alternative models by contrast, propose a common 16 stranded β -barrel as the pore forming channel wall^{[63][55][64]}. Beyond the β -barrel these models also predict an N-terminal α -helix which is assumed to reside either in- or outside the barrel lumen^{[64][63][65]}. Interestingly, even if these models are consistent regarding the number of predicted β -strands, they partially vary to a great extent in the sequence regions where the β -strands are assigned to. Most of the models rely on alignments and computerised modelling in which a multitude of biochemical and biophysical data were integrated^{[63][64]}. Regarding the origin such models were established for NcVDAC, ScVDAC1 the VDAC of *Dictostelium discoideum* as well as for the isoforms 1 of human and mouse. Additionally, a 16-stranded topology was also established by the limited proteolysis of in detergent embedded HVDAC1 and a following MALDI mass spectrometric analysis^[55]. Further support for a 16 to 18-stranded barrel derived from a model which was drawn on the comparison between already existing β -barrel membrane protein structures and the EM data obtained from the outer membranes of *N. crassa*^{[38][66]}.

For this type of model a potential gating mechanism was developed on the basis of a multitude of EM observations. According to this mechanism channel gating is presumably accomplished by the movement of a mobile domain between the ex- and interior of the barrel. EM images of NcVDAC 2D crystals pre-treated with a VDAC modulating polyanion which is known to force the closed state of the channel, support this mechanism^[67]. After pre-treatment, the images exhibited a reduced lumen bore without a change in outer channel wall diameter in association with the disappearance of preexisting lateral surface protein^[62]. Since in untreated 2D crystals the N-terminal α -helix was found to laterally extend from the barrel^[39] this α -helix might be a potential candidate for the mobile domain which reduces the channel conductance upon movement^[66]. However, if the mobile domain coincide with the N-terminal α -helix or rather with a flexible loop is still a matter of debate. However, this mechanism neglect the biochemical observation that charge altering point mutations of the N-terminal α -helix affect only the ion selectivity of the open state. Another argument in the same line concerns the fact that the channels open state conformation is shown to be destabilized by the truncation of the N-terminal α -helix^{[54][68]}. Thus, both observations argue the N-terminal α -helix as lumen integral part of the open state.

The distinct influence of the N-terminal α -helix on the open state and a reconsideration of the EM data led finally to a third proposed mechanism^{[38][66]}. According to this proposition the N-terminal α -helix is lumen integral attached to a certain groove of the inner channel wall in the open state. In this position the α -helix function in both, open state stabilization and selectivity control. Removed from this groove, e.g. by an applied potential or the influence of another protein, the channel becomes destabilized and adopts its low conducting conformation. Channel closure would hence be the consequence of a destabilized channel wall. Once destabilised, a structural rearrangement of the relevant wall region or the inward-folding of at least one of the loops is suggested to narrow the barrel diameter^{[38][66]}.

2.3.8 The role of VDAC in mitochondrial complexes

Besides the controlled and limited exchange there is evidence that VDAC acts at the interface between mitochondria and the cytoplasm also within other cellular functions. As such the channel is involved in energy metabolism and the mitochondrial phase of apoptosis^[69].

2.3.8.1 Involvement of VDAC in complexes of the energy metabolism

In rat liver, brain and heart mitochondria it was observed that VDAC acts as the mitochondrial binding site for the cytoplasmic hexo- and glycerol kinases^{[70][71][72]} and connects them at the mitochondrial contact sites with the adenine nucleotide translocator (ANT) of the inner membrane^[73]. As a consequence, VDAC provides the cytosolic kinases with the preferential access to ATP through functional coupling of sites responsible for oxidative phosphorylation and metabolic activation^[70]. Interestingly, it seems that VDAC alters its conformation upon direct complex formation with the ANT in a way which increases its affinity to the cytoplasmic kinases^[74].

Additionally, there is evidence of a further highly organized “energy transport channel”, concerning the phosphocreatine cycle and mediated through the indirect interaction between VDAC and ANT via the mitochondrial creatine kinase in the intermembrane space^{[73][75]}. The complex, thereby formed, was shown to promote the formation of creatine kinase octamers^[76] and simultaneously abates the affinity of VDAC to the cytoplasmic kinases^[74].

However, it is still not demonstrated whether the formation of the two complexes is controlled by a VDAC influencing potential or a certain conformation of the ANT. But, regardless of the triggering event, it is widely believed that the functional states of VDAC and the mitochondria are connected^[74].

2.3.8.2 Involvement of VDAC in the mitochondrial phase of apoptosis

Besides the functional coupling of metabolic processes there is further evidence that VDAC is also involved in processes concerning the mitochondrial pathway of apoptosis in multicellular organisms^[60]. The MIMS contains a couple of pro-apoptotic proteins which are retained by the outer mitochondrial membrane^[77]. Among these proteins are for instance pro-caspases, Smac/Diablo as well as cytochrome c.

Once released from the inter membrane space these proteins participate in specific points of the apoptotic cascade *e.g.* in the cytochrome c initiated formation of the apoptosome^[78]. It is currently not clear how the release of these factors, which is known as mitochondrial outer membrane permeabilization (MOMP), exactly proceeds. In principle there are two conceivable scenarios: (1) the formation of an adequate channel or (2) the rupture of the outer membrane^[79]. Concerning the two possibilities it is only proven that the Bcl-2 protein family has a significant impact on the development of MOMP.

However, several models include also VDAC as a component of the MOMP machinery. Evidence for the involvement of VDAC in MOMP derived from the fact that several proteins of the Bcl-2 family were found to act on VDAC. For instance, sucrose uptake by liposome-reconstituted Rat VDAC1 (RVDAC1) and recombinant human VDAC1 (HVDAC1) was found to be abolished in the presence of anti-apoptotic Bcl-X_L and, by contrast, enhanced in presence of the pro-apoptotic proteins Bax or Bak^[80]. Basically the same effects were observed concerning the release of cyt c in an analogical experimental set up^[80]. In the scope of this study it was also observed that mitochondria which were isolated from a ScVDAC1 deficient yeast strain exhibit in the presence of Bax or Bak neither a loss of the mitochondrial membrane potential ($\Delta\Psi_m$), nor the release of cyt c. However, both was detectable in a Bax and Bak dependent manner if wild type or HVDAC1 complemented yeast mitochondria were used. Remarkably, none of the effects were again ascertained when Bcl-X_L was coexisting^[80]. Additional support for direct interactions between VDAC and certain members of the Bcl-2 family derived from conductance measurements of rat liver and NcVDAC1^{[81][82]}. The addition of pro-apoptotic Bid for instance, induced a closure of RVDAC1 and NcVDAC1 as revealed by the significant lower conductance of the into planar lipid bilayers reconstituted channels^[81]. In contrast, Bcl-X_L, was found to maintain RVDAC1 in an "open" high conductance state^[82]. However, compared to the findings mentioned above, the addition of Bax failed to bring about changes regarding the conductance of RVDAC1^[81]. Since the exact molecular interactions of Bcl-2 proteins and VDAC are not known yet, the observations support both scenarios: (1) the constitution of a potential large channel somehow influenced by VDAC and certain Bcl-2 family members and (2) the rupture of the outer membrane; here the interaction between VDAC and a Bcl-2 member induces VDAC closure and subsequent hyperpolarization leading eventually to matrix swelling and hence rupture^[79].

Moreover, the action of apoptotic proteins on VDAC has also to be considered in relation to the already mentioned set of VDAC interactions. There is compelling evidence that not only VDAC, but also dynamic complexes around the central VDAC-ANT interaction may be controlled by the Bcl-2 protein family and several other factors^{[4][83]}. The so called permeability transition pore complex (PTPC) resembles a voltage dependent high conductance channel which is able to increase the permeability of the inner mitochondrial membrane through its alteration. Channel opening was shown to be influenced by pro-apoptotic proteins as well as by calcium, reactive oxygen species and artificially by some chemotherapeutic agents^[84]. To what extent VDAC affects this complex is quite unclear at present, but it seems that the protein is besides the ANT and cyclophilin involved in both PTPC assembly and function^[79].

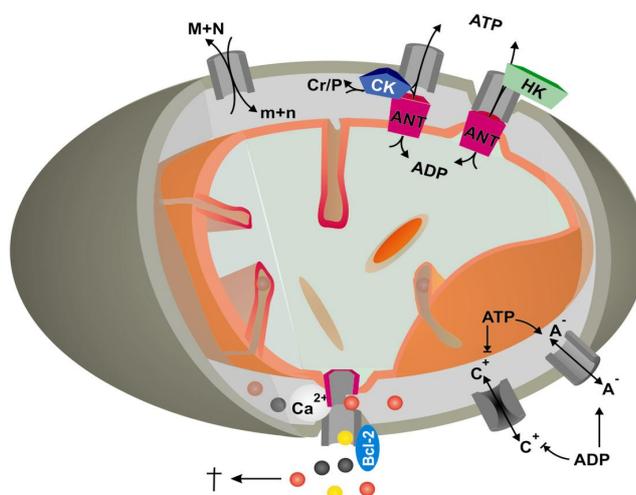


Figure 2-2: General functions of VDAC.

The voltage dependent anion channel resembles the major pass through of the outer mitochondrial membrane for the vast majority of mitochondrial metabolites. The channel is thought to control and limit the exchange of metabolites by different conductance states. A high conductance state which is preferentially anion selective and a low conductance state which is preferentially cation selective virtually impermeable for ADP, ATP and other negatively charged metabolites. VDAC is further participating in complexes involved in energy metabolism and the mitochondrial phase of apoptosis. CK: Creatine kinase; HK: Hexokinase; ANT: Adenine nucleotide translocator; Bcl-2: Pro and anti-apoptotic proteins of the Bcl-2 family; Coloured spheres: Pro-apoptotic proteins.

However, there is strong evidence that also alternative, VDAC independent MOMP mechanisms exist (for a review, see [79]). Bax oligomers, for instance, were recently shown to produce supra-molecular openings (permeable to 2 MDa dextrans) in mitochondrial outer membrane vesicles, in vesicles reconstituted from extracted mitochondrial lipids and in liposomes which resemble the lipid composition of *Xenopus* mitochondria [85]. The same was observed with monomeric Bax in the presence of Bid. Interestingly, Bcl-X_L was shown again to be effective against the release induced by oligomeric Bax or the combination of monomeric Bax and Bid. Thus, concerning MOMP, Bax-mediated permeabilization have to be equally considered. Nevertheless, different MOMP mechanisms are not mutually elusive and may play a role in alternative apoptotic scenarios [79].

2.4 Conceptual formulation

VDAC proteins of several hosts have been extensively studied within the last three decades. As a result VDAC is depicted as the main mitochondrial outer membrane pore that functions at this position in a variety of metabolic and apoptotic complexes. Although several models have been developed over the years, the exact topology of this protein is still unknown.

The aim of this study was to elucidate the structure of the human VDAC I (HVDAC I) at atomic resolution by X-ray crystallographic and multidimensional NMR methods. The knowledge of the exact topology should further provide an improved insight into the transport and gating function of HVDAC1. Moreover, multidimensional NMR techniques were used to identify dynamic domains as well as potential binding sites which are involved in the interaction between HVDAC1 and known binding partners such as the pro-apoptotic protein Bid.

Since the projected investigations require substantial quantities of partly labelled and deuterated protein it was planned to overproduce a histidine tagged version of HVDAC1 in *Escherichia coli*. This approach based on the high protein recovery due to inclusion body formation as exemplified in previous studies as well as on the refolding protocols therein established^{[53][55]}. Hence, a further optimization of the expression, purification and refolding methods appeared promising in order to obtain sufficient protein amounts for the intended structure determination.

3 Materials and methods

Unless otherwise noted all chemicals and reagents were purchased in the highest available purity grade from Sigma-Aldrich (St. Louis, USA) Merck (Darmstadt), Serva (Heidelberg) and Roth (Karlsruhe). Detergents were purchased from Anatrace (Maumee, USA). Labelled compounds were obtained from Eurisotop (Saint-Aubin Cedex, France). Deuterium oxide (D₂O) was supplied by OntarioPower (Pickering, Canada). All solutions, buffers and media were sterile-filtered after preparation. Applied lab ware for bacterial cultivation and molecular biological techniques was heat sterilized prior to utilization. If not otherwise indicated all experiments involving standard techniques were performed in accordance to the manufacturers protocols and recommendations.

3.1 Materials

3.1.1 General Instruments:

PCR cycler	Biometra – Thermocycler 3 – ,Göttingen
DNA sequencer	Applied Biosystems – ABI Prism 377 –, Foster City, CA, USA
Transfection apparatus	BioRad – Gene Pulser –, Richmond, CA, USA
Shaking incubator	Infors-HT AG – Multitron AJ20 –, Bottmingen, Switzerland
Fermenter	B.Braun Melsungen AG – Biostst V – Melsungen
Centrifuges / Rotors	BeckmannCoulter – Avanti J25 / JLA-25.500, JA-10.500; Avanti J20-XP / JLA-8.100; Optima LE 80 K ultra centrifuge L7-55 / 45Ti; 50Ti; 60Ti –, Fullerton, USA Eppendorf AG – 5417R / FA45-30-11 –, Hamburg
French Press	Polytec GmbH – Aminco 20K French Pressure Cell –, Waldbronn
FPLC System and Columns	Amersham Pharmacia Biotech – ÄKTA systems Explorer and Basic –, Freiburg
UV-VIS spectrometer	Pharmacia LKB Biochem Ltd. – Ultraspec II – Cambridge, United Kingdom
CD spectrometer	JASCO – J-715 Spectropolarimeter –, Easton, MD, USA
FT-IR spectrometer	Thermo Fisher Scientific – Nicolet 6700 – Waltham, USA
Agarose horizontal gel electrophoresis apparatus	Biometra – Agagel mini – ,Göttingen

3.1.2 Consumables

Electroporation cuvettes	(Gene Pulser [®] , 0.2 cm gap) Biorad, Richmond, USA
PS-tube 14 ml	Greiner bio-one. Kremsmünster, Austria
Petri dishes (94/16)	Greiner bio-one. Kremsmünster, Austria
ABI Prism BigDye Terminator Cycle Sequencing Ready Reaction Kit	Perking Elmar, Wellesley, USA

AutoSeq™ G-50 disposable spin column	Amersham Pharmacia Biotech, Freiburg
NuPAGE® Gel System, NuPAGE® Novex Bis-Tris Gels and buffers	Invitrogen, Karlsruhe
Centrifugal filter devices	Millipore Amicon, Billerica, USA
Cellulose membrane dialysis tubing (cut-off 10kDa)	Sigma-Aldrich, St. Louis, USA
Crystallization screens (Crystal screen™, Crystal screen 2™, Crystal screen light™, Membfac™, PEG/Ion™, Index™, SaltRx™)	Hampton Research, Aliso Viejo, USA
Crystallization optimization screens (Additive screen™, Detergent screens™ I-III, heavy atom screen Pt™)	Hampton Research, Aliso Viejo, USA
Siliconized Glass Circle Cover Slides (22 mm)	Hampton Research, Aliso Viejo, USA
VDXM™ plates with sealant	Hampton Research, Aliso Viejo, USA
Crystallisation consumables	Hampton Research, Laguna Niquel, USA

3.1.3 Kit systems

Qiaquick Plasmid purification kit	Quiagen, Hilden
Quickchange site-directed mutagenesis kit	Stratagene, La Jolla, CA, USA

3.1.4 Fine Chemicals

Acryl amide	Biorad, Hercules, USA
Tryptone (Bacto™ -Tryptone)	Becton, Dickinson and Co., Sparks, USA
Yeast extract (Bacto™ Yeast extract)	Becton, Dickinson and Co., Sparks, USA
Agar (Bacto™ Agar)	Becton, Dickinson and Co., Sparks, USA
Agarose	Seakem, Teknova, Half Moon Bay, CA, USA
Deoxyribonucleotides (dNTPs)	Amersham Pharmacia Biotech, Freiburg
IPTG	Gerbu Biotechnik GmbH, Gaiberg
L-Selenomethionine	Anatrace, La Jolla, USA
Complete Protease inhibitor EDTA free	Hoffmann-La Roche Ltd. , Basel, Switzerland
Protein LMW marker	Amersham Pharmacia Biotech, Freiburg
PageRuler unstained Protein ladder	Fermentas St. Leon-Rot
DNA Ladder	New England Biolabs, 1 kb ladder Ipswich, USA
Supercoiled DNA Ladder	Sigma-Aldrich, St. Louis, USA
Ni-Sepharose HP	Amersham Pharmacia Biotech, Freiburg
Ethidium bromide	Boehringer, Mannheim
n-octylpolyoxyethyleneglycol (OPOE)	Bachem, Weil am Rhein

n-octyltetraoxyethylene (C ₈ E ₄)	Bachem, Weil am Rhein
n-dodecyl-N,N-dimethylamine-N-oxide solution 30% (LDAO)	Sigma-Aldrich, St. Louis, USA
D-Glucose ¹³ C ₆ , 99%; D7, 97-98%	Larodan Fine chemicals, Malmö, Sweden
Amonium Chloride ¹⁵ N, 99%	Larodan Fine chemicals, Malmö, Sweden
Deuterium oxide (D ₂ O)	OntarioPower, Pickering, Canada

3.2 Strains and vectors

3.2.1 Strains

Strain:	Phenotype:
<i>Escherichia coli</i> M15 [prep4] (Quiagen, Hilden)	<i>E. coli</i> K12 NaI ^S Str ^S Rif ^S Thi ⁻ Lac ⁻ Ara ⁺ Gal ⁺ Mtl ⁻ F ⁻ RecA ⁺ Uvr ⁺ Lon ⁺ / carries prep4 (<i>lacI</i> encoding repressor plasmid)
<i>Escherichia coli</i> DL39 (CGSC, Yale, USA)	<i>F araD139 Δ(argF-lac)Ui69 rpsL150 relA1 thiA zei-724: :Tn10 glpR gyrA Δ(glpT-glpA)593</i>
<i>Escherichia coli</i> DL39 [prep4]	<i>F araD139 Δ(argF-lac)Ui69 rpsL150 relA1 thiA zei-724: :Tn10 glpR gyrA Δ(glpT-glpA)593</i> / carries prep4 (<i>lacI</i> encoding repressor plasmid)
<i>Escherichia coli</i> DH5α (GibcoBRL, Gaithersburg, USA)	<i>F φ80dlacZΔM15 Δ(lacZYA-argF) U169 endA1 hsdR17(rK, rK⁺) supE44 λ⁻ recA1 thi-1 gyrA96 relA1</i>
<i>Escherichia coli</i> BL21CodonPlus (DE3)-RIPL (Stratagen, La Jolla, USA)	<i>E. coli B F ompT hsdS(r_B⁻ m_B⁻) dcm⁺ Tet^r gal λ (DE3) endA Hte [argU proL Cam^r] [argU ileY leuW Strep/Spec^r]</i>

3.2.2 Vectors

pDS56/RBSII-VDACHis6	as described elsewhere ^[55]
pet23d-HisBID	as described elsewhere ^[66]

3.3 Growth Media

3.3.1 Antibiotics

Antibiotics containing media were supplemented shortly before use with 25 µg/ml kanamycin (Kan), 100 µg/ml ampicillin (Amp), 30 µg/ml chloramphenicol (Cam) or their combinations, respectively. All antibiotics were dissolved in 70% ethanol in a thousandfold higher stock concentration, aliquotted and stored at -20°C. Antibiotics containing agar plates were exclusively supplemented after heat sterilisation and re-cooling to 50°C.

3.3.2 LB agar plates

After adding 15 g agar per litre LB broth the suspension was heat sterilised, re-cooled to 50°C, supplemented with antibiotics and poured in aliquots of averaged 20 ml into petri dishes. After congelation the plates were stored in the dark at 4°C until use.

3.3.3 LB broth

Tryptone	10	g
Yeast extract	5	g
NaCl	10	g
NaOH (10 M)	0.2	ml
H ₂ O, deionised	ad 1000	ml

3.3.4 TB broth

Tryptone	12	g
Yeast extract	24	g
Glycerol (86%, w/v)	5	ml
Phosphate buffer (10x)*	100	ml
H ₂ O, deionised	ad 1000	ml

*) Phosphatebuffer 10x

KH ₂ PO ₄	23.14	g
K ₂ HPO ₄	164.33	g
H ₂ O, deionised	ad 1000	ml

3.3.5 Minimal medium

M9 Minimal medium (standard/deuterated)

M9 Salt (10x)*	100	ml
Glucose (20%)	20	ml
MgSO ₄ (0.1 M)	10	ml
CaCl ₂ (0.01 M)	10	ml
NH ₄ Cl*	1	g
Thiamine (1%)	0.2	ml
H ₂ O, deionised resp. D ₂ O	ad 1000	ml

*) M9 Salt (10x)

Na ₂ HPO ₄ × 2H ₂ O	60	g
KH ₂ PO ₄	30	g
NaCl	5	g
H ₂ O, deionised resp. D ₂ O	ad 1000	ml

3.3.6 Algal extract supplemented media (AES media)

M9 Salt deuterated (10x) v.s.	100	ml
Glucose (10% w/v)	10	ml
MgSO ₄ (0.1 M)	20	ml
L-leucine [§]	0.25	g
Vitamin mix ^a	5	ml
Trace element solution ^p	1	ml
Deuterated algal lysate amino acid mixture (10% w/v)*	10 (30) [#]	ml
D ₂ O	ad 1000	ml
labelled amino acids ^{&}	as indicated ^c	

*) Deuterated algal lysate amino acid mixture was produced and characterised at the MPI of Biochemistry; Dept. of Membrane Biochemistry as described^[87].

#) Preparatory cultures and overproduction cultures contained 30 ml and 10 ml of the algal extract, respectively.

§) No unlabeled leucine was added when leucine labeling was intended.

&) Preparatory cultures contained no labelled amino acids.

a) Vitamin mix

Thiamine (B ₁)	100	mg
d-biotin (H)	20	mg
Choline bromide	20	mg
Folic acid (B ₉)	20	mg
Niacin amide (B ₃)	20	mg
d-panthotenic acid (B ₅)	20	mg
Pyridoxal (B ₆)	20	mg
Riboflavin (B ₂)	20	mg
Tris-base (saturated)	0.2	ml
D ₂ O	ad 100	ml

b) Trace element solution

HCl (5M)	16	ml
FeCl ₂ × 4H ₂ O	10	g
CaCl ₂ × 2H ₂ O	370	mg
H ₃ BO ₃	130	mg
CoCl ₂ × 6H ₂ O	36	mg
CuCl ₂ × 2H ₂ O	8	mg
ZnCl ₂	680	mg
Na ₂ MoO ₄ × 2H ₂ O	1.21	g
MnCl ₂ × 4H ₂ O	80	mg
D ₂ O	ad	1000 ml

c) labelled amino acids

Overproduction cultures (500 ml each) were supplemented with either one or in case of the ¹⁵N-Met, [¹⁵N, ¹³C]-Leu, [¹⁵N, ¹³C]-Ile sample with all three amino acids 15 min prior induction.

L-Methionine (15N, 95-99%)*	90	mg
L-Leucine (U-13C6, 98%; 15N)*	80	mg
L-Isoleucine (U-13C6, 98%; 15N, 98%)*	50	mg
L-Phenylalanine (15N, 98%)*	150	mg
L-Valine (U-13C5, 98%; 15N)*	70	mg
DL-Lysine 2HCl (15N2, 98%)#	250	mg
L-Tyrosine (15N, 98%)#	80	mg
L-Arginin HCl (15N4, 98%)#	100	mg
DL-Alanine (15N, 98%)\$	250	mg

Amino acids were purchased from *) Euriso-top, Saint-Aubin Cedex, France; #) Sigma-Aldrich, St. Louis, USA; \$) OMNI Life Science, Bremen.

3.4 General Molecular Biological Techniques

3.4.1 Preparation of electro-competent *E. coli* cells

Single colonies of the different *E. coli* strains were obtained by streaking an inoculum of the corresponding freezer stock across an LB plate and following incubation at 37°C overnight. Afterwards a preparatory culture was prepared by the inoculation of 35 ml LB broth with one of the individualised clones and overnight incubation in a 100 ml Erlenmeyer flask at 37°C and 200 rpm. 5 ml of this culture were then used to inoculate 500 ml of LB medium in a 2.5-litre baffled Erlenmeyer flask.

The main culture was cultivated at 37°C and 200 rpm until an OD₆₀₀ in-between 0.5 and 0.7 absorption units was reached. Afterwards, the culture was cooled down on ice for 30 min. Cells were then harvested at 4000 *g* for 20 min and washed three times by resuspension and centrifugation at 4000 *g* for 20 min with 500, 250 and at least 50 ml of a pre-cooled 10% glycerol solution. Finally, the cells were resuspended in 400 µl of pre-cooled 10% glycerol, subdivided into 70 µl aliquots, shock frozen in liquid N₂ and stored at -70°C until use.

3.4.2 Transformation of *E. coli* cells

For transformation of *E. coli* strains, about 1 µg of plasmid DNA was mixed with 70 µl of thawed electrocompetent cells, transferred into a pre-cooled cold electroporation cuvette and incubated on ice for 5 minutes. Plasmid transformation was performed by electroporation with a Biorad Gene Pulser System, set to 1.5 kV charging voltage, resistance 800 Ω and capacitance of 25 µF. Transformed cells were immediately diluted with 1 ml LB, transferred to a PS-Tube and incubated for 45 min at 37°C and 200 rpm. Afterwards 10 to 20 µl of the cell suspension were plated. In case of transformed Quikchange® reactions, cells were harvested after the incubation period at 4000 *g* for 20 min and resuspended in 250 µl LB broth. The whole suspension was plated on LB^{Amp} or LB^{Amp/Kan} media afterwards and incubated overnight at 37°C.

3.4.3 Determination of DNA concentrations

DNA concentrations were determined by UV absorption at 260 nm in quartz cuvettes with a path length of 0.3 cm. Concentrations for double stranded DNA (dsDNA) were calculated as follows:

$$\text{dsDNA } [\mu\text{g/ml}] = 44 \mu\text{g/ml} \times A_{260} \times 0.3^{-1}$$

3.4.4 Plasmid amplification

PDS56/RBSII-VDACIHis and pET23dHisBID were amplified in the *E. coli* strains M15[prep4] and DH5α. For amplification, 6 ml of LB^{Amp/Kan} (M15[prep4]) or LB^{Amp} (DH5α) medium were inoculated with a single colony of the corresponding strain and incubated at 37°C and 200 rpm overnight. Cells were harvested by centrifugation at 4000 *g* for 20 min and subsequently used for plasmid isolation.

3.4.5 Isolation of plasmid DNA from *E. coli* cells

All plasmids were purified using the Qiaprep® Miniprep protocol as recommended by Quiagen™. Plasmid DNA was finally eluted with 30 µl of deionised H₂O and stored at -20°C until use.

3.4.6 Analysis of plasmid DNA by agarose gel electrophoresis

Purified plasmids were analysed by horizontal agarose gelelectrophoresis. All agarose gels were run in Tris-Acetate (TAE) buffer (50 mM Tris-acetate, 1 mM EDTA, pH 8.0). Gels were prepared by dissolving 0.8% agarose in 100 ml TAE with the help of microwave heating. After re-cooling to about 50°C, the solution was supplemented with 0.5 µg/ml ethidium bromide in TAE buffer and poured into a comb mounted gel tray for congelation. Samples containing 100 to 200 ng plasmid DNA were mixed with an equal volume of loading buffer (20 mM Tris/HCl pH 7.5, 50% glycerol, 0.1% bromophenol blue, 0.1% xylencyanol) and subsequently applied. Gels were run at 5 V/cm (voltage/interelectrode distance) for approximately 1 h. DNA fragments were visualized by fluorescence and relative to an DNA ladder evaluated.

3.4.7 Sequencing of PDS56/RBSII-VDACIHis

DNA sequencing reactions were carried out by using the ABI Prism BigDye™ Terminator Cycle Sequencing Ready Reaction Kit as recommended by Perkin Elmer™.

Sequencing reaction:

Plasmid DNA (200-500 ng)	2.0	µl
Sequencing primer (10 µM)*	1.5	µl
BigDye™	3.0	µl
H ₂ O, deionised	ad	20.0
		µl

*) Sequencing primers were designed to bind 200 bp away from the region of interest. Oligonucleotide syntheses was carried out by Metabion, Planegg-Martinsried.

Sequencing primers:

Primer:	Oligonucleotide sequence:
1	5'-ccctttcgtcttcacctcgagaaatc-3'
2	5'-cttaaagttcgttctagagtagtgtagtg-3'
3	5'-ctgatcttccacagtaatctcgg-3'
4	5'-agattgaccctgacgcctgc-3'

*) Oligonucleotide syntheses was carried out by Metabion, Planegg-Martinsried.

Sequencing program:

96 °C		3.0 min
96 °C	} 30 cycles	0.5 min
45 °C		0.5 min
60 °C		4.0 min

Afterwards, the samples were diluted with 20 µl dH₂O and purified with AutoSeq™ G-50 disposable spin columns according to Perkin Elmer™. Sequence analysis by gel-electrophoresis was carried out by the scientific service of the MPI of Biochemistry. Sequence verifications were performed with the program Staden package (MRC Laboratory of Molecular Biology, Cambridge, United Kingdom).

3.4.8 Site directed mutagenesis of HVDAC1

Hvdac1-his₆ point mutations were introduced by the QuickChange® site-directed mutagenesis kit according to the protocol of Stratagene™. For introduction of the indicated point mutations the following primer pairs were used. Double and multi mutants were consecutively achieved by introduction of a further point mutation in the already mutated host plasmids. Successful mutagenesis was approved by DNA sequence analysis.

Mutagenesis reaction:

Plasmid DNA (10 ng)	2.0 µl
Oligonucleotide primer #1 (10 µM)*	1.5 µl
Oligonucleotide primer #2 (10 µM)*	1.5 µl
Reaction buffer (10×)	5.0 µl
dNTP mix	1.0 µl
QuikSolution	3.0 µl
H ₂ O, deionised	ad 50.0 µl

*) Oligonucleotide syntheses was carried out by Metabion, Planegg-Martinsried.

Mutagenesis program:

95 °C		1.0 min
95 °C	} 18 cycles	50 sec
60 °C		50 sec
68 °C		5.0 min
68 °C		7.0 min

Oligonucleotide primer pairs:

pDS56/RBS2-HVDAC1His6/[mutant]	pDS56/RBS2-HVDAC1His6/[host]	Primer pair:
C130S	nativ	5'-gagcacattaacctgggctccgacatggatttcgacattg-3' 5'-caatgtcgaaatccatgtcggagcccagggttaatgtgctc-3'
C235S	nativ	5'-gattgacctgacgcctccttctcggctaaagtg-3' 5'-cactttagccgagaaggaggcgtcagggtcaatc-3'
C130S/C235S	C130S	5'-gattgacctgacgcctccttctcggctaaagtg-3' 5'-cactttagccgagaaggaggcgtcagggtcaatc-3'
S49C/C130S/C235S	C130S/C235S	5'-gaatttacaagctcaggctgcccacactgagaccacc-3' 5'-gggggtctcagtggtggcgcaagcctgagcttgtaaatc-3'
S107C/C130S/C235S	C130S/C235S	5'-ccttcgattcatccttctgcccctaactggg-3' 5'-cccagtgtagggcagaaggatgaatcgaagg-3'
S196C/C130S/C235S	C130S/C235S	5'-cagagtttggcggctgcatcttaccagaaa-3' 5'-cttctcggtaaatgcaagcccaactctg-3'
S263C/C130S/C235S	C130S/C235S	5'-gtattaaactgacactgtgccccttctggatggcaag-3' 5'-cttgccatccagaagagcgcaagcagtgctcagtttaatac-3'
V20C/C130S	C130S	5'-caaatctgccagggatgcttcaccaagggctatg-3' 5'-catagcccttggtgaagcaatccctggcagatttg-3'
C130S/C235A	C130S	5'-gattgacctgacgcctccttctcggctaaagtg-3' 5'-cactttagccgagaaggaggcgtcagggtcaatc-3'
L34M/C235S	C235S	5'-gcttaataaagcttgatgatgaaaacaaaatctgagaatg-3' 5'-cattctcagattttgttttcatatcaagctttattaagc-3'
L13M	native	5'-ccacgtatgccgatatgggcaaatctgccag-3' 5'-ctggcagatttgcccatatcggcatacgtg-3'
I230M	native	5'-gcagccaagtatcagatggaccctgacgcctgc-3' 5'-gcaggcgtcagggtccatctgatacttggctgc-3'
I88M	native	5'-ctaggcaccgagatgactgtggaagatc-3' 5'-gatcttccacagtcatctcgggtgctag-3'
L13M/V20M	L13M	5'-caaatctgccagggatgcttcaccaagggctatg-3' 5'-catagcccttggtgaacatcctcctggcagatttg-3'
L13M/L34M	L13M	5'-ggatttgcttaataaagcttgatgatgaaaacaaaatctgagaatggattgg-3' 5'-ccaatcattctcagattttgttttcatatcaagctttattaagccaaatcc-3'
L13M/L42M	L13M	5'-caaatctgagaatggaatggaatttacaagctcagg-3' 5'-cctgagcttgtaaatccattccattctcagattttg-3'
L13M/L61M	L13M	5'-ccaaagtacgggcagatggaaccaagtacagatg-3' 5'-catctgtacttggtttcactactgcccgtcactttgg-3'
L13M/L72M	L13M	5'-gatggactgagtacggcatgacgtttacagaaaatg-3' 5'-catttctctgtaaacgtcatgcccgtactcagtcacc-3'
L13M/I117M	L13M	5'-gggaaaaaaatgctaaaatgaagacagggtacaagcgg-3' 5'-ccgcttgtagcctgtcttcatcttagcatttttttccc-3'
L13M/V187M	L13M	5'-ccagcttcacactaatatgaatgacgggacagagtttg-3' 5'-ccaaactctgtcccgtcatcatttagtggaagctgg-3'
L13M/L240M	L13M	5'-gcttctcggctaaaatgaacaactccagc-3' 5'-gctggagttgttcatcttagccgagaagc-3'
L13M/L254M	L13M	5'-ggtttaggatacactcagactatgaagccaggtattaactgacac-3' 5'-gtgtcagtttaatacctggcttcatagctcagtgatcctaacc-3'
L13M/L282M	L13M	5'-caagcttggtctaggaatggaatttcaagcaagatc-3' 5'-gatcttgcttgaattccattcctagaccaagcttg-3'

3.4.9 Preparation of *E. coli* DL39 [prep4]

E. coli DL39 was transformed with the prep4 repressor plasmid isolated from *E. coli* Δ M15. Transformants of *E. coli* DL39 [prep4] clones were grown in 6 ml LB^{Kan} overnight, supplemented with 7% sterile DMSO, flash frozen in liquid N₂ and stored at -70 °C until use.

3.5 Protein expression and purification

3.5.1 Heterologous expression of HVDAC1 in *E. coli*

3.5.1.1 Overproduction of HVDAC1 in *E. coli* M15 [prep4]

Two liters of TB^{Amp/Kan} were inoculated from a 100 ml culture of PDS/RBSII-VDAC1His₆ transformed *E. coli* M15 [prep4] cells and incubated in 5 l baffled Erlenmeyer flasks at 37 °C and 200 rpm. HVDAC1 inclusion body formation was induced by the addition of 1 mM IPTG at an OD₆₀₀ of 0.8 AU and further incubation at 37 °C and 200 rpm. After an induction period of 4 h, cells were harvested by centrifugation at 5000 g for 30 min., shock frozen in liquid N₂ and stored at -70 °C until further use.

3.5.1.2 Overproduction of selenomethionine labelled HVDAC1 in *E. coli* M15 [prep4]

Selenomethionine labelled HVDAC1 was produced by using the feedback inhibition of the methionine biosynthesis pathway^[88]. A culture of *E. coli* M15 [prep4] / pDS/RBSII-VDACHis₆ was grown on M9^{Amp/Kan} at 37 °C and 200 rpm overnight. From this culture 1.5 l of M9^{Amp/Kan} were inoculated to an OD₆₀₀ of 0.1 AU and incubated in a baffled 5 l Erlenmeyer flasks at 37 °C and 200 rpm. At an OD₆₀₀ of 0.6 the culture was supplemented with 150 mg lysine, 150 mg phenylalanine, 150 mg threonine, 75 mg isoleucine, 75 mg leucine and 90 mg selenomethionine. After further incubation for 15 min. 1 mM IPTG was added. Following an induction period of 12 h, cells were harvested by centrifugation at 5000 g for 30 min., shock frozen in liquid N₂ and stored at -70 °C until further use.

3.5.1.3 Overproduction of ²H, ¹⁵N and ¹³C labelled HVDAC1 in *E. coli* M15 [prep4]

A 20 ml culture of *E. coli* M15 [prep4] / pDS/RBSII-VDACHis₆ was grown on M9^{Amp/Kan} at 37 °C and 200 rpm overnight. In order to adapt the culture to D₂O, the cells were consecutively inoculated to ²H-M9^{Amp/Kan} of an increasing D₂O content of 70, 80 and 100%. At each step the cells were incubated for 24 h at 37 °C and 200 rpm.

Subsequent to adaption, an 1.5 l culture of [^2H , ^{15}N]-M9^{Amp/Kan} or [^2H , ^{15}N , ^{13}C]-M9^{Amp/Kan} was inoculated to an OD₆₀₀ of 0.1 AU and incubated in baffled 5 l Erlenmeyer flasks at 37°C and 200 rpm. HVDAC1 inclusion body formation was induced by adding 1 mM IPTG at an OD₆₀₀ of 0.8 AU and further incubation at 37°C and 200 rpm. Following an induction period of 8 h cells were harvested at 5000 g for 30 min., shock frozen in liquid N₂ and stored at -70°C until further use.

3.5.1.4 Overproduction of selective amino acid labelled HVDAC1 *E. coli* in DL39 [prep4]

Cultures of *E. coli* DL39 [prep4] / pDS/RBSII-VDACHis6 were grown overnight in partially deuterated AES^{Amp/Kan} at 37°C and 200 rpm. In order to adapt the culture to D₂O, cells were consecutively inoculated to AES^{Amp/Kan} media with an increasing D₂O content of 70, 80 and 100%. During each step the cultures were incubated for 24 h at 37°C and 200 rpm. Subsequent to adaption, a further culture of 2.0 l AES^{Amp/Kan} was inoculated at an OD₆₀₀ of 0.1 AU and incubated in a baffled 5 l Erlenmeyer flask at 37°C and 200 rpm. At an OD₆₀₀ of 0.5 AU, cells were harvested by centrifugation at 5000 g for 30 min. and resuspended in 500 ml ^2H -M9. Afterwards the cells were harvested again at 5000 g for 30 min., resuspended in 500 ml AES^{Amp/Kan} and further incubated in a baffled 2.5 l Erlenmeyer flask at 37°C and 200 rpm. After 45 min. of incubation the culture was supplemented with the labelled amino acid (see 3.3.6) and following further 15 min. with 1 mM IPTG. Following an induction period of 12 h, cells were harvested by centrifugation at 5000 g for 30 min., shock frozen in liquid N₂ and stored at -70°C until further use.

3.5.2 Purification and refolding of HVDAC1 inclusion bodies

All HVDAC1-His₆ samples were purified and refolded according to the following protocol.

3.5.2.1 Purification of HVDAC1 inclusion bodies

Cells were resuspended in 100 mM Tris/HCl pH 7.5; 1 mM EDTA; 5 mM DTT, 100 mM NaCl, 0.2 mM PMSF and incubated with 0.1 mg/ml lysozyme for 0.5 h. After addition of 1 mM MgCl₂, 0.1 mM MnCl₂ and 0.05 mg/ml DNase I the cells were finally disrupted by two *French press* passes. Subsequently, the inclusion bodies were harvested by centrifugation at 5000 g for 30 min. at 4°C. The gained pellet was resuspended in 100 mM Tris/HCl pH 7.5; 1 mM EDTA; 1 mM DTT, 100 mM NaCl, 0.2 mM PMSF, supplemented with 3% v/v OPOE, stirred for 2 h at room temperature and again harvested at 5000 g for 30 min. at 4°C. To remove residual detergent the pellet was resuspended in 100 mM Tris/HCl pH 7.5; 1 mM EDTA; 1 mM DTT, 100 mM NaCl, 0.2 mM PMSF and centrifuged at 5000 g for 30 min. at 4°C.

Inclusion bodies were dissolved in 100 mM Tris/HCl pH 7.5; 1 mM EDTA; 5 mM DTT, 6 M guanidinium chloride. Insoluble material was removed by centrifugation at 100 000 *g* for 45 min. Finally, the HVDAC1 protein containing supernatant was adjusted to a protein concentration of 15 mg/ml with 100 mM Tris/HCl pH 7.5; 1 mM EDTA; 5 mM DTT, 6 M guanidinium chloride and stored at -70 °C until use.

3.5.2.2 Refolding of denatured HVDAC1

HVDAC1 refolding was performed at 4 °C by drop-wise dilution of the dissolved inclusion bodies in 100 mM Tris/HCl pH 8.0; 1 mM EDTA; 5 mM DTT; 1% w/v LDAO until a final concentration of 0.6 M guanidinium chloride was reached. The solution was stirred over night at 4 °C, centrifuged at 100 000 *g* for 45 min. and finally 5-fold diluted with 100 mM sodium phosphate pH 7.5.

3.5.3 Purification of refolded HVDAC1 for NMR investigations

Refolded HVDAC1 was applied to a 5 ml Ni²⁺-SephacroseHP column (GE Healthcare), washed with 25 ml of 20 mM sodium phosphate pH 7.5; 20 mM imidazole; 0.2% LDAO and afterwards eluted with 50 ml of 20 mM sodium phosphate pH 7.5; 300 mM imidazole; 0.2% LDAO.

3.5.3.1 Preparation of HVDAC1 NMR samples

HVDAC1 containing fractions were identified by SDS PAGE and pooled. The protein concentration of the pooled fraction was determined at a wavelength 280 nm. Subsequently, the LDAO content of the HVDAC1 pool was based on the calculated protein concentration in such a way adjusted that it will add to 6% after concentration of the protein sample to 0.6 mM. The volume of required LDAO was calculated as follows.

$$V_S = V_0 \cdot \frac{C_0 - C_{F^0} \cdot \frac{C_P}{C_{PF}}}{C_{F^0} \cdot \frac{C_P}{C_{PF}} - C_S}$$

v_s : supplemented LDAO volume [ml]

v_0 : volume HVDAC1-His₆ sample [ml]

c_0 : LDAO concentration sample [%]

c_{F^0} : final LDAO concentration [6%]

c_P : protein concentration sample [mM]

c_{PF} : protein concentration final [0.6 mM]

c_S : LDAO concentration stock solution [15%]

After LDAO addition the samples were dialysed against 25 mM BisTris-HCl pH 6.5, 0.2% LDAO for 4 h and concentrated with a centrifugal filter device (Amicon Ultra- 30K, Millipore) to a final protein content of 0.6 mM HVDAC1. NMR samples were further supplemented by 0.05% sodium azide and stored at 4°C until measurement.

3.5.3.2 MTSL-labeling of HVDAC1 NMR samples

Single cysteine mutants of HVDAC1 were modified at the cysteine sulfhydryl group by the paramagnetic thiol-specific nitroxide spin label (1-oxy-2,2,5,5-tetramethyl-3-pyrroline-3-methyl)-methanethiosulfonate (MTSL). HVDAC1 samples were supplemented with a 3 to 5-fold molar excess of MTSL (100 µg/µl dissolved in ice cold acetone) either before or after refolding and purification. Afterwards the samples were incubated at room temperature for 1.5 h in the dark. Unbound spin label was removed by dialysis. Effective spin labeling was verified by ESI-MS.

3.5.4 Preparation of refolded HVDAC1 for crystallisation

3.5.4.1 Purification of refolded HVDAC1 for crystallisation trials

Refolded HVDAC1 was applied to a 5 ml Ni²⁺-SepharoseHP column (GE Healthcare), and washed with 100 ml of 20 mM sodium phosphate pH 7.5; 20 mM imidazole; 0.8% v/v OPOE. Afterwards, HVDAC1 was eluted with 50 ml 20 mM sodium phosphate pH 7.5; 300 mM imidazole; 0.8% v/v OPOE. Protein containing fractions were verified by SDS-PAGE, pooled and concentrated to 10 mg/ml by a centrifugal filter device with a molecular cut-off of 30 kDa.

3.5.4.2 Detergent exchange

Purified HVDAC1 fractions were divided into 500 µl aliquots and supplemented with different detergents as indicated below. The different aliquots were dialysed against 50 ml of 25 mM BisTris-HCl pH 6.8 including the respective detergent in the indicated concentration. Dialysis was carried out in cellulose membrane dialysis tubes with a molecular cutoff of 10 kDa for 60 h at 4°C. After dialysis HVDAC1 samples were centrifuged at 20 000 g for 30 min. and stored at 4°C until crystallisation.

Detergents used:

Detergent	trivial name	applied conc. [%]
n-octyltetraoxyethylene	C ₈ E ₄	2.0
n-octaethylene glycol monododecylether	C ₁₀ E ₈	0.2
nonaethylene glycol monododecylether	C ₁₂ E ₉	0.2
n-octyl-polyoxyethylene;	OPOE	0.8
n-octyl- -D-glucopyranoside	OG	1.5
n-nonyl- -D-glucopyranoside	NG	0.5
n-nonyl- -D-maltopyranoside	NM	0.9
n-decyl- -D-maltopyranoside	DM	0.2
n-undecyl- -D-maltopyranoside	UM	0.2
n-dodecyl- -D-maltopyranoside	DDM	0.5
N,N-dimethyldecyl-amine-β-oxide	DDAO	0.5
N,N-dimethyldodecyl-amine-β-oxide	LDAO	0.2
cyclohexyl-propyl- -D-maltoside	Cymal-3	2.0
cyclohexyl-butyl- -D-maltoside	Cymal-4	0.6
cyclohexyl-pentyl- -D-maltoside	Cymal-5	0.2
cyclohexyl-hexyl- -D-maltoside	Cymal-6	0.2

3.5.4.3 Crystallisation of HVDAC1

Crystallisation trials were carried out by the hanging drop vapor diffusion method in 24 well VDXM™ plates. Initial screening was performed using the crystallisation screens Crystal screen™, Crystal screen 2™, Crystal screen light™, Membfac™, PEG/Ion™, Index™ and SaltRx™. To set up a crystallisation reaction, 1.5 µl of HVDAC1 sample were mixed with 0.75 µl precipitant solution and placed on top of 0.5 ml precipitant solution. Reactions were incubated at 18 °C and regularly followed for crystal formation by a stereo microscope. Successful conditions were screened for further optimisation by utilisation of the Additive™- and the Detergent-screens I-III™. For optimization, 1.5 µL HVDAC1 sample was mixed with 0.75 µl of the appropriate precipitant, supplemented by 0.25 µl of the additive or detergent solution and incubated as described above. Heavy metal incorporation was carried out by soaking HVDAC1 crystals with platinum derivatives of the heavy atom screen PT™ as recommended by Hampton Research™.

3.5.5 Overproduction and purification of mouse His₆-BID

3.5.5.1 Overproduction of mouse His₆-BID in *E. coli* BL21 (DE3)-RIPL

20 ml cultures of pet23d-HisBid transformed *E. coli* BL21CodonPlus (DE3)-RIPL cells were grown overnight in LB^{Amp/Cam} at 37 °C and 200 rpm. From this culture 2 l of TB^{Amp/Cam} were inoculated to an OD₆₀₀ of 0.05 AU and incubated in a baffled 5 l Erlenmeyer flask at 37 °C and 200 rpm. Adding 1 mM IPTG at an OD₆₀₀ of 1.2 AU and further incubation at 37 °C and 200 rpm induced mouse His₆-Bid expression. Following an induction period of 4 h cells were harvested by centrifugation at 5000 *g* for 30 min., shock frozen in liquid N₂ and stored at -70 °C until further use.

3.5.5.2 Overproduction of ²H and ¹⁵N labelled His₆-BID in *E. coli* BL21 (DE3)-RIPL

100 ml cultures of pet23d-HisBid transformed *E. coli* BL21CodonPlus (DE3)-RIPL cells were grown overnight on M9^{Amp/Cam} at 37 °C and 200 rpm. In order to adapt the culture to D₂O, the cells were consecutively inoculated in ²H-M9^{Amp/Kan} with an increasing D₂O content of 70, 80 and 100%. During each step the cultures were incubated at 37 °C for 24 h. Subsequent to adaption 1.5 l of ²H-M9^{Amp/Cam} or [²H,¹⁵N]-M9^{Amp/Cam} were inoculated to an OD₆₀₀ of 0.1 AU. Cultures were incubated in baffled 5 l Erlenmeyer flasks at 37 °C and 200 rpm. Adding 1 mM IPTG at an OD₆₀₀ of 0.8 AU and further incubation at 37 °C and 200 rpm induced mouse His₆-Bid expression. After an induction period of 8 h cells were harvested by centrifugation at 5000 *g* for 30 min., shock frozen in liquid N₂ and stored at -70 °C until further use.

3.5.5.3 Purification of His₆-BID

Cells were resuspended in 20 mM sodium phosphate pH 7.5; 1 mM EDTA; 150 mM NaCl, 5 mM DTT and disrupted by two *French press* passes. After sedimentation of the cellular debris by ultra centrifugation at 120 000 *g* for 45 min. the supernatant was applied to a 5 ml Ni²⁺-SephacroseFF column (GE Healthcare) and washed with five column volumes of 20 mM sodium phosphate pH 7.5; 1 mM DTT. Elution of His₆-BID was carried out with 20 mM sodium phosphate pH 7.5; 1 mM DTT; 300 mM imidazole. His₆-Bid containing fractions were identified by SDS-PAGE, pooled and concentrated to a total volume of 4 ml by a centrifugal filter device (molecular cutoff of 10 kDa). The sample was then applied to a Superdex 75 gel filtration column (GE Healthcare) equilibrated with 25 mM Tris-HCl pH 7.5. His₆-Bid containing fractions were verified by SDS-PAGE, pooled and concentrated to a protein concentration of 5 mg/ml by a centrifugal filter device. The sample was finally supplemented with 30% glycerol, flash frozen in liquid N₂ and stored at -70 °C until use.

3.5.5.4 Cleavage of His₆-BID by Caspase8

Cleavage of His₆-BID by Caspase8 was carried out in analogy to an already described protocol^[89]. Caspase8 (7.7 µl/µg) was a friendly gift from the Serono Pharmaceutical Research Institute, Geneva, Switzerland. 5 mg/ml of His₆-BID were 1:1 diluted with 50 mM Hepes-NaOH pH 7.5; 100 mM NaCl; 10 mM DTT; 10% sucrose and supplemented with 12.5 µl of Caspase8. The sample was incubated for 2 h at 20°C and afterwards applied to a 1 ml Ni²⁺-SepharoseFF column (GE Healthcare).

Following a wash step with 5 column volumes of 50 mM Hepes-NaOH pH 7.5; 100 mM NaCl; 10% sucrose, cleaved His₆-cBID was eluted by 5 column volumes of 50 mM Hepes-NaOH pH 7.5; 100 mM NaCl; 10% sucrose; 300 mM imidazole. Cleavage efficiency was verified by SDS-PAGE. Cleaved samples were dialysed against 25 mM Tris-HCl pH 7.5; 30% glycerol, shock frozen in liquid N₂ and stored at -70°C until use.

3.5.6 Purification of bovine adenosine nucleotide translocator (ANT) from bovine heart

3.5.6.1 Purification of mitochondria from bovine heart

All steps were carried out on ice in the cold room. A slaughter-warm bovine heart was obtained from the Munich slaughterhouse and immediately cooled in ice water. The 3.5 kg heart was after fat and tendons removal diced and subsequently minced by a meat grinder. The mincemeat was then suspended in 4 l of 20 mM Hepes-NaOH pH 7.2, 250 mM sucrose.

Cell disruption was carried out in a pre-cooled blender for 45 sec at low speed. To sediment the cell debris the suspension was twice centrifuged at 600 g for 15 min. at 4°C. The mitochondria were then sedimented at 12 000 g for 45 min. at 4°C and subsequently carefully resuspended in 100 ml of 20 mM Hepes-NaOH pH 7.2, 250 mM sucrose. For absorption measurements, the resuspension was 50-fold diluted in 10 mM Tris-HCl pH 7.5; 0.1% SDS and measured at wavelengths at 280 and 310 nm, respectively. The total mitochondrial protein content was estimated as follows^[90].

$$c_{\text{mito}} = \frac{A_{280} - A_{310}}{1.05} \quad c_{\text{mito}}: \text{Total mitochondrial protein [mg/ml]} \quad (2)$$

To stabilize ANT, the mitochondrial suspension was supplemented with 4 µmol atractyloside/mg total protein, incubated at 20°C for 20 min. and pelletised at 9000 g for 10 min. at 4°C. Finally, the mitochondria were resuspended in 100 ml 20 mM Hepes-NaOH pH 7.2, 250 mM sucrose, flash frozen in liquid N₂ and stored at -70°C until use.

3.5.6.2 Purification of BANT from bovine heart mitochondria

Mitochondria of 50 mg total protein were harvested at 9000 *g* for 10 min. and resuspended in 5 ml 10 mM Tris-HCl pH 7.4; 500 mM NaCl; 1 mM EDTA. After adding 20 mM of carboxyattractyloside the suspension was incubated for 10 min. on ice. Mitochondria were lysed by the addition of 2% 3-Laurylamido-N,N'-dimethylpropyl amine oxide (LAPAO) and subsequent incubation overnight on ice. Purification was carried out on a 50 ml hydroxyapatite/celite column, pre-equilibrated with 10 mM Tris-HCl pH 7.4; 500 mM NaCl; 1 mM EDTA; 0.05% w/v LAPAO. After sample application the protein containing flowthrough was collected, constricted to a total volume of 5 ml by a centrifugal filter device (molecular cut-off of 10 kDa) and applied to a Superdex 75 16/60 column equilibrated with 10 mM Tris-HCl pH 7.4; 100 mM NaCl; 1 mM EDTA; 0.05% w/v LAPAO. BANT containing fractions were verified by SDS-PAGE, concentrated to 1 mg/ml by a centrifugal filter device (molecular cut-off of 10 kDa) and stored at 4 °C until use.

3.5.7 Further utilised proteins

Bax was a kindly gift from Stephanie Bleicken, MPI of Biochemistry, Dept. of Membrane Biochemistry, Martinsried, Germany. Caspase-8 was kindly provided by Dr. Bruno Antonsson, Serono Pharmaceutical Research Institute, Geneva, Switzerland. Human Bcl-X_L, Bid and Hexokinase II peptides were provided by Dr. K. Zeth, Max-Planck Institute for Developmental Biology, Tübingen, Germany.

3.6 Protein analytical methods

3.6.1 Determination of protein concentrations

Protein concentrations were calculated on the basis of the absorption at 280 nm according to the law of Lambert-Beer. Protein solutions which exceed an absorption unit (AU) of 1 were diluted or measured in cuvettes of shorter path lengths. For purified proteins the extinction coefficients were calculated on basis of the corresponding primary sequences by using the ProtParam online tool (<http://www.expasy.ch/tools/protparam.html>). For protein mixtures the protein concentration was roughly estimated to 1 [mg/ml]/1 AU.

Calculated extinction coefficients ϵ_{280} ($M^{-1} \text{ cm}^{-1}$)	Protein	ϵ_{280} ($M^{-1} \text{ cm}^{-1}$)
	HVDAC1	36960
	MBID	8370
	BANT	45630

3.6.2 SDS-Polyacrylamide gel-electrophoresis (SDS-PAGE) of proteins

Analytical gel-electrophoresis was performed under denaturing conditions in a discontinuous buffer system. Protein separation was carried out in acrylamide/bisacrylamide gels composed of a stacking gel (7% v/v acrylamide/bisacrylamide) upstream connected to a separation gel (13% or 17% acrylamide/bisacrylamide) or in NuPAGE® Novex gradient gels (4-12% acrylamide/bisacrylamide). Protein samples of 5 to 10 mg total protein were mixed with 5-fold sample buffer (0.5 M Tris-HCl pH 6.8; 10% glycerol; 2.3% SDS; 5% DTT; 0.1% bromophenol blue) and heated for 10 min. at 40 °C (membrane proteins) or 100 °C (soluble proteins). Electrophoresis was performed at about 15 V/cm until the dye front reached the end of the gel. Protein bands were visualised by staining (0.025% Coomassie brilliant blue R250; 25% ethanol; 8% acetic acid) and subsequent destaining (30% methanol; 10% acetic acid) in the corresponding solutions.

3.6.3 N-terminal sequencing

N-terminal sequencing by Edman degradation was performed by the scientific service of the Max-Planck Institute of Biochemistry, Martinsried, Germany. Proteins were either directly sequenced from solution or from redissolved crystals. In case of the latter up to 10 protein crystals were collected, in reservoir solution washed and subsequently redissolved in 0.1% trifluoroacetic acid.

3.6.4 Protein mass spectrometric analysis

3.6.4.1 High performance liquid chromatography/mass spectrometry (HPLC/ESI-MS)

Reversed phase high performance liquid chromatography/mass spectrometry (HPLC/MS; Perkin Elmer) was used to determine protein masses. Protein samples of about 1 mg/ml were applied to a 100x5 mm C8 HD 125/5 reverse phase column (Macherey and Nagel). For gradient elution the HPLC was programmed as follows: Equilibration at 5% solvent B; linear gradient: 0 min., 5% solvent B; 15 min.: 90% solvent B (solvent A: 0.05% (v/v) trifluoroacetic acid (TFA) in water; solvent B: 0.05% (v/v) TFA in acetonitrile).

The protonated protein molecules were detected in the positive ion electrospray ionization (ESI) mode as they elute from column during the acetonitril/water gradient. Mass analysis was done separately at m/z-windows of 600-2000.

3.6.4.2 Peptide mass fingerprint analysis

After SDS-PAGE and staining selected protein bands were cut out in gel pieces and fully destained by a three times alternating incubation in 100 μ l 50% acetonitrile and 100 μ l 50 mM ammonium bicarbonate for 15 min. each. Cysteine carboxymethylation was performed by incubation of the gel pieces consecutively in 100 μ l 10 mM DTT, 50 mM ammonium bicarbonate at 56°C for 45 min. and then in 100 μ l 55 mM iodoacetic acid, 50 mM ammonium bicarbonate at room temperature for 30 min. The gel pieces were subsequently washed by the repetition of the destaining steps, dried in a speedvac and rehydrated in 50 mM ammonium bicarbonate, 10 μ g/ μ l trypsin for protein digestion over night. Thereafter the gel pieces were consecutively shaken in 50 μ l ddH₂O, 50 μ l 50% acetonitrile, and at least 50 μ l acetonitrile, 0.1% trifluoroacetic acid for 20 min. each. The digestion and all washing solutions were combined, shock frozen in liquid N₂ and dried in a speedvac. Desalting was achieved by twofold re-dissolving in 100 μ l ddH₂O, refreezing in liquid N₂ and drying in a speedvac. The pellet was dissolved in 10 μ l 33% acetonitril, 0.1% trifluoroacetic acid, supersonic sounded for 10 sec and centrifuged for 15 min. at 20 000 *g*. Samples were mixed with a matrix (ACCA Bruker) in an 1:1 ratio of 1 μ l in total by a MALDI AutoPrep Robot System (Bruker Daltonics, Bremen) and subsequently spotted on a MALDI steel target. Mass analysis was carried out in comparison to applied standards by MALDI-MS on a Reflex III mass spectrometer (Bruker Daltonics). Data analysis was carried out with the programm MASCOT peptide mass fingerprint (Matrix science, London, United Kingdom).

3.6.5 Secondary structure determination by circular dichroism spectroscopy

CD spectra of HVDAC1 samples (0.20 mg/ml Protein in 10 mM Tris/HCl pH 8 supplemented with 0.2% LDAO) were recorded on a Jasco J-810 spectrophotometer in a 0.1 mm quartz cuvette at 4°C. 10 spectra were accumulated per data set, using a data pitch of 0.1 nm, scan speed 20 nm/s, 1 nm slit width and a response time of 2 sec. Analysis of the spectra was carried out using the deconvolution software suite CDpro (<http://lamar.colostate.edu/~sreeram/CDPro/index.shtml>).

3.6.6 Reconstitution of HVDAC1 in planar bilayer membranes and conductivity measurements

The experiments were performed in cooperation with the department of Biophysics at the University of Stuttgart^{[51][91]}. Briefly, planar lipid membranes were formed from a 1% (w/v) solution of diphytanoyl-phosphatidyl-choline (Avanti Polar Lipids, Alabaster, AL) dissolved in n-decane/butanol (9:1 v/v), spread across a circular hole (area about 1 mm²) in the thin wall of a Teflon cell that separates two aqueous compartments filled with 1 M KCl solution.

1-10 µg of HVDAC1 in 20 mM sodium phosphate buffer pH 7, 0.2% cymal-5 were added and voltages of ±10 mV to ±100 mV were applied. Membrane currents were measured with a pair of Ag/AgCl electrodes (World Precision, Berlin, Germany or Metrohm, Herisau, Germany) using a HEKA EPC8 amplifier (HEKA, Lambrecht, Germany) or a Keithley 428 current amplifier (Keithley Instruments Inc., Cleveland, OH). Amplified signals were filtered at 3 kHz, monitored with an analog/digital storage oscilloscope and recorded with a strip chart recorder or alternatively digitized with a CED 1401 analog/digital converter (Cambridge Electronic Design, Cambridge, Great Britain) and recorded and stored on PC using the WinEDR version 2.4.8 software package (J. Dempster, University of Strathclyde, Glasgow, Great Britain). Single channel analysis was carried out by using the Origin 7.5 software package (OriginLab Corporation, Northampton, MA).

3.6.7 Analysis of protein-protein interactions by chemical and light-induced crosslinking

Protein-protein interactions of HVDAC1 with BID, cBID and ANT were analysed by chemical and light induced crosslinking. Before use, all proteins were separately dialysed against 20 mM BisTris-HCl pH 6.8; 0.2% cymal-5. Potential protein-protein interactions were identified in comparison to their untreated references by SDS-PAGE. The oligomeric nature of positive interactions was further investigated by peptide mass fingerprint analysis. In all reactions, the concentration of each individual protein was adjusted to about 12.5 µM.

3.6.7.1 Chemical crosslinking

Proteins were equimolar mixed in the desired combinations and incubated in a total volume of 50 µl for 4 h at 37°C. 25 µl of each sample were then supplemented by glutaraldehyde to a final concentration of 0.03% and incubated at 30°C for 15 min. The reaction was stopped by adding of 7 µl 0.5 M Tris-HCl pH 6.8; 10% glycerol; 2.3% SDS; 5% DTT; 0.1% bromophenol blue and subsequent heating at 100°C for 10 min.

3.6.7.2 Light-induced crosslinking

With minor modifications, Light-induced crosslinking was performed as described elsewhere^[92]. Proteins were equimolar mixed in the desired combinations and incubated in a total volume of 50 µl for 15 min. at 37°C. 34 µl of the sample were then supplemented in the dark with 4 µl of a 2.5 mM Tris(bipyridyl)-ruthenium(II)dichlorid ($\text{Ru}^{\text{II}}(\text{bipy})^3\text{Cl}_2$, Sigma) solution and 2 µl of a 25 mM ammonium persulfate solution.

The reaction mixture was immediately exposed for 0.1 sec. by a white light emitting 150 W xenon lamp (optical filters: GG400, KG3; $\lambda = 400\text{-}750\text{ nm}$) at a distance of 25 cm. To stop the reaction after exposure the samples were directly supplemented by 10 μl 0.5 M Tris-HCl pH 6.8; 10% glycerol; 2.3% SDS; 5% DTT; 0.1% bromophenol blue.

3.6.8 NMR spectroscopy

NMR measurements and analysis were carried out by the department of NMR based structural biology at the Max Planck Institute for Biophysical Chemistry in Göttingen. A summary of all measured HVDAC1 samples is tabularly summarised below. An advanced description of the HVDAC1 analysis could be received elsewhere^[93]. In brief, all spectra were recorded at 37°C on cryogenic probe head eqiped Bruker 600, 800 or 900 Mhz spectrometers. Three different TROSY-type triple resonance experiments (HNCA, HNCO and multiple quantum (mq) HNCOCA) as well as a ¹⁵N-edited ¹H-¹H NOESY-TROSY^[94] and a mixed-time parallel evolution HMQC-NOESY^[95] spectrum were recorded. The sample specific summary of the recorded spectra is given below. Paramagnetic relaxation enhancement (PRE) data were achieved by recording TROSY-HSQC spectra of MTSL-labelled HVDAC1 single cysteine mutants and their unlabeled references. Dynamics were studied by measuring steady state heteronuclear ¹⁵N{¹H}-NOEs with a TROSY version in an interleaved manner^[96]. The molecular weight of the protein/micelle complex was estimated by ¹⁵N-edited 1D T1p experiments. Recorded NMR data were processed and analysed by M. Bayrhuber at the department of NMR based structural biology of the Max Planck Institute for Biophysical Chemistry, Göttingen, Germany. For processing and analysis the programs NMRPipe, NMRDraw^[97] and SPARKY (T. D. Goddard and D. G. Kneller, SPARKY 3, University of California, San Francisco, USA) were used.

HVDAC1-His₆ samples and recorded NMR spectra:

Sample:	Recorded spectra:
[² H(100%), ¹⁵ N]-HVDAC1-His ₆	TROSY-HSQC, HetNOE, T1p
[² H(100%), ¹⁵ N, ¹³ C]-HVDAC1-His ₆	TROSY-HSQC, TROSY-HNCA, TROSY-HNCO, mq-TROSY-HNCOCA, ¹⁵ N-NOESY-TROSY,
[² H(75%), ¹⁵ N, ¹³ C]-HVDAC1-His ₆	TROSY-HSQC, ¹⁵ N-NOESY-TROSY
[² H(75%), ¹⁵ N, ¹³ C]-HVDAC1-His ₆ in D ₂ O	TROSY-HSQC, ¹⁵ N-NOESY-TROSY
[² H(50%), ¹⁵ N, ¹³ C]-HVDAC1-His ₆	TROSY-HSQC, ¹⁵ N-NOESY-TROSY
[² H(75%), ¹⁵ N]-HVDAC1-His ₆ /C130S ± MTSL	TROSY-HSQC
[² H(75%), ¹⁵ N]-HVDAC1-His ₆ /C235S ± MTSL	TROSY-HSQC
[² H(75%), ¹⁵ N]-HVDAC1-His ₆ /C130S/V20C	TROSY-HSQC

Sample:	Recorded spectra:
[² H(75%), ¹⁵ N]-HVDAC1-His ₆ /C130S/V20C	TROSY-HSQC, 15N-NOESY-HMQC
[² H(75%), ¹⁵ N]-HVDAC1-His ₆ /C130S/C235S/S107C ± MTSL	TROSY-HSQC
[² H(75%), ¹⁵ N]-HVDAC1-His ₆ /C130S/C235S/S49C ± MTSL	TROSY-HSQC
[² H(75%), ¹⁵ N]-HVDAC1-His ₆ /C130S/C235S/S263C	TROSY-HSQC
[² H(75%), ¹⁵ N]-HVDAC1-His ₆ /C235S/L34C ± MTSL	TROSY-HSQC
[¹⁵ N, ¹³ C]-Leu, ¹⁵ N]-Met, [¹⁵ N, ¹³ C]-Ile, [² H]-HVDAC1-His ₆	TROSY-HSQC
[¹⁵ N]-Val, [² H]-HVDAC1-His ₆	TROSY-HSQC
[¹⁵ N]-Tyr, [² H]-HVDAC1-His ₆	TROSY-HSQC
[¹⁵ N]-Ala, [² H]-HVDAC1-His ₆	TROSY-HSQC
[¹⁵ N]-Lys, [² H]-HVDAC1-His ₆	TROSY-HSQC
[¹⁵ N]-Arg, [² H]-HVDAC1-His ₆	TROSY-HSQC
[² H(75%), ¹⁵ N]-HVDAC1-His ₆ + ATP	TROSY-HSQC
[² H(75%), ¹⁵ N]-HVDAC1-His ₆ + ADP	TROSY-HSQC
[² H(75%), ¹⁵ N]-HVDAC1-His ₆ + Fluoxetine (PROZAK)	TROSY-HSQC
[² H(75%), ¹⁵ N]-HVDAC1-His ₆ + [² H]-MBID	TROSY-HSQC
[² H(75%), ¹⁵ N]-HVDAC1-His ₆ + [² H]-MBID-MTSL	TROSY-HSQC
[² H(75%), ¹⁵ N]-HVDAC1-His ₆ + [² H]-cMBID	TROSY-HSQC
[² H(75%), ¹⁵ N]-HVDAC1-His ₆ + GdCl ₃	TROSY-HSQC

3.6.9 X-ray data collection and analysis

Native as well as selenomethionine and platinum derivatised HVDAC crystals were mounted in cryoloops™ and supplemented with an appropriate amount of an anti-freezing agent (glycerol, 2,3-butanediol or polyethylene glycol 400) if necessary. The crystals were flash frozen and stored under liquid N₂ until X-ray data collection. Native, SAD and MAD diffraction data were collected at the ESRF beamlines ID29, ID23-1 and the SLS beamline X10SA, respectively. Data collection was carried out by the oscillation method^[98] at 100 K. Diffraction data were integrated with MOSFLM^[99], XDS^[100] and d*TREK^[101]. Data scaling and merging was done with SCALA^[102] and prepared by SHELXC for heavy atom substructure determination in SHELXD^[103]. Refinement of selenium and platinum sites as well as the phase probability calculations were carried out in SHARP^[104]. Subsequent density modification using different values for solvent content was done with SOLOMON^[105]. Further phase improvement was attempted using inter-crystal averaging with DMMULTI^[106]. Structure solution was greatly supported by Dr. Clemens Vornrhein, Global Phasing Ltd., Cambridge, UK. Map interpretation was started by placing fragments of high-resolution beta barrel protein structures (<http://www.rcsb.org/pdb/home/home.do>; 1prn, 2f1c, 2fgq) in B-factor sharpened^[107] electron density maps by MOLREP^[108].

Subsequent placement of further beta-sheets and iterative model building and geometry refinement was performed with O^[109] and COOT^[110], respectively.

The extended molecular model of HVDAC1 was finally achieved by manual application of the NMR topology onto the X-ray derived model. Orientation and remodeling was carried out consistently to the interstrand HN-HN NOEs and the selenium sites of M132, M158 and M230 in COOT. Positioning of the predicted N-terminal helix was done by fitting a model helix into a corresponding portion of the electron density map. Orientation and fitting of the α -helix was verified through the selenium site of M13.

3.6.10 Alignments, secondary predictions and homology modelling

All alignments carried out by the protein multiple sequence alignment software MUSCLE^[111] set to the standard parameters. These alignments were carried out on the basis of a representative subset of animal, plant and fungal VDAC1 sequences collected from the protein knowledge base SWISSPROT (<http://www.expasy.org/sprot/>).

Secondary structural predictions of HVDAC1 were accomplished by the Protein Structure Prediction Server PSIPRED set to the standard parameters (<http://bioinf.cs.ucl.ac.uk/psipred/ute>).

Homology modeling of the NcVDAC and wheat VDAC1 topology was done on the basis of the HVDAC1 model. In accordance to the alignment derived from MUSCLE the individual residues of HVDAC1 were in silico mutated therefore. In silico mutation and remodeling was carried out in COOT^[110].

4 Results

4.1 Biochemical properties of HVDAC1

The human voltage dependent anion channel isoform 1 was overproduced from the pDS/RBS2-HVDAC1His6 plasmid in a modified form. The modifications affected the N-terminal region, due to the plasmid construction elongated by four amino acids, as well as the C-terminal region which was extended by two linker amino acids and six histidines with respect to an effective purification and detergent exchange (Fig. 4-1).

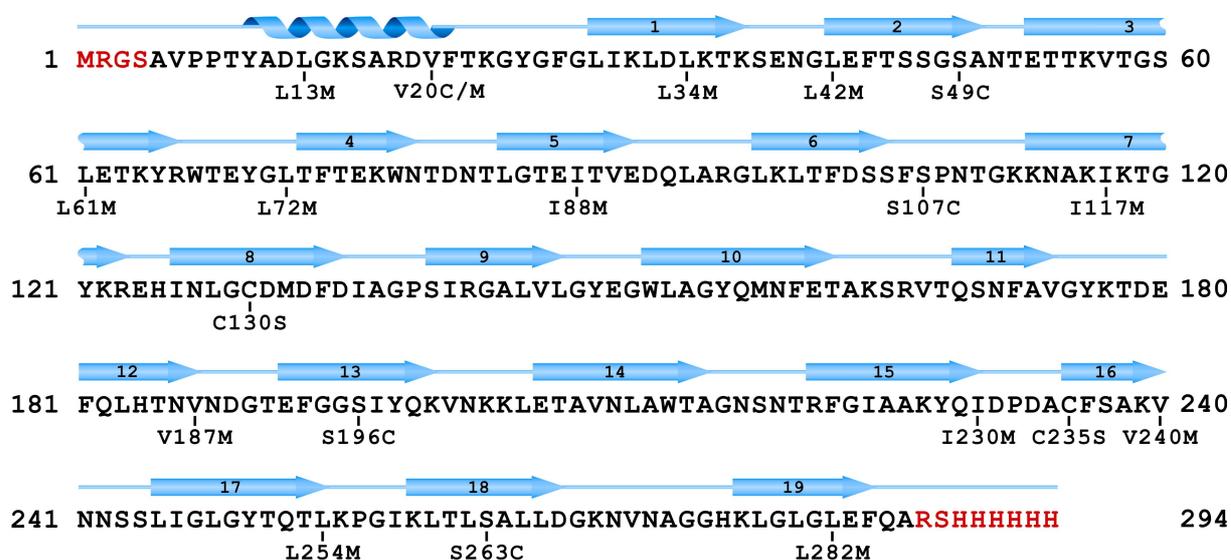


Figure 4-1: Amino acid sequence of the expressed HVDAC1.

The depicted amino acid sequence was translated from the *hvdac1* gene of pDS56/RBS2-HVDAC1His6 with the EXPASY translation tool TRASLATE. (<http://www.expasy.ch/tools/dna.html>). Differences between the natural human VDAC1 and the expressed protein are highlighted in red. Displayed secondary structure elements are depicted as predicted by the Protein Structure Prediction Server (PSIPRED; <http://bioinf.cs.ucl.ac.uk/psipred/ute>). Sequence variations of the generated HVDAC1 mutants are indicated by their position and amino acid alteration.

The HVDAC1 protein is comprised of 294 amino acids corresponding to a molecular weight of 32 139 Da. Calculations of the theoretical isoelectric point (pI) identifies HVDAC1 as a basic protein with a value of 9.0. This value is compared to the native channel ($pI_{\text{HVDAC1}} = 8.6$) slightly increased due to the added amino acids. With regard to the secondary structural content a computational sequence analysis predicted 19 β -sheets preceded by an N-terminal located α -helix. The predicted β -sheets are evenly distributed across the region of residue 27-294. About 54% of the total sequence are covered by this β -sheets which are comprised of 8.5 amino acids in average.

4.2 Overproduction, purification and refolding of HVDAC1

4.2.1 Overproduction of HVDAC1

All HVDAC1 samples intended for NMR structural studies had to be fully deuterated and ^{15}N -labelled according to its size. Moreover, for certain NMR experiments HVDAC1 had to be ^{13}C -labelled in addition. The required labelling was achieved by HVDAC1 overproduction in $[^2\text{H}, ^{15}\text{N}]$ -M9 and $[^2\text{H}, ^{15}\text{N}, ^{13}\text{C}]$ -M9 media, respectively. With doubling times of about 3 [h] the growth rates of *E. coli* in minimal and especially in fully deuterated minimal media were quite low. Furthermore, cell growth in this media even after exhaustive D_2O adaption reached only to an optical density (OD_{600}) of 1.7 AU at the best. Because of the low yield and the significant decreased growth rate during induction, cells were not induced before an OD_{600} of 0.9 AU was achieved and afterwards incubated for twelve hours. This method allowed to obtain about 3 g wet cell mass per litre medium.

The incorporation of specifically ^{15}N or $[^{15}\text{N}, ^{13}\text{C}]$ labelled amino acids into an otherwise deuterated HVDAC protein turned out to be more difficult. To avoid the scrambling of the ^{15}N -labelled amino group from the selected to arbitrary amino acids by *E. coli* intrinsic aminotransferases, these samples had to be produced in a transaminase negative strain. For this reason the transaminase negative *E. coli* strain DL39 was modified to contain the *lacI* encoding repressor plasmid [prep4] which is necessary for a tight regulation of the pDS56/RBSII based expression system. To achieve the required deuteration grade this strain had to be grown in presence of a deuterated algal lysate amino acid mixture. However, the applied algal extract naturally contains all amino acids and hence aggravates an efficient incorporation of a specific label. In order to still achieve an adequate label incorporation of at least 90%, the specifically labelled amino acids had hence to be added in tenfold excess. Because of the available quantity of the labelled amino acids this entailed, however, that in the media the applicable amount of algal extract had to be reduced to 0.1%. Under these limited conditions the constructed *E. coli* DL39 [prep4] strain only grew to a maximum OD_{600} of about 0.6 AU. The direct expression of HVDAC1 in this media hence became impossible due to the minimum of required cell mass. To avoid this problem, the required cell mass was produced in a higher supplemented AES medium in a first cultivation step. Harvesting and washing of this culture consequently provided sufficient cell mass for the amino acid specific labeling of HVDAC in a fourfold reduced volume of algal extract limited medium. This strategy finally led to a yield of 3 g of wet cell mass per 0.5 litre of expression culture.

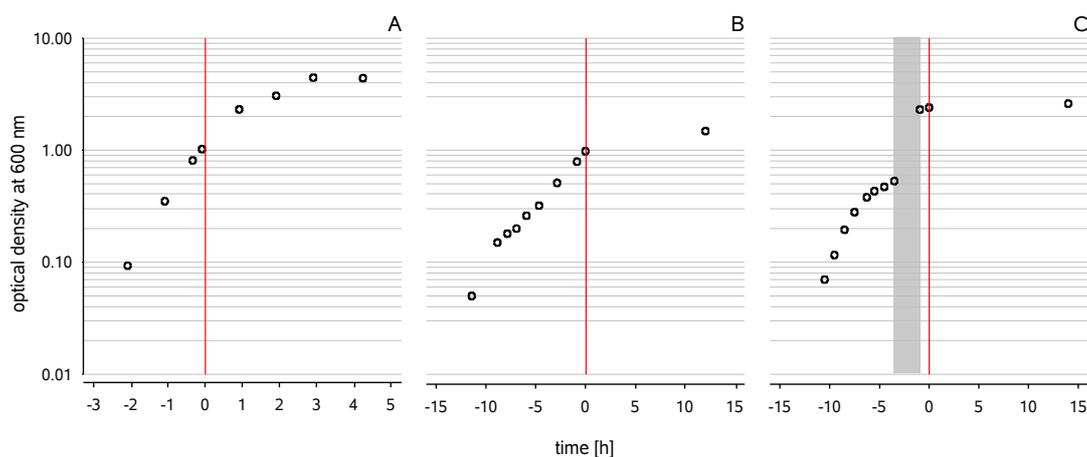


Figure 4-2: Growth of *E. coli* M15 and DL39 HVDAC1 overproduction cultures in different media.

Cell growth was monitored by the measurement of the optical density at 600 nm. Points of IPTG addition are marked by a red line. **A)** *E. coli* M15 in TB media. **B)** *E. coli* M15 in $[^2\text{H}, ^{15}\text{N}, ^{13}\text{C}]$ -M9 media. **C)** *E. coli* DL39 in ^2H -AES media. The grey bar indicates the time period while the cells were centrifuged, washed and resuspended in a fourfold reduced volume of the primary ^2H -AES culture.

The production of HVDAC1 for all other biochemical and crystallisation experiments was carried out in TB medium. In this medium the expression cultures grew normal and led to the formation of 5 g wet cell mass per litre of medium.

Production of selenomethionine labelled protein led to the formation of about 2.5 g wet cell mass per litre of medium.

4.2.2 Isolation of HVDAC1 inclusion bodies

The heterologous overproduction of HVDAC1 in *E. coli* results in analogy to previous studies^{[54][53]}, in the formation of inclusion bodies. Due to the HVDAC1 inclusion body formation it was possible to enrich HVDAC1 in substantial amounts by a single low spin centrifugation step after cell disruption (Fig. 4-3A). Although the vast majority of protein impurities could be removed by this step an additional detergent based step was applied to remove potentially attached membrane parts and hydrophobic proteins. This method led to the extraction of about 70 mg dissolved inclusion bodies from one gram of the in TB grown cells. In all other media this recovery was significantly lower but amounts up to about 25 mg inclusion bodies per gram wet cells were still present.

SDS-PAGE revealed a inclusion body composition of approximately 50% HVDAC1 and several other protein impurities (Fig. 4-3B). To exclude an inhomogeneous expression of HVDAC1, the nature of this impurities was elucidated by the MALDI-MS fingerprint method.

As a result it turned out that in fact only a negligible part of the impurities derived from oligomeric or processed variants of the HVDAC1. The bulk of the examined impurities belong to several other predominantly soluble proteins, often observed in inclusion body fractions.

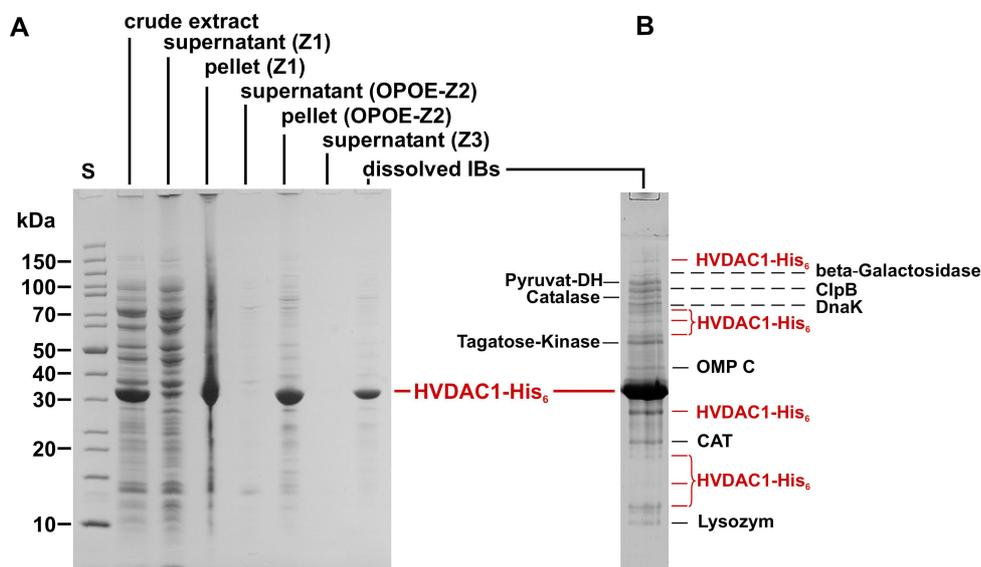


Figure 4-3: HVDAC1 inclusion body (IB) purification

A) HVDAC1 IBs were isolated by three centrifugation steps (Z1-3) in addition to an intermediate incubation in the detergent OPOE (between Z1 and Z2). Aliquots of each step were collected and according to their total sample volume normalised by dilution. 100 μ l of each aliquot were precipitated using acetone and redissolved in the same amount of loading buffer. 5 μ l of each fraction were applied to the depicted 12% SDS gradient gel. **B)** Remaining impurities of the dissolved IB fraction were partially identified by the MALDI-MS fingerprint method.

Among them are prominent chaperones (ClpB, DnaK), several metabolic enzymes (pyruvate dehydrogenase, β -galactosidase, tagatose kinase, catalase, chloramphenicol acetyltransferase), the outer membrane protein OmpC as well as lysozyme which was added for cell disruptive reasons.

Since these impurities were also not removable under alternative conditions of higher ionic strength or with harsher detergents like Triton X-100 or NP-40 the obtained HVDAC1 fraction was intended for further purification after refolding.

4.2.3 Refolding of denatured HVDAC1

Refolding of the denatured HVDAC1 protein was induced by rapid dilution of the inclusion body fraction in LDAO supplemented solution. Successful refolding was initially evaluated on the following assumption. If refolding occurs subsequent to guanidinium chloride depletion, HVDAC1 should remain detergent protected in solution.

If refolding fails the protein should precipitate again and cause a significant clouding of the refolding buffer. Based on the OD_{280} of the refolding buffer an efficient refolding of HVDAC1 with LDAO concentrations above 43.5 mM ($CMC_{LDAO \text{ in } 0.1 \text{ M NaCl}} = 0.14 \text{ mM}$)^[112] was achievable. As revealed by the OD_{280} and SDS-PAGE the clarified refolding solution approximately contained 90% of the in total applied protein, thereby including substantial amounts of evidently refolded HVDAC1 but also almost all other protein impurities (Fig. 4-4B).

4.2.4 Purification of refolded HVDAC1 by Ni^{2+} -affinity chromatography

Due to the remaining impurities, HVDAC1 was further purified by Ni^{2+} -affinity chromatography (Fig. 4-4A). For samples which were intended for crystallisation trials this step was additionally used to exchange LDAO against the dialysable detergent OPOE.

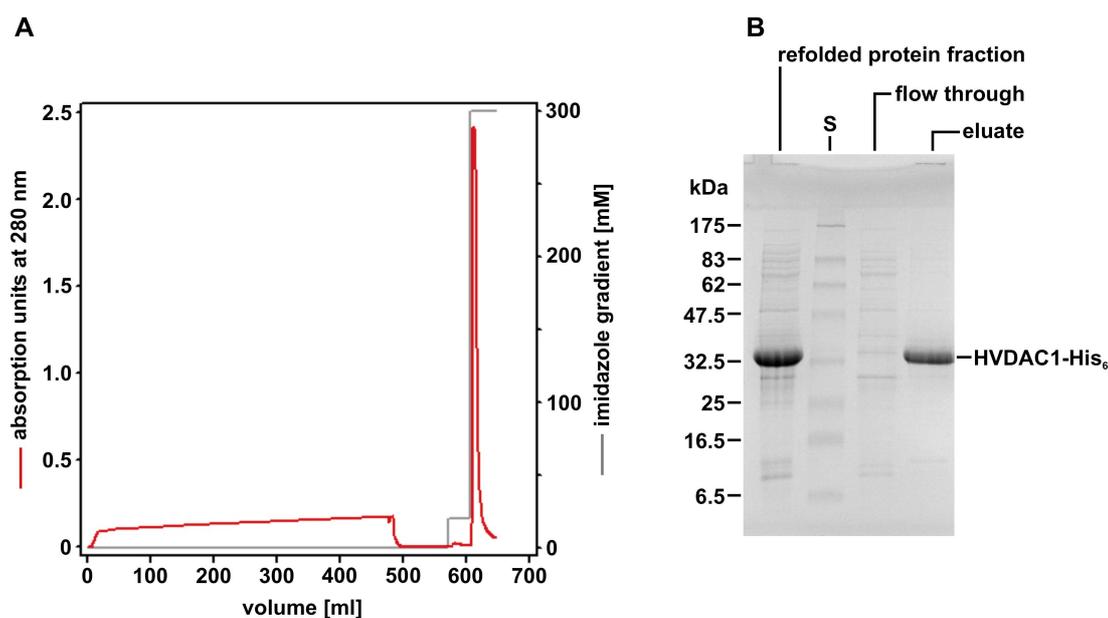


Figure 4-4: Purification of refolded HVDAC1 by Ni^{2+} -affinity chromatography.

HVDAC1 refolding was achieved by a 10-fold dilution of the dissolved IBs fraction (15 mg/ml) in 1% LDAO. Incidental precipitate was pelleted and the remaining solution was again 10-fold diluted in order to reduce the LDAO induced binding interference. **A)** Chromatogram of the HVDAC1- His_6 purification. About 480 ml of the diluted refolding solution were applied to a 5 ml Ni^{2+} Sepharose HP™ column. To exchange the detergent the column was washed with 10 column volumes (CV) of an 0.8% OPOE containing buffer and additional 10 CV of an 0.8% OPOE and 20 mM imidazole containing buffer. HVDAC1- His_6 was subsequently eluted with 10 CV of an 0.8% OPOE and 300 mM imidazole containing buffer. **B)** Purification efficiency as verified by SDS-PAGE. 5 μ l of the refolded protein fraction, the flow through and the eluted HVDAC1- His_6 fraction were each applied.

Since the high amount of LDAO in the refolding solution impairs with an efficient binding of HVDAC-His₆ to the nickel matrix, the solution had to be diluted to an LDAO concentration of 0.2%. After LDAO depletion the solution remained fully transparent. Consequently, the integrity of HVDAC1-His₆ was not affected by the detergent reduction after refolding.

To achieve a maximum purification efficiency, the applied Ni²⁺-sepharose matrix was 1.3 fold overloaded with respect to its theoretical binding capacity of 20 mg/ml. This approach allowed a one step elution of HVDAC1 and finally led to a pure and concentrated HVDAC1 fraction as probed by SDS-PAGE (Fig. 4-4B). After refolding and purification typical yields range from 4 mg HVDAC1 per gram in M9 or AES media grown cells to 15 mg HVDAC1 per gram in TB medium grown cells.

4.3 Characterisation of refolded HVDAC1

4.3.1 Mass determination of HVDAC1

HPLC/ESI-MS analysis of the isolated protein results in a single peak at a molecular mass of 32.140 kDa. This value is virtually equivalent to the 32139 kDa calculated from sequence (cf. chap. 4.1).

The isolated HVDAC1 protein matches therefore exactly the sequence intended to be expressed (Fig.4-1) and was consequently neither modified nor processed during expression and purification.

HPLC/ESI-MS was also used to verify the successful incorporation of selenomethionine in samples intended to solve the crystallographic phase problem. This measurement results in a single molecular mass peak of 32.280 kDa. The difference of 140 kDa is hence indicative for the complete replacement of the three methionine residues by selenomethionine.

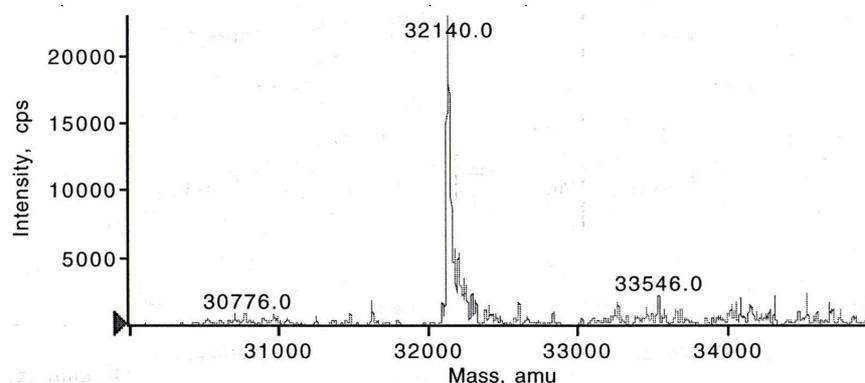


Figure 4-5: Mass analysis of purified HVDAC1 by HPLC/ESI-MS.

Mass spectra of the purified HVDAC fraction. Investigated samples were applied in a concentration of 1 mg/ml. cps: counts per second; amu: atomic mass units.

4.3.2 Evaluation of refolded HVDAC1 by circular dichroism (CD) spectroscopy

Since α -helices, β -sheets and β -turns absorb right- and left-circularly polarized light differentially, their distinct spectral characteristics can be used to predict the secondary structural constitution of proteins and polypeptides.

Thus, CD spectroscopy was used to evaluate the structural constitution of HVDAC1. The molecular ellipticity of the recorded HVDAC1 far-UV spectrum exhibits a minimum of $-10,3 \cdot 10^{-3} \text{ deg cm}^2 \text{ dmol}^{-1}$ at 215 nm and a conversion from negative to positive ellipticity at 204.5 nm (Fig.4-6).

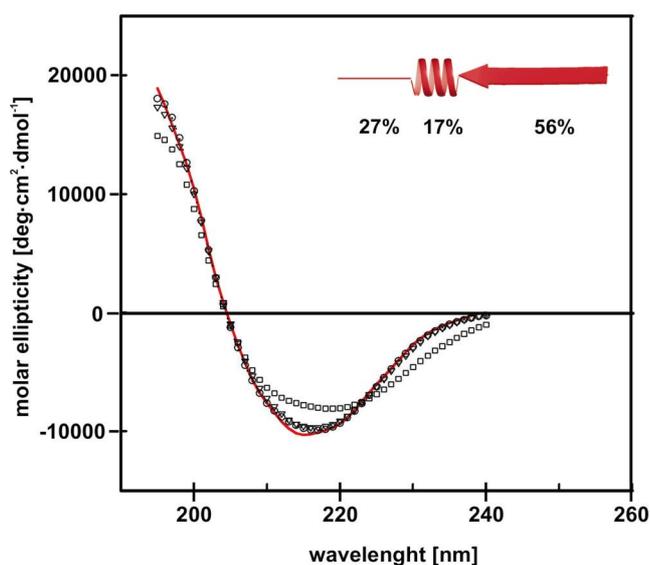


Figure 4-6: Circular dichroism spectroscopy of refolded HVDAC1.

HVDAC1 secondary structural content as proposed by spectrum deconvolution with the CDpro program suite. Superposition of the HVDAC1 spectrum (—) and the recalculated spectra of the CDSSTR, ∇ ; CONTILL, \circ ; SELCON3, \square ; solution.

These values are in addition to the entire curve progression strongly indicative for a high β -sheet content of the refolded protein. Further specified by spectral deconvolution the protein displays approximately 56% β -sheet and β -turn and 17% α -helical structure (Tab.4-1; Fig. 4-6B).

Table 4-1: Predicted secondary structural contents of the HVDAC1 protein in 0.2% LDAO

Deconvolution program	α -helical [%]	β -structure (sheet/-turn) [%]	unstructured [%]
CDSSTR	17.6	55.5 (36.2/19.3)	26.1
CONTINLL	16.1	57.5 (38.2/19.3)	26.5
Selcon3	18.2	55.2 (33.6/21.6)	29.1

4.3.3 Voltage dependent conductance of HVDAC1

Voltage dependency is a common feature of all VDAC proteins. To prove the functional state of the refolded protein, the conductance of HVDAC1 was determined to that effect.

HVDAC1 conductance was recorded at voltages in the range of -100 to 100 mV upon insertion of the protein into a membrane bilayer. Current measurements of single channels demonstrated the ability of HVDAC1 to switch between an open and a closed sub-conductance state of approximately 4.3 and 1.8 nS, respectively (Fig. 4-7). At voltages above ± 50 mV, the channel revealed an additional subconductance state of approximately 2.6 nS.

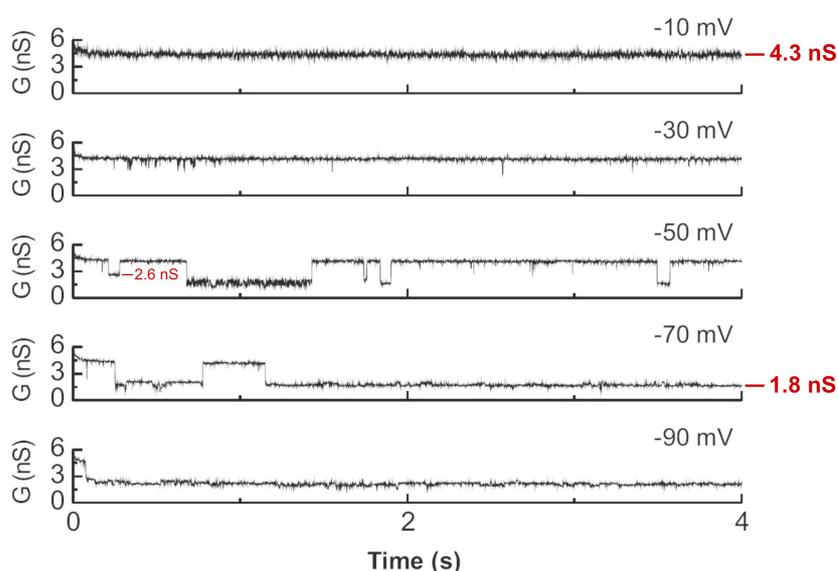


Figure 4-7: Sample current traces of single-channel recordings.

The lipid bilayer experiments were performed by adding the sample to one side of a membrane (cis side) formed by diphytanoyl-phosphatidylcholine/n-decane. Upon insertion, single-channel current traces were recorded after voltage jumps from 0 mV to the indicated voltage.

Consequently, common voltage dependency could also be observed for refolded HVDAC1 when reconstituted in a membrane bilayer.

Moreover, the steady-state conductance of HVDAC was obtained from experiments in which a few channels were reconstituted into the membrane. At membrane potentials up to voltages of ± 30 mV, the closing events in the channel recordings represented only a minor fraction of the current fluctuations. At higher voltages, the number of closing events increased, thereby reducing the steady-state membrane currents (Fig. 4.8A). The recorded data were fitted by a double Boltzmann distribution (3) and followed a bell-shaped curve as a function of the applied voltage (Fig. 4.8B).

$$G_{norm} = \left(\frac{1 - G_{rest(n)}}{1 + \exp^{-A_{(n)}(V - V_{0(n)}})} + G_{rest(n)} \right) \cdot \left(\frac{1 - G_{rest(p)}}{1 + \exp^{-A_{(p)}(V - V_{0(p)}})} + G_{rest(p)} \right) \quad (3)$$

G_{norm} by the mean conductance at ± 10 mV normalised conductance

V : applied potential

$U_{0(p/n)}$: respective negative (n) and positive (p) midpoint potential.

$A_{(p/n)}$: Voltage sensitivity of the channel as determined at the negative (n) and positive (p) midpoint potential.

$G_{rest(p/n)}$: respective rest conductivity at very high negative (n) and positive (p) potentials

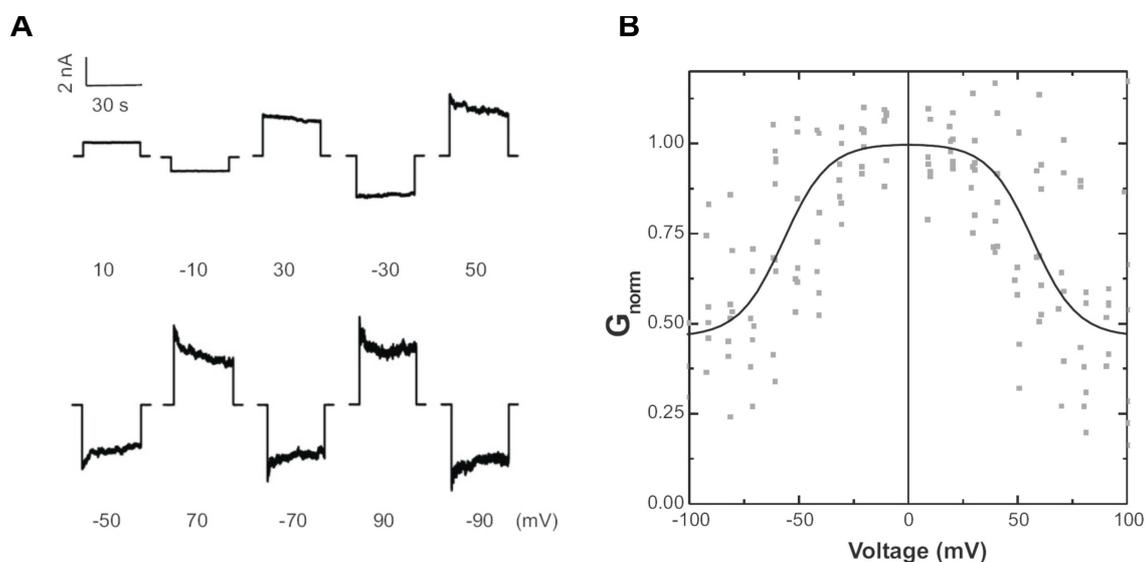


Figure 4-8: Sample current traces of multiple channels.

A) Current traces of multiple channels recorded after voltage jumps from 0 mV to the indicated voltage.

B) Channel conductance G , as a function of the transmembrane potential. The conductance at a given voltage was normalised to G_{norm} by the mean conductance determined at 10 and -10 mV. The solid curves (—) indicate the best fit by a double Boltzmann distribution. The midpoint potential of the distribution was estimated at ± 57 mV.

Estimated by the Boltzmann distribution 50% of the inserted channels adopted a closed sub-state of 43% rest conductivity at a midpoint potential of about 57 ± 8 mV (Tab. 4-3).

Table 4-3 Variables of the fitted Boltzmann distribution

applied potential	negative	potential
midpoint potential, V_0 [mV]	-57.96	55.48
voltage sensitivity, A [mV^{-1}]	0.085	-0.080
G_{rest}	0.39	0.47

Furthermore, the determined voltage sensitivity A suggested in accordance to (4) that at least a number of 2 charges z is involved in the gating process.

$$z \cdot d = A \cdot \frac{kT}{e} \quad (4)$$

k : Boltzmann constant
 e : Electron charge
 T : Absolute temperature = 293K
 A : Voltage sensitivity
 z : number of gating charges
 d : whole membran = 1

4.4 Structure determination of HVDAC1

According to the results obtained by CD spectroscopy and conductance measurements it is assumed that the topology of refolded HVDAC1 is equivalent to the native mitochondrial protein. Thus, HVDAC1 was used in order to determine a high resolution structure of the human VDAC1 by NMR and X-ray crystallography.

4.4.1 Structure determination of HVDAC1 by NMR spectroscopy

Since biomolecules studied by NMR are subjected to size limitations, the HVDAC1 samples consequently had to be fully deuterated, labelled and particularly concentrated to a mM range.

An initial ^{15}N -TROSY-HSQC spectrum of a [^2H (75%), ^{15}N]-labelled HVDAC1 sample revealed a promising spectrum of a well folded and obviously mainly β -stranded protein. Applied T1 ρ measurements estimated the size of the protein/detergent complex in a range of 80 to 120 kDa.

However, the signal intensity of these samples was due to the protein concentration insufficient for an effective recording of the spectra relevant for structure determination.

4.4.1.1 Optimization of HVDAC1 NMR samples

The maximum HVDAC1 concentration in the initial samples was limited to about 0.3 mM. Further increase affected the solubility of the protein and led to significant precipitation as assumed due to significant clouding of the protein solution. Thus, optimisations towards a higher sample concentration were necessary.

Changing the buffer system from phosphate to Bis-Tris and an optimization of the LDAO concentration to 6% allowed an increase of the protein concentration to 0.6 mM. As a result of this improvement a fourfold increase of the signal intensity was observed in the HVDAC1 spectra (Fig. 4-9).

Although the protein solution remained almost transparent up to concentrations of about 1.2 mM these maximization failed in a further enhancement of the signal intensity. Besides the protein concentration the signal intensity was also critically influenced by the applied amount of detergent. Higher as well as lower concentrations than the finally applied 6% failed to improve the signal intensity and moreover, diminished the quality of the recorded spectra.

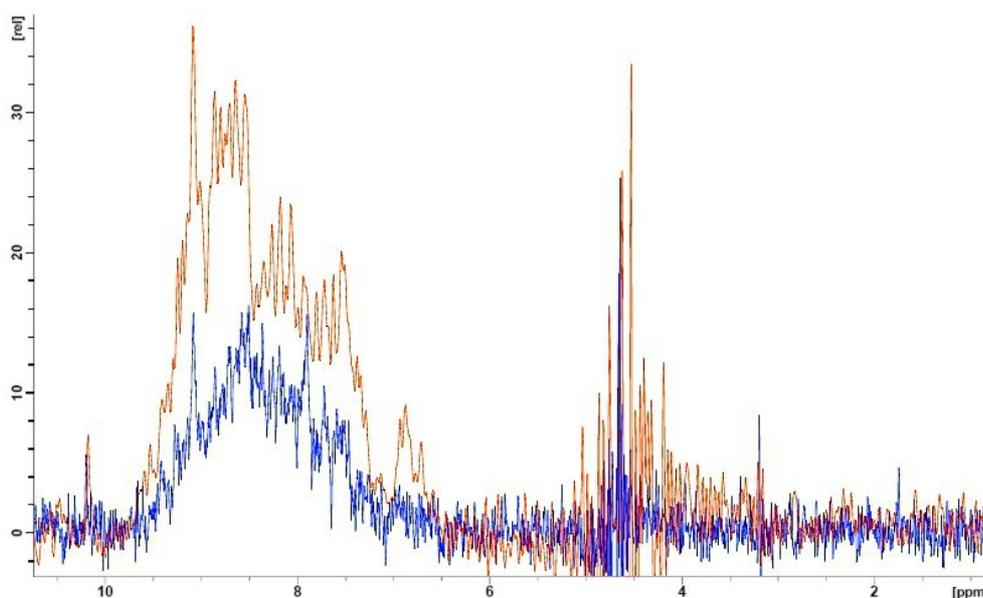


Figure 4-9: Influence of different buffer systems on the NMR signal intensity of HVDAC-His₆.

Superposition of the recorded 1D TROSY-HSQC spectra of HVDAC-His₆. Changing the buffer system allowed an increase of the protein concentration to 0.6 mM and results in a four-fold enhanced signal intensity. The spectra were recorded at 310 K on a 900 MHz spectrometer equipped with a cryogenic probe head. 0.3 mM HVDAC1 in 20 mM KP_i, 0.6% LDAO, pH 6.5 (—); 0.6 mM HVDAC1 in 25 mM BisTris-HCl, 6% LDAO, pH 6.8 (—).

Further optimizations concerned the pH of the buffer system as well as the maximum temperature applied during the measurement. As a result of the recorded 1D TROSY-HSQC spectra it turned out that concentration and quality of the soluble protein remained constant to an acidification down to pH 6.8 and starts to decrease clearly below pH 6.5. Regarding the temperature, the spectral optimum was established at 310 K due to the detection of significant protein unfolding at more elevated temperatures, e.g. 315 K. The most feasible spectral quality was therefore achieved with samples of 0.6 mM HVDAC-His₆ in 25 mM BisTris-HCl pH 6.8 supplemented with 6% LDAO and measured at 310 K.

Optimised samples exhibited a comparable but improved ¹⁵N-TROSY-HSQC spectra with a strong chemical shift dispersion, indicative for a folded and mainly of β -strands composed protein (Fig 4-10). From the 294 expected signals 247 (84%) could be detected. This corresponds to 84% of all possible signals.

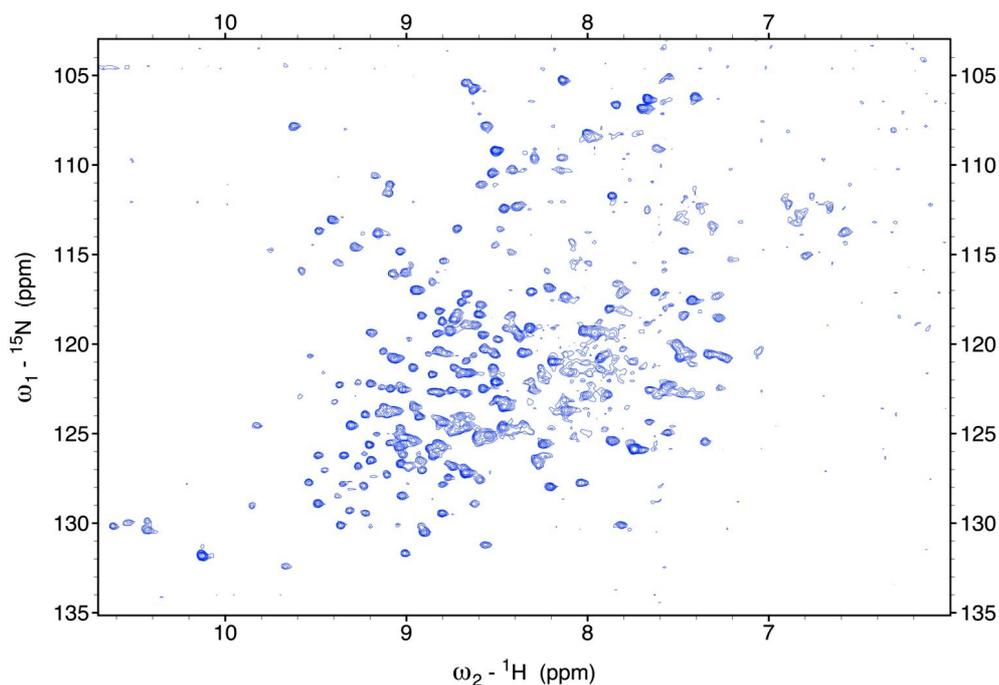


Figure 4-10: ^{15}N TROSY-HSQC HVDAC-His₆ spectrum.

^{15}N TROSY-HSQC spectrum of HVDAC1 in 25 mM BisTris-HCl, 6% LDAO, pH 6.8.

4.4.1.2 Resonance assignment and secondary structure determination

Unfortunately, a signal assignment using the common (^1H , ^{15}N , ^{13}C) standard strategy^[113] becomes largely unfeasible due to strong relaxation observed in most of the 3D triple resonance experiments. Due to the strong relaxation, all experiments implying a coherence transfer to C_β failed. Thus, sequential information was only available from C_α chemical shifts.

Restricted to an HNCA, its modified version and a multiple quantum TROSY-HNCACO at least 70% of the determinable $\text{C}_{\alpha(i-1)}$ peaks could be detected.

However, C_α atoms in general exhibit a low chemical shift dispersion. Consequently, the C_α chemical shifts of most amino acids appear in a very similar range and subsequently complicate an unambiguous amino acid assignment (Fig. 4-11).

To exclude wrong connectivities HVDAC1 had to be prepared in various modified versions. Therefore several ^{15}N and $^{15}\text{N}/^{13}\text{C}$ labelled amino acids were selectively incorporated into HVDAC1. Signals observed from such samples arose almost exclusively from the incorporated label and therefore allowed the assignment of the incorporated amino acid type.

By this approach it was possible to assign the amino acids alanine, arginine, isoleucine, leucine, lysine, methionine, phenylalanine, tyrosine and valine to their corresponding HSQC shifts (Fig. 4-12). However, this method is only sensitive to the incorporated amino acid type and inappropriate to assign individual residues.

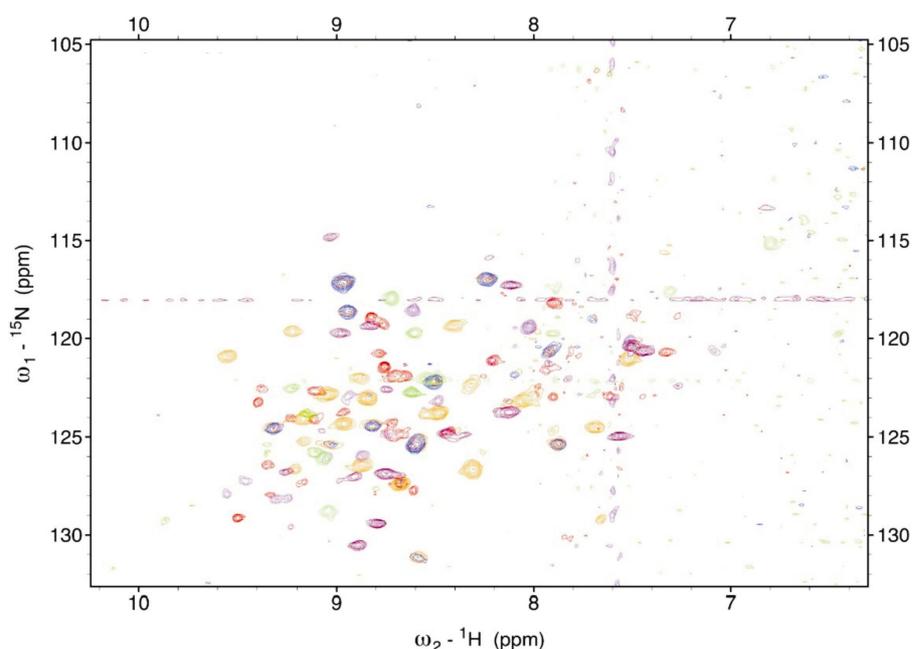


Figure 4-12: Overlay of ^{15}N TROSY-HSQC spectra of selectively labelled HVDAC-His₆.

Chemical shifts are correlated to the assigned amino acid type. Red: Ile, Leu, Met; Orange: Ala, Val; Blue: Val; Green: Tyr; Magenta: Lys; Light green: Arg; Violet: Phe.

Thus, further structural information had to be extracted from chemical shift perturbations of HVDAC1 single cysteine mutants. Restricted to the locally induced alteration of the electronic environment, only shifts of residues in the local vicinity of the mutation site were affected and became sequentially assignable (Fig. 4-13). Furthermore, the detected perturbations of some mutants reappear periodically around the mutated amino acids and are indicative for anti-parallel β -strands in the respective region. In additional experiments, the prepared single cysteine mutants have also been modified with the paramagnetic spin label MTSL. Due to the paramagnetic relaxation enhancement these modifications caused specific peak intensity reductions in an environment of 20-25 Å. Thus, the observed alterations were well suited for the verification of the sequential assignment as well as for the establishment of a HVDAC1 topology model.

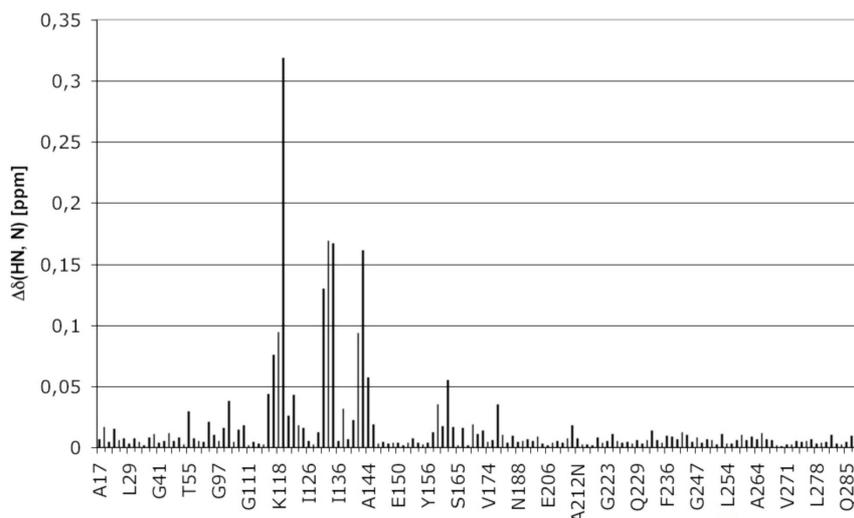


Figure 4-13: HN and N chemical shift changes upon residue mutation of HVDAC-His.

Chemical shift changes of residues close to the mutation side C130S as plotted against the assigned residues. The appeared clustering is indicative for a β -stranded fold around the introduced spin label.

Combined together, the information of all native, selective labelled and mutated samples allowed an extensive sequential assignment of the HVDAC1. In total 56% of all backbone resonances could be assigned by this approach (Fig4-15). Since the HVDAC1 TROSY-HSQC spectrum (Fig. 4-10) exhibited only 84% of the expected chemical shifts, this corresponds to about 67% of the maximum assignable peaks. Interestingly, the vast majority of the assigned residues belong to two thirds of the C-terminal residues. By contrast, in the N-terminal part only a few residues could be assigned so far (Fig 4-14).

Based on the assignment, the secondary structural elements of HVDAC1 were identified by the differences between calculated random coil values and the experimentally observed C_{α} and C' chemical shifts^[114]. Relative to random coil values C_{α} and C' resonances tend to shift upfield in β -strands and down field in α -helical regions. Thus, negative secondary chemical shifts refer to β -stranded and strong positive shifts to α -helical regions when subtracted from the random coil values. The secondary chemical shift pattern thereby obtained exhibits along the assigned sequence of HVDAC1 predominantly negative shifts which are periodically clustered by small positive values (Fig. 4-14). Hence, the refolded HVDAC protein mainly consists of β -strands in the assigned regions. By contrast, strong positive values exclusively appeared at the beginning of the N-terminal region, thereby supporting the existence of the predicted N-terminal α -helix.

Moreover, the secondary structural distribution of HVDAC1 was also probed by the residue specific solvent accessibility in a D_2O exchange experiment.

Since the potential $^2\text{H}/^1\text{H}$ exchange becomes decelerated by the secondary structural hydrogen bonding network a TROSY-HSQC was recorded after an exchanging period of one hour. The recorded spectrum still displayed 37% of the 247 initially observed HSQC resonances. Out of these 91 exchange resistant peaks, 90 have been assigned. Based on the distribution of the assignable residues 87 correspond to residues which reside in the C-terminal two thirds of the protein.

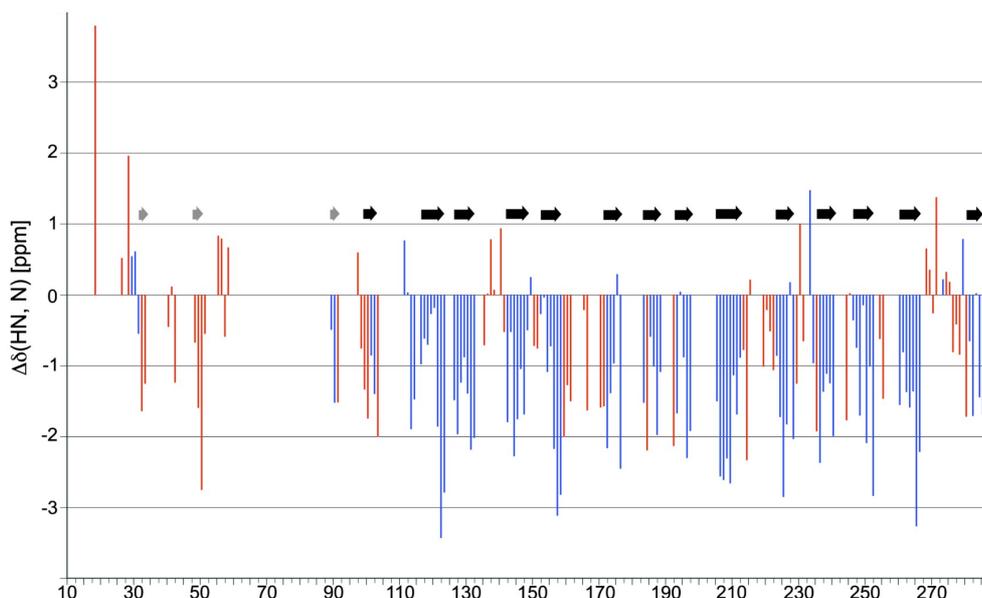


Figure 4-14: Secondary chemical shifts of HVDAC1-His₆.

C_{α} and C' derived secondary chemical shifts are plotted against all sequentially assigned residues of HVDAC1. Negative and strong positive values are indicative for β -strands and α -helices, respectively. Residues which exchange with D_2O after 1 h are coloured in red. Residues which are exchange resistant after 1 h are coloured in blue. Unambiguously assigned β -strands are indicated by black arrows. Potentially β -stranded fragments are indicated by grey arrows.

When correlated to the secondary structural shift distribution the obtained $^2\text{H}/^1\text{H}$ exchange data confirmed the established secondary structural assignment to a large extent. Most of the residues with β -strand indicative negative shifts were also $^2\text{H}/^1\text{H}$ -exchange resistant and are flanked by loops or turns of exchange sensitive residues (Fig.4-14).

As a result, in the C-terminal two thirds of the protein 14 β -strands could be unambiguously assigned (Fig. 4-14) (Tab. 4-4). In spite of the only fragmentary established assignment in the N-terminal region three further potential β -strands could be identified due to the secondary structural shift distribution (Fig. 4-14) (Tab. 4-4).

Table 4-4 Secondary structural assignment of HVDAC1-His₆

β -sheet	residue-range	sequence	β -sheet	residue-range	sequence
N-1	29-33	LIKLD	N-3	89-91	EVT
N-2	55-58	TKVT			
C-1	97-103	GLKLTFD	C-8	193-197	FGGSI
C-2	116-223	KIKTGYKR	C-9	205-212	ETAVNLA
C-3	126-132	INLGCDM	C-10	223-228	GIAAKY
C-4	142-148	IRGALVLG	C-11	236-240	FSAKV
C-5	152-158	LAGYQM	C-12	246-252	IGLGYT
C-6	172-176	FAVGY	C-13	260-266	LTLSALL
C-7	183-188	LHTNVN	C-14	281-286	GLGLEFQ

However, since most of the residues in the N-terminal third of HVDAC1 were either not assignable or readily exchanged with D₂O a more advanced characterisation became virtually impossible. The reason causing the lack of structural information in this region might be attributed to an enhanced flexibility of the N-terminal part. As such, this argument is further confirmed by the observed heteronuclear NOEs.

In general, heteronuclear ¹⁵N{¹H}-NOEs above 0.7 refer to regions of lower flexibility, values below 0.7 to regions of an enhanced flexibility. All in all, 62% of the recorded heteronuclear ¹⁵N{¹H}-NOEs exhibited a value above 0.7 and hence refer to a largely well ordered protein. However, most of the assigned N-terminal (61%) as well as most of all unassigned residues (65%) exhibit ¹⁵N{¹H}-NOEs below 0.7, thereby indicating an enhanced mobility of these residues (Tab. 5-3). In the comparatively large C-terminal part, by contrast, only one third (33%) of the assigned residues exhibit ¹⁵N{¹H}-NOEs below 0.7. Moreover, out of these 33%, 62% are assigned to residues which reside in loop regions, predominantly in the enlarged one between residue 268 and 278 (Tab. 5-3). Thus, compared to the entire protein, the ratio of the observed ¹⁵N{¹H}-NOE values lead to the conclusion that the N-terminal third of HVDAC1 poses an enhanced flexibility.

Table 5-3: Percentages of ¹⁵N{¹H}-NOEs values below 0.7 against different sequence regions

Residues	¹⁵ N{ ¹ H}-NOEs < 0.7 [%]
N-terminal (1-97)	61
C-terminal (97-288)	33*
unassigned	65

*) 62% of the 33% belong to loop regions

4.4.1.3 NMR topology model of HVDAC1

In order to maximise the NOE information ^{15}N -edited NOESY spectra were measured on samples of a different deuteration grade. Samples with a deuteration grade of about 99% only exhibited HN-HN crosspeaks whereas samples with a deuteration grade of approximately 75% also showed peaks to aromatic and a few $\text{H}\alpha$ protons. The combination of all NOESY-TROSY spectra finally led to the assignment of 39 crosspeaks (Tab 4-5).

Based on the observed HN-HN cross peaks, the secondary structural shifts and the $^1\text{H}/^2\text{H}$ amide proton convertibility, a two dimensional topology model of the 14 C-terminal β -strands could be established (Fig. 4-15). Moreover, the negative secondary chemical shift values of the residues between 29-33 and 55-58 (Fig. 4-14) suggest the existence of at least three further β -strands in the N-terminal part of the HVDAC1.

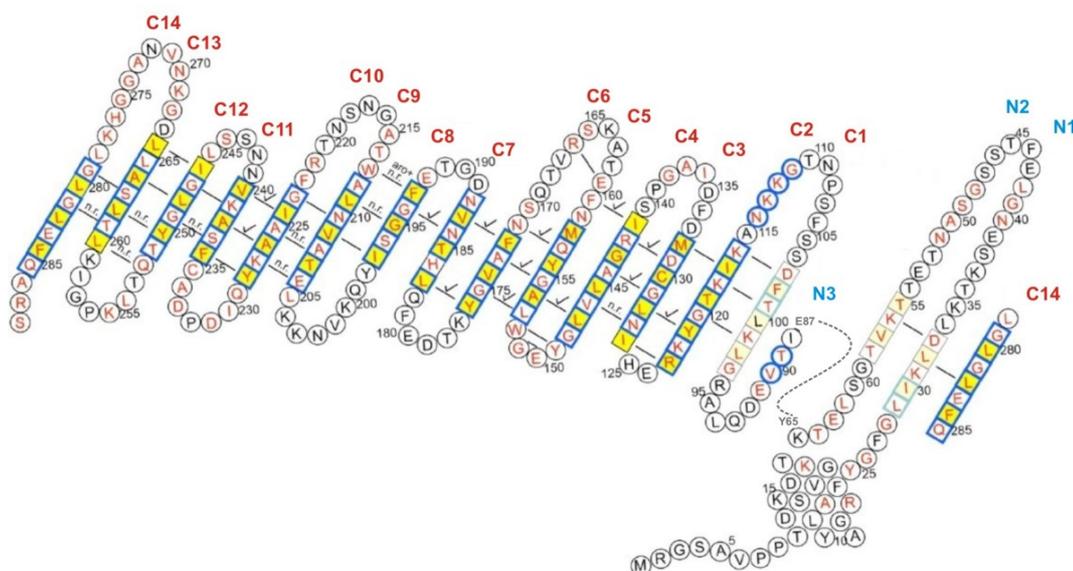


Figure 4-15: NMR topology model of HVDAC1.

Unambiguously established β -strands in the C-terminal part are numbered in red. Three further potential β -strands in the N-terminal part are numbered in blue. The depicted α -helix is based on the observed secondary chemical shifts and the PSIPRED analysis. Amino acids are given in a one letter code. Red letters denote assigned, black letters unassigned residues. The HN-HN connectivities are represented by black lines. Checks on top of these lines refer to NOEs which are also present in 100% D_2O . The abbreviation "n.r." and "aro" are indicative for not resolved NOEs and NOEs of aromatic protons, respectively. Boxed residues are part of a β -strand. Residues which do not exchange with D_2O after 1 h are bordered in blue or light blue. β -strands which are bordered in light blue or gray exhibit an increased flexibility. The side chains of the residues in yellow boxes point towards the hydrophobic membrane, side chains of residues in white boxes face to the hydrophilic channel pore. The dashed line refers to a section of 23 residues for which no structural information is available so far.

However, the NOE connectivities in these regions are poorly resolved and might therefore be misleading. Because of the secondary chemical shift analysis and in accordance to the obtained PSIPRED results (Fig. 4-1), the model proposes besides the present 17 β -strands also an α -helix at the N-terminal end of HVDAC1 (Fig. 4-15).

Table 4-5 HN-HN connectivities assignment of HVDAC1-His₆

Nr.	residues	NOE	Nr.	residues	NOE	Nr.	residues	NOE
1	L31-L282	+	14	Y149-W152	+	27	A208-A225	+*
2	D33-K56	+	15	E150-G151	+	28	N210-G223	+
3	K99-G120	+	16	L153-G175	++	29	I224-V240	++
4	T101-K118	+	17	G155-A173	++	30	A226-A238	++
5	D103-K116	+	18	Q157-N171	++	31	Y228-F236	+
6	I117-M132	+	19	E161-R166	+	32	S237-G249	+*
7	Y121-L128	++	20	F172-V187	++	33	K239-G247	+
8	R123-I126	+	21	Y176-L183	++	34	I246-L266	+
9	N127-V146	+*	22	N186-G194	++	35	L248-A264	+
10	G129-A144	++	23	F193-W213	+* ^{aro}	36	Y250-L262	+*
11	D131-R142	++	24	G195-L211	+*	37	Q252-L260	+*
12	I141-F160	++	25	I197-V209	+	38	T261-G281	+*
13	L147-A154	++	26	E206-K227	+*	39	S263-G279	+

+: interstrand NOE; +*: not resolved interstrand NOE; ++: interstrand NOE, also present in 100% D₂O;

+*^{aro}: inter-strand NOE of aromatic protons

Due to a lack of structural information, a gap of 23 residues between Y65 and E87 did not allow a complete secondary structural assignment of HVDAC1. However, the length and the amphipathic nature of these fragment suggests that the structure of HVDAC1 possesses at least one or two further β -strands than assigned so far.

4.4.1.4 Spatial position of the N-terminal α -helix

Since V20 is supposed to be located in the N-terminal α -helix, its structural position was investigated by the chemical shift perturbations of the mutant V20C/C130S/C235S. The recorded TROSY-HSQC spectrum of this mutant exhibited the most distinct perturbations in the vicinity of the mutation site V20C and a region in the C-terminal part of HVDAC1-His₆, the region around A226 (Fig. 4-16). This finding is also consistent with the paramagnetic relaxation enhancement (PRE) observed from the MTSL spin labelled mutant C130S. In this mutant the label was attached to the remaining cysteine at position 235.

Because of the low signal to noise ratio, only peaks which were broadened beyond detection were considered as an effect. As a result, the largest effects were observed in the region around the labelled site (C235). However, besides the expected region further effects were detectable on the resonances of the N-terminal residues A17 and R18. The spin label attached to C235 hence specifically affected residues in the proposed N-terminal α -helix.

Combined together, the findings derived from the mutants V20C and C135S led to the conclusion that the N-terminal α -helix of HVDAC1 resides closely to the β -stranded barrel region in-between β -strands C9 and and C12 (Fig. 4-15).

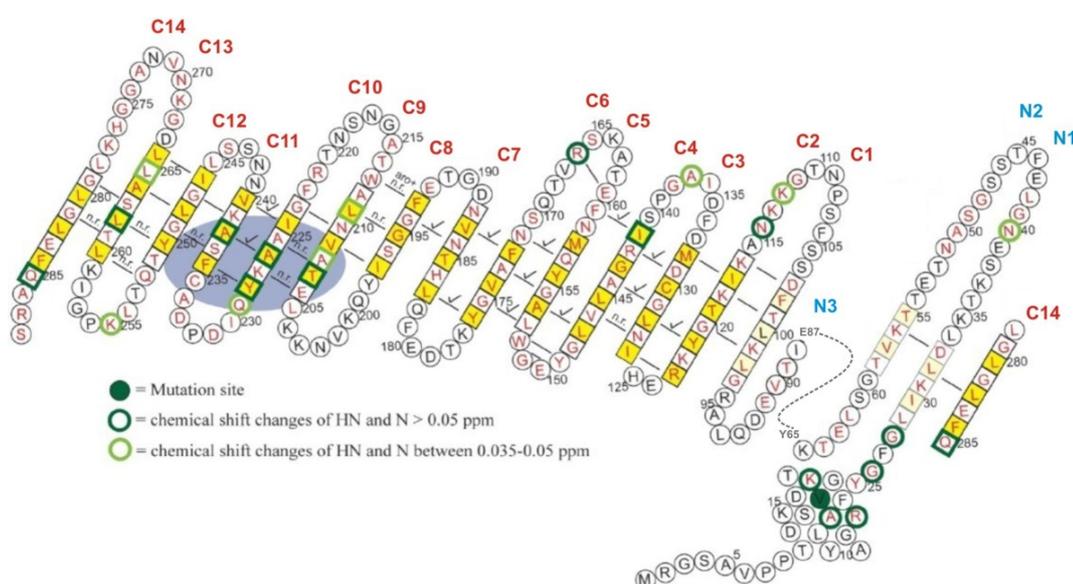


Figure 4-15: Chemical shift perturbations of the HVDAC1 V20C/C130S/C235S mutant.

The observed chemical shift perturbations of the V20C/C130S/C235S mutant are residue specific mapped on the NMR topology model of HVDAC1. The mutation site V20C is denoted by the green background. Residues which exhibited H_N and N shift changes greater than 0.05 ppm are highlighted by a dark green border. Residues which exhibited perturbations in between 0.035 and 0.05 ppm are highlighted by a light green border. The most clustered effects are enclosed by a blue ellipsoid.

4.4.2 Structure determination of HVDAC1 by X-ray crystallography

Refolded HVDAC1 was also used in crystallisation trials with the objective of its structure determination by X-ray diffraction.

4.4.2.1 Crystallisation of HVDAC1

Due to the expression strategy several milligrams of refolded HVDAC1 became available and facilitated an extensive screening for suitable crystallisation conditions.

Since the detergent plays a crucial role in membrane protein crystallisation, LDAO was exchanged against OPOE following refolding. In contrast to LDAO, OPOE can be exchanged by dialysis due to its 10-fold higher critical micellar concentration (6.6 mM). By taking advantage of this property HVDAC1 could be gently transferred into 16 different detergents by dialysis (Tab. 4.6). Moreover, the use of this strategy allowed to maintain a constant protein concentration of 10 mg/ml during the exchange process. Consequent reconcentration which entails a concurrent increase of the detergent concentration could hence be omitted. In the majority of cases, protein concentrations above 10 mg/ml caused significant precipitation during dialysis and were therefore not applicable. Significant HVDAC1 precipitation was also observed with DDM and Cymal-6 if these were applied in a concentration threefold above their CMCs as routinely used for all other detergents. To still maintain a preferably high protein concentration, DDM and Cymal-6 were applied in concentrations 10-fold above their CMCs. HVDAC1 samples were used in crystallisation trials against 347 different precipitants. Potential HVDAC1 crystals appeared over an incubation period of two days to three weeks in 84 of the about 5500 tested conditions.

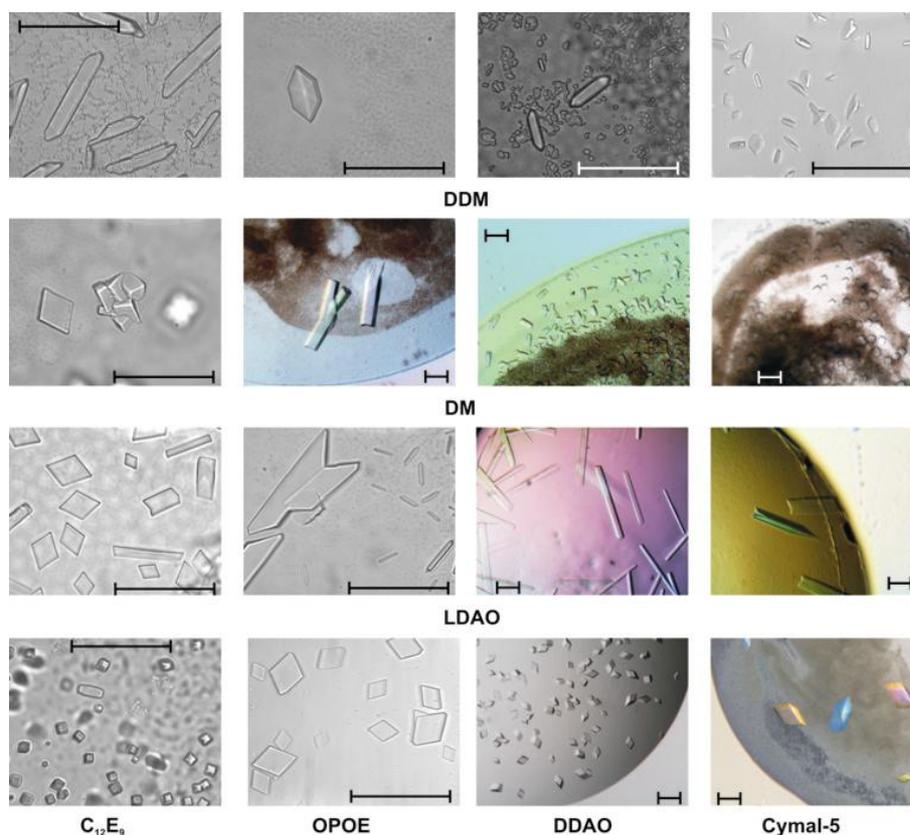


Figure 4-15: Obtained HVDAC1 crystals.

Potential HVDAC1 crystals appeared with several detergents under various conditions. Most of the crystals detergent-independent occurred as thin rhomboid plates or parallelepipeds, but also in a variety of rods and hexagonal pyramids and prisms. Crystals were all achromatic. All colorations are solely due to the application of a polarisation filter. Scale bars: 100 μm.

Regarding the detergents, 8 of the initially applied 16 supported the formation of crystals under several conditions. Within the successful detergents a large number of crystallisation conditions were particularly observed in conjunction with LDAO and DDAO (Tab. 4-6). With few exceptions all crystals grew in the presence of high concentrations of low to medium molecular weight polyethylene glycols (e.g. 20-30% PEG400-4000) at pH values between 6 and 8. None of the successful conditions contained higher salt concentrations.

Most of the crystals exhibit a morphology of thin rhomboid plates or parallelepipeds (Fig 4-15) of a size up to 200 μm in their maximal dimension. Besides the predominant forms several other crystals appeared as rods of different length, shape and thickness and sporadical also as hexagonal pyramids or prisms (Fig 4-15).

Table 4-6 Summary of the HVDAC1 crystallisation trials

Detergent	Conc. [%]	Successful conditions	Maximum resolution [\AA]
C ₈ E ₄	0.67	2	> 30
C ₁₀ E ₈	0.067	-	--
C ₁₂ E ₉	0.067	2	> 30
OPOE	0.33	5	> 8
OG	0.5	-	--
NG	0.17	-	--
NM	0.23	-	--
DM	0.1	8	> 20
UM	0.067	-	--
DDM	0.33	9	> 30
DDAO	0.17	27	> 8
LDAO	0.067	22	> 15
Cymal-3	0.67	-	--
Cymal-4	0.2	-	--
Cymal-5	0.067	9	3.6
Cymal-6	0.20	-	--

Conc., indicates the initial concentration of detergent in the crystallization drop. Successful conditions quotes the number of different crystallisation conditions out of the used 334 under which crystals appear.

Even if most of the obtained crystals were well-formed and exhibited sharp edges the vast majority of them only diffracted to a resolution of about 8 \AA at its best. Diffraction to a maximum resolution of about 3.6 \AA could solely be observed for a set of parallelepiped crystals of almost identical lattice constants. All of these crystals were grown with 0.2% Cymal-5 under the two conditions 30% PEG 400, 0.1 M HEPES/NaOH pH 7.5, 0.2 M MgCl₂ and 30% Jeffamine ED-2001, 0.1 M HEPES/NaOH pH 7.0 (Tab. 4-6).

Other crystals of similar lattice constants, but crystallised in the presence of DDAO, only diffracted to about 8 Å and are hence indicative for the importance of Cymal-5 for the generation of crystals of reasonable quality.

Although the formation of the HVDAC1/Cymal-5 crystals was reproducible the crystal quality varied strongly in diffraction. Most of them diffracted only to about 6 Å and only a minor fraction to higher resolutions. Interestingly, these fluctuations were not only recognizable across but also within the different refolding batches. To exclude that this effect was due to a potential modification of the protein, some of the better diffracting crystals were subsequent to the X-ray experiment redissolved and analysed by N-terminal sequencing and mass spectrometry. The result of these investigations verified on the one hand that the diffracting crystals were unambiguously composed of HVDAC1 and furthermore, that neither the N- nor the C-terminus of the applied protein were processed during crystallisation. The observed fluctuations in diffraction quality might therefore be due to slight but inevitable micro-environmental variations in the different crystallisation drops.

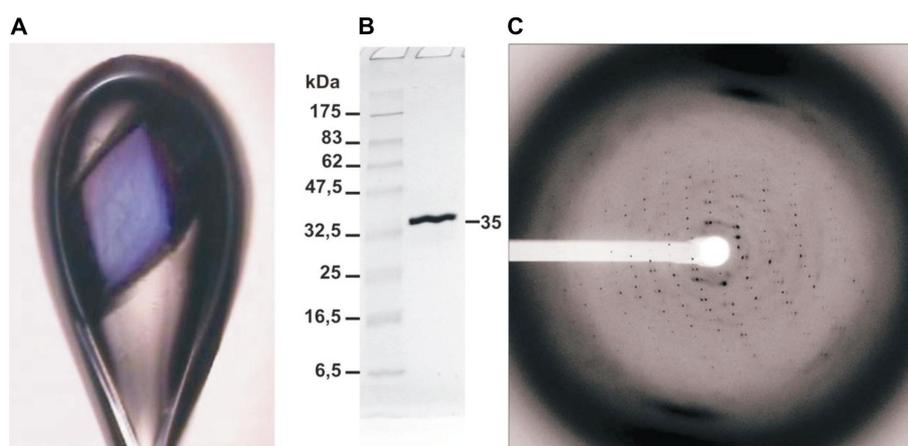


Figure 4-15: Diffraction pattern of HVDAC1-His₆/Cymal-5 crystals.

Crystals of HVDAC1/Cymal-5 diffracted to a maximum resolution of about 3.6 Å. **A:** Parallelepiped HVDAC1/Cymal-5 crystal mounted in a 0.2-0.3 mm cryoloop. **B:** Coomassie stained SDS gel of redissolved HVDAC1/Cymal-5 crystals. The 35 kDa band was verified as HVDAC1 by both N-terminal sequencing and a MALDI-MS fingerprint analysis. **C:** Diffraction pattern of the in A depicted crystal as collected at the beamline PXII of the swiss light source. The detector edges correspond to a resolution of 3.5 Å.

4.4.2.2 Structure determination of HVDAC1

The HVDAC1 crystals belong to a trigonal space group with unit cell dimensions of $a = b = 78.9$ Å and $c = 165.7$ Å (Tab. 4-7). Systematic absences along the crystallographic c axis suggest the nature of the threefold axis as either 3_1 or 3_2 . Thus, HVDAC1 crystallised in one of the enantiomorphous space groups $P3_x$, $P3_x12$ or $P3_x21$.

Due to the lack of VDAC high resolution structures the mandatory phase information had to be determined experimentally. Since this approach required an isomorphous derivative or modifications within the native protein HVDAC1 crystals were either soaked by Pt containing compounds or crystallised from a selenomethionine-derivatised HVDAC1 version.

The best selenomethionine and dichloro(ethylenediamine)-platinum derivatives thereby obtained, diffracted to a resolution of about 4.0 Å and 4.3 Å, respectively (Tab.4-7). For experimental phasing, multiple wavelength anomalous dispersion (MAD) datasets of SeMet- and single wavelength anomalous dispersion (SAD) datasets of Pt-derivatized crystals were collected and allowed the heavy atom substructure determination of two selenium and two platinum sites. Moreover, taking advantage of the isomorphism of the two datasets, they could simultaneously be used for the refinement of the four sites and subsequent phase probability calculations.

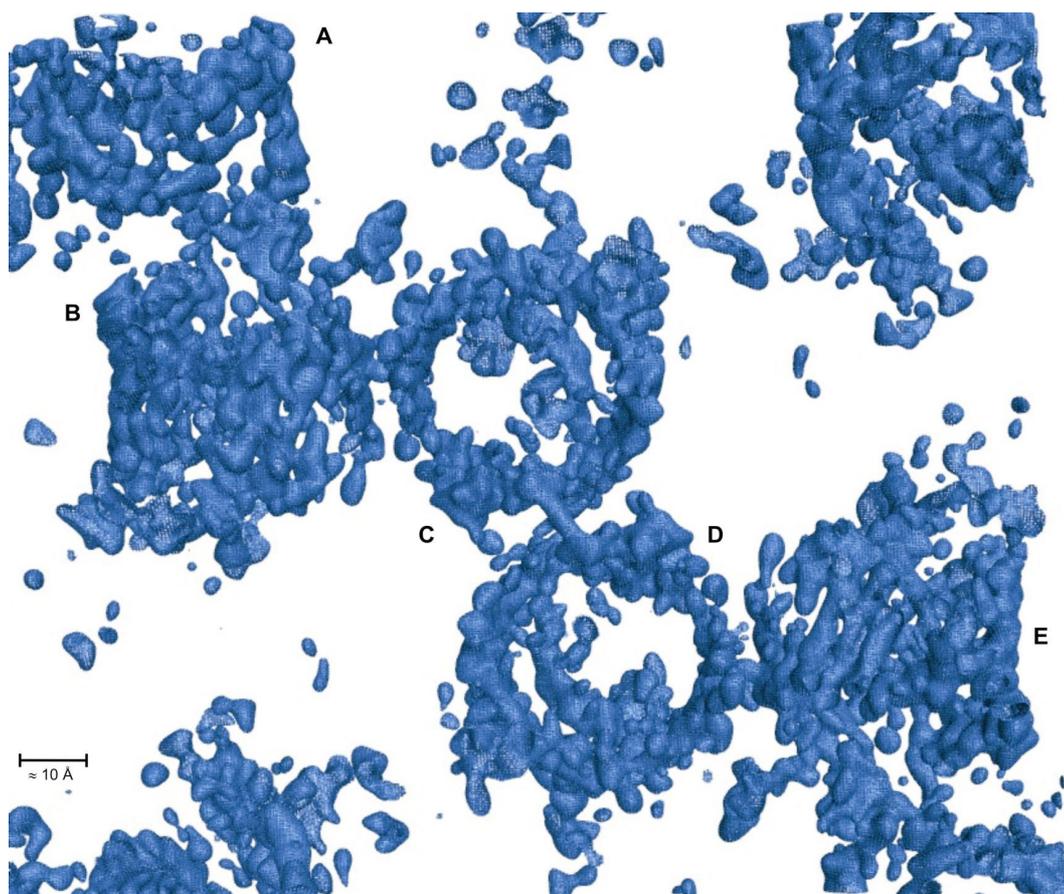


Figure 4-16: Electron density map of HVDAC1-His₆ subsequent to density modification.

Illustrated section of the electron density map after solvent flattening (σ level = 1.5). Several barrel shaped structures of about 50 Å in width and height are visible from the top (C,D) and a lateral (A,B,E) point of view.

Table 4-7 Data collection and phasing statistics for native and derivatised HVDAC1-His₆ crystals.

Crystal	TM10		TM7 _(SeMet)		TMZ6 _(Pt)
Space group			P 3 ₂ 2 1		
Cell dimensions					
a, b, c, [Å]	78.9, 78.9, 165.7		77.6, 77.6, 166.5		76.7, 76.7, 164.5
α, β, γ, [°]	90, 90, 120		90, 90, 120		90, 90, 120
Data collection	Native	Peak	Edge	Remote	Peak
Resolution [§] [Å]	20.00-3.6 (3.81-3.60)	25.00-4.00 (4.22-4.00)	25.00-4.00 (4.22-4.01)	25.00-4.07 (4.29-4.07)	38.39-4.25 (4.48-4.25)
Wavelength [Å]	0.954	0.9795	0.9797	0.9756	1.072
Measured reflections [§]	51117 (8029)	26987 (3845)	26461 (3453)	25150 (3278)	35359 (2383)
Redundancy [§]	7.1 (7.3)	5.2 (5.3)	5.1 (5.1)	5.0 (4.7)	8.3 (4.0)
Unique reflections [§]	7223 (1105)	5293 (725)	5172 (681)	4983 (699)	4283 (595)
Completeness [§] [%]	98.3 (99.9)	99.4 (98.7)	98.7 (93.7)	99.3 (98.6)	99.8 (99.8)
R _{merge} ^{†§} [%]	10.8 (66.1)	8.5 (57.2)	8.2 (59.9)	7.9 (57.9)	14.1 (54.2)
Mean I/σ(I) [§]	11.08 (3.02)	13.2 (2.3)	13.3 (2.2)	13.3 (2.2)	12.9 (2.2)
Solvent content [%]	73.5		72.7		71.8
Phasing statistics					
Number of sites			2 Se		2 Pt
Phasing power [#] -					
overall	-/-	-/0.77	0.47/0.39	0.47/0.39	0.58/0.33
shell 12.09-8.77 Å		-/4.51	3.31/2.30	0.60/2.27	0.81/1.69
shell 8.77-7.22 Å		-/1.93	1.44/1.09	0.61/1.05	0.75/0.83
shell 7.22-6.28 Å		-/1.20	0.82/0.62	0.41/1.05	0.72/0.44
shell 6.28-5.63 Å		-/0.87	0.52/0.41	0.30/0.41	0.64/0.28
Figure of Merit [%] -					
overall	-/-		0.27		
shell 12.09-8.77 Å			0.79		
shell 8.77-7.22 Å			0.63		
shell 7.22-6.28 Å			0.44		
shell 6.28-5.63 Å			0.33		

[†]), $R_{\text{merge}} = \sum_{\text{unique reflections}} (\sum_{i=1}^N |I_i - \bar{I}|) / \sum_{\text{unique reflections}} (\sum_{i=1}^N I_i)$;

[§]) Values for the highest resolution shell are given in parentheses

[#]) Phasing power = [| Fh(calc) | / phase-integrated lack of closure] for (acentric / anomalous) reflections;

[%]) Figure of Merit for acentric reflections.

With phasing power up to approximately 6 Å the most probable solution was found for space group $P3_221$ with a mean figure of merit (FOM) of 0.27 across the entire resolution range (38.39 - 4.0 Å). According to this solution the crystals contain one HVDAC1 molecule per asymmetric unit.

Phase improvement was carried out by density modification through a stepwise increase of the solvent content, solvent flipping and density truncation. Finally, this approach enabled a phase extension to approximately 4.5 Å as estimated from the resulting electron density map which unambiguously exhibit barrel shaped structures.

4.4.2.3 Overall dimensions of the barrel shaped structures

These barrel shaped structures can be described by hollow and slightly elliptical cylinders with outer dimensions of about 41 and 42 Å in diameter and approximately 33 Å in height (Fig. 4-17) However, the estimated height only reflects the lower limit of the core barrel and might be underestimated by 5 to 10 Å. This is due to several ambiguous and disconnected density stretches which remained unaccounted for when determining the barrel height (for illustrative reasons not shown in Fig. 4-17).

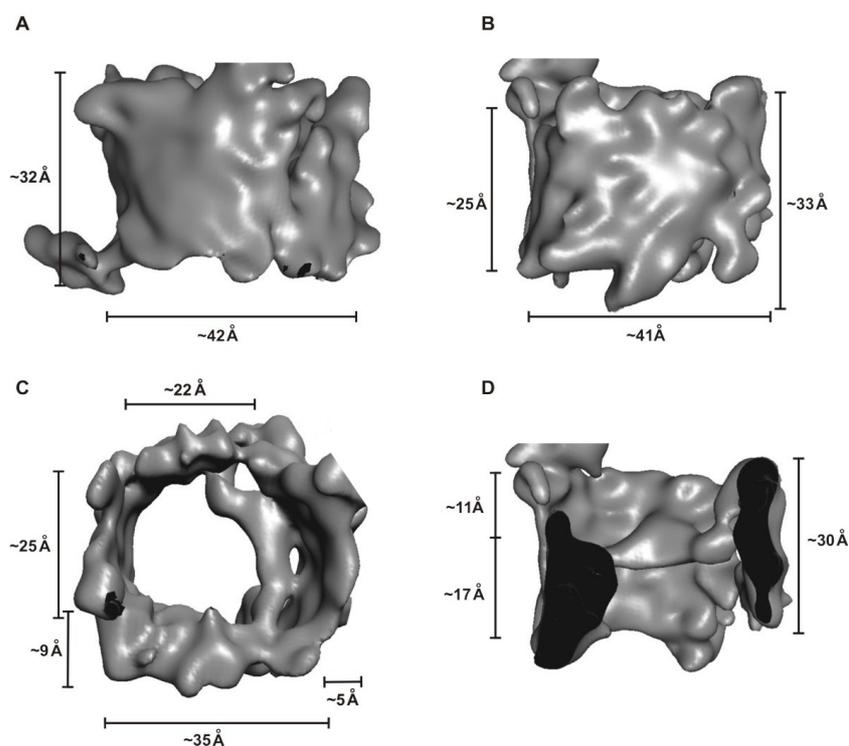


Figure 4-17: Overall dimensions of the HVDAC1 structure

Surface representations of the barrel shaped structures. The surface of the derived electron density was generated by the isosurface function of PYMOL (applied σ level = 1.0). Distances were determined by dummy atoms placed at the density borders in PYMOL (not illustrated). (A, B) Lateral views of the HVDAC1 density surface, before and after 90° rotation. (C) Top view. (D) Lateral view of a mid section.

Both barrel edges exhibit several indentations along the cylinder flanges. Due to these indentations the core barrel height varies in a range between 25 and 33 Å. The barrel wall is formed by a thin envelope of changing thickness and varies between about 5 Å and a maximum of approximately 9 Å (Fig. 4-1C). At the level of both channel entrances this wall encloses an elliptical pore lumen of about 35 Å × 25 Å in diameters. In a depth of about 11 Å the pore diameter becomes further constricted by a density stretch which extends almost horizontally along a third of the barrel wall (Fig. 4-17D). This density stretch seems to be an additional feature well clear of the lumen surrounding barrel wall and reduces the pore diameters from 35 × 25 Å to about 22 Å × 25 Å (Fig. 4-17C).

4.4.2.4 Density improvement by *B*-factor sharpening

A further improvement of the obtained low resolution maps was carried out by *B*-factor sharpening during fast Fourier Transformation^[107]. The application of a negative *B* factor, B_{sharp} results in the up-weighting of the higher resolution terms and therefore to an enhancement of the details of higher resolution features such as secondary structural elements. Since B_{sharp} could be considered as a pseudo Wilson scaling of the diffraction data^[107], an appropriate value can be figured out by the B_{sharp} dependent expectation of the corresponding plots. An optimal B_{sharp} value should produce a Wilson plot which is just positive against all resolution bins and was accordingly specified to -160 in the case of the collected HVDAC1 data. As a result of the *B*-factor sharpening the maps exhibited distinct continuous density stretches in several regions of the barrel shaped structures. These stretches are arranged parallel at intervals of approximately 4.5 Å (Fig4-18B).

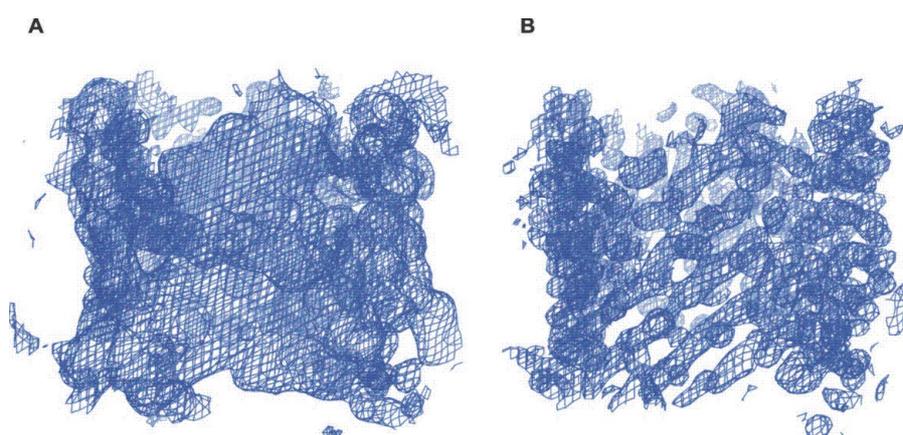


Figure 4-18: Effect of the applied *B*-factor sharpening.

The implementation of a negative *B*-factor^[107], B_{sharp} enhanced the resolution of higher resolution features such as β -strands. $F_{\text{sharpened map}} = \exp(-B_{\text{sharp}} \sin^2 \theta / \lambda^2) \times F_{\text{map}}$ ^[107]. (A) Original low resolution map. (B) *B*-factor sharpened map. Maps are displayed in the same orientation. (applied σ level = 1.0).

Since it is very unlikely that such topologies may have been derived from the method inherent noise level enhancement, the observed stretches are clearly indicative for β -stranded elements and their inclination angle against the barrel axis of HVDAC1.

4.4.2.5 Map interpretation

Subsequent interpretation of the B -factor sharpened maps was initiated by computerised placing trials of several fragmented beta barrel protein structures.

Following this strategy, the best solution was found for an eight stranded fragment which was generated on the basis of the bacterial porin Omp32. The used fragment includes the β -strands between the residues 170-180, 183-195, 200-214, 218-229, 236-248, 253-264, 269-281 and 287-297. Based on this fragment, MOLREP was able to fit two of these half-barrels into the density of the applied map. This results in a twofold disconnected 16- stranded β -barrel (Fig. 4-19).

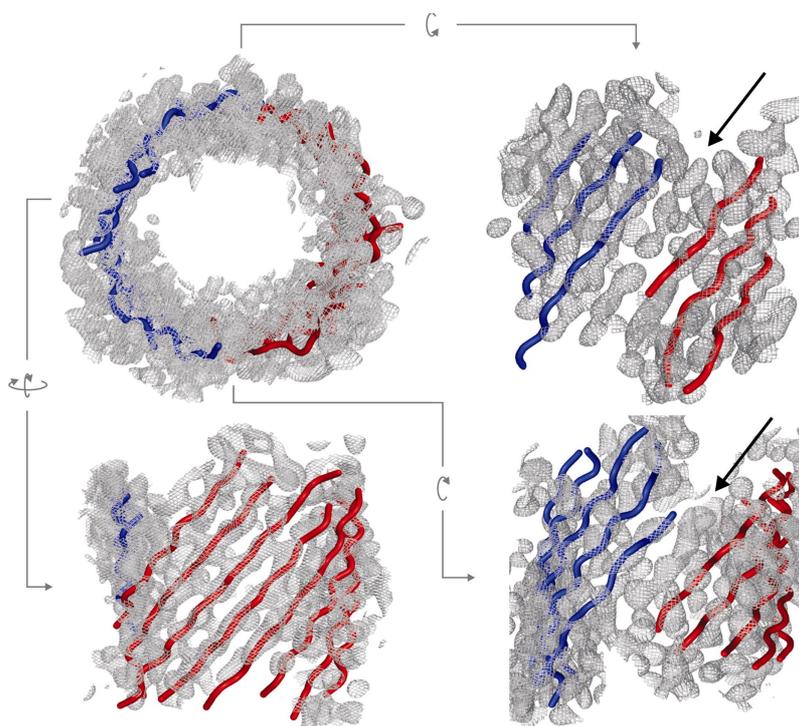


Figure 4-19: Placement of half-barrels into the HVDAC1-His₆ density.

Two 8-stranded fragments (red, blue) were generated on the basis of the porin OMP32 and could be computationally fitted into the B -factor sharpened density of HVDAC1. The placed fragments are separated from each other by two gaps. Both gaps exhibit additional extra density of particular one further β -strand (\rightarrow). (applied σ level = 1.2)

However, both gaps clearly exhibit extra density stretches which can be assigned to particular one further potential β -strand. (Fig 4-19). Therefore, two further strands were manually placed into the remaining density and led to the construction of a closed 18-stranded β -barrel. The emerged β -barrel could be successfully placed by MOLREP and manually refined. Nevertheless, the additional density feature which expands perpendicular to the channel axis along a third of the inner channel wall remained unexplained by this approach (Fig. 4-20). However, the overall shape of this feature suggests an α -helical structure in this part of the density and refers in all probability to the position of the N-terminal α -helix of HVDAC1.

For further investigations several SeMet mutants of HVDAC1 were generated. So far, a set of suitable crystals were obtained for the mutants L13M and I230M. Even if these crystals diffracted only to a resolution of about 5.3 Å they could still be used to locate the corresponding selenium sites. According to the determined positions resides the Se atom of I230M in the immediate vicinity of the outer barrel wall on the opposite side of M158. The Se atom of L13M was determined at the interface between the inner barrel wall and the density of the potential α -helical structure.

Thus, the detected Se position of L13M assigned the barrel-internally observed density unambiguously to the N-terminal α -helix of HVDAC1. This α -helix runs perpendicular centered along a section of the inner barrel-wall which is defined by M158 and I230 (Fig. 4-20).

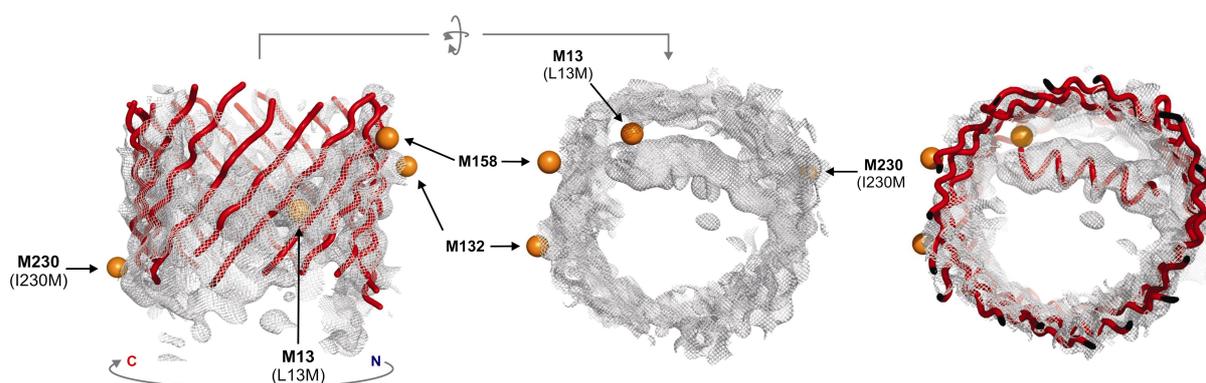


Figure 4-20: Orientation of the N-terminal α -helix of HVDAC1.

Based on the observed density stretch in the barrel interior and the selenium position of L13M runs the N-terminal α -helix perpendicular centered along the inner barrel wall between residues M158 and I230. Left illustration: Lateral view; Middle and right illustration: Top view. (applied σ level = 1.0). Determined selenium positions are indicated by orange spheres. Labels refer to the appropriate selenomethionine residues.

4.4.3 Combination of X-ray and NMR data

Unfortunately, both methods particular failed in structure determination of the HVDAC1 topology. Nevertheless, NMR and X-ray investigations provide a large extend of structural information. As such the NMR investigations led to the establishment of a two dimensional model for the C-terminal 80% of HVDAC1. Apart from that, the interpretation of the X-ray data disclosed the secondary structural topology of the channel at low resolution. Consequently, the respective informations of both methods were complementary combined in order to gain a more detailed HVDAC1 model.

Based on the selenium sites of M132, M158 and I230M it was possible to consistently apply the 14-stranded NMR model on the X-ray derived β -strand distribution (Fig.4-21).

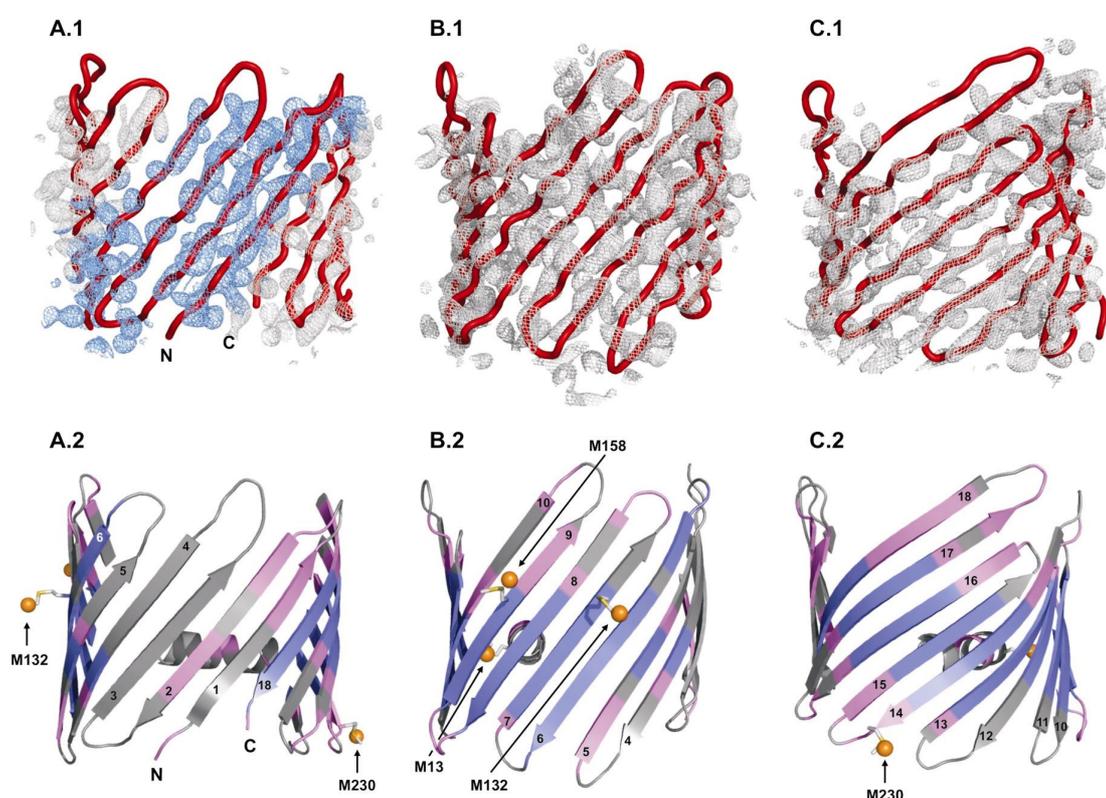


Figure 4-21: Combined NMR-X-ray model of HVDAC1.

Improved HVDAC1 model after combining the two dimensional NMR model and the X-ray derived β -strand topology. **Upper row:** Tube cartoon representation of the derived model and its fit into the B -factor sharpened density of HVDAC1 (applied σ levels = 2.0). The density stretches colored in blue refer to the NMR unassigned region of the model. Representations are laterally depicted in approximately 60° increments. **Lower row:** Cartoon representation of the derived HVDAC1 model. Orientations correspond to the upper row. The 18 β -strands are consecutively numbered from the N- to the C-terminal end of the protein. NMR assigned residues are represented by the regions coloured in magenta and blue. The blue regions refer furthermore, to residues which do not exchange with D_2O after 1 h. Orange spheres refer to the X-ray derived positions of the selenium sites of M13, M132, M158 and M230. The methionine side chains of the residues M13, M132, M158 and M230 are correspondingly docked as common rotamers to their NMR assigned positions.

The topology thereby achieved coincides with both the given positions of the selenium sites as well as with the overall shape of the electron density in the assigned region. The combined NMR-X-ray model therefore provides a more detailed description of the HVDAC1 topology albeit only for the NMR assigned parts of the protein.

However, four further parallel density stretches are clearly detectable in the gap between the NMR assigned β -sheets (Fig. 4-21 A.1). At least a part of the N-terminal unassigned region has hence to be folded into four additional β -strands, thereby closing the barrel.

4.4.4 Topology of HVDAC1

With regard to the topology the HVDAC1 sequence can be divided into two parts. The first part, which covers approximately the N-terminal 10% of the sequence, forms consecutively the N-terminus, the α -helix and the linker to the channel wall. The second part, which covers the C-terminal 90% of the sequence, folds into 18 anti-parallel β -strands, thereby forming the closed channel wall in an all next neighbour conformation (Fig.4-22C, D).

Relative to the channel axis all of these strands are right tilted and right hand twisted (Fig.4-23C, D). However, the tilt angles of the individual β -strands are not constant and vary along the channel perimeter. As defined by the observed density stretches the tilt angle changes from approximately 40° in the N-terminal half, to about 55° in the C-terminal section of the barrel (Fig, 4-21 A.1-C.1).

In general, there are two parameters to describe a β -barrel structure. These are the number of the β -strands n and as a measure of their offset the shear number S [115]. S and n are directly related to the mean tilt angle α and the mean barrel radius R . Taking the common β -sheet parameters such as an intra-strand distance of $a = 3.3 \text{ \AA}$ and an inter-strand distance of $b = 4.4 \text{ \AA}$ into account this relation can be expressed by the following equations.

$$R = \frac{[(Sa)^2 + (nb)^2]^{0.5}}{2\pi} \quad \tan \alpha = Sa/nb$$

Based on the 18 β -strands and a barrel diameter of 35.5 \AA , HVDAC1 exhibit a shear number of 24 and an average tilt angle of 45° (Fig. 4-22).

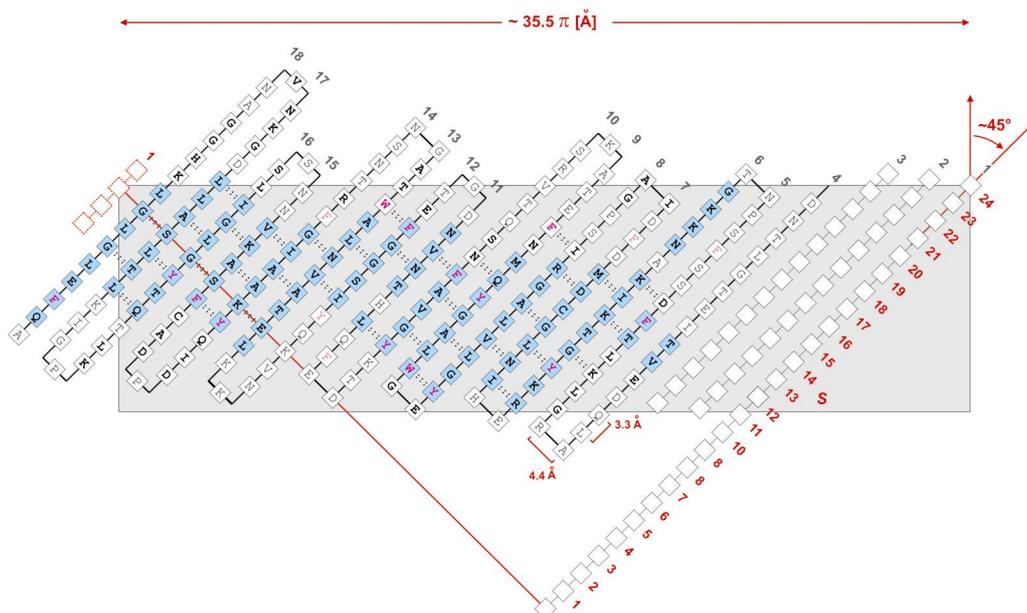


Figure 4-22: Shear number and mean tilt angle of the HVDAC1 β -barrel .

HVDAC1 is cut at the first strand and represented in a way that it is viewed from the outside of the flattened barrel. Strands are numbered from the first to the 18th. Residues which are assigned by NMR are shown as bold characters in the one letter amino acid code. Residues coloured in magenta refer to the position of aromatic amino acids. Residues which do not exchange with D₂O after 1 h are indicated by blue boxes. The gray coloured area resembles with 112 x 30 Å the central area of the channel wall at the C_α backbone. The shear number *S* is derived by running from a certain strand along the hydrogen bonds once around the barrel until this strand is reached again (depicted by the red line). *S* corresponds to the residue offset between the start and the point of return on the same β -strand. HVDAC1 exhibits a shear number of 24. The tilt angles of the 18 β -strands averages 45°.

On one side of the barrel the individual β -strands of HVDAC1 are connected by short β -turns and on the other side by β -turns or loops of various lengths. Due to the shorter loops between, e.g. β -strands 11, 12 and 15, 16 and the longer ones between e.g. β -strands 9, 10 and 13, 14 as well as 17, 18 the barrel wall becomes irregular and varies between 30 and 38 Å in height (Fig. 4-23B). Because of the different loop lengths, the barrel edge is twofold notched in this region.

The twofold notched region between strand 10 and 17 also resembles the part of the barrel closest to the N-terminal α -helix. According to the observed density stretch, the selenium position of L13M, and the main chemical shift perturbations of the V20C mutant, this helix runs almost perpendicular to the channel axis along the inner side of this twofold notched barrel wall region (Fig. 4-23 A, B). In relation to its vertical position, the α -helix is located between the middle and the lower third of the barrel (Fig. 4-23 B).

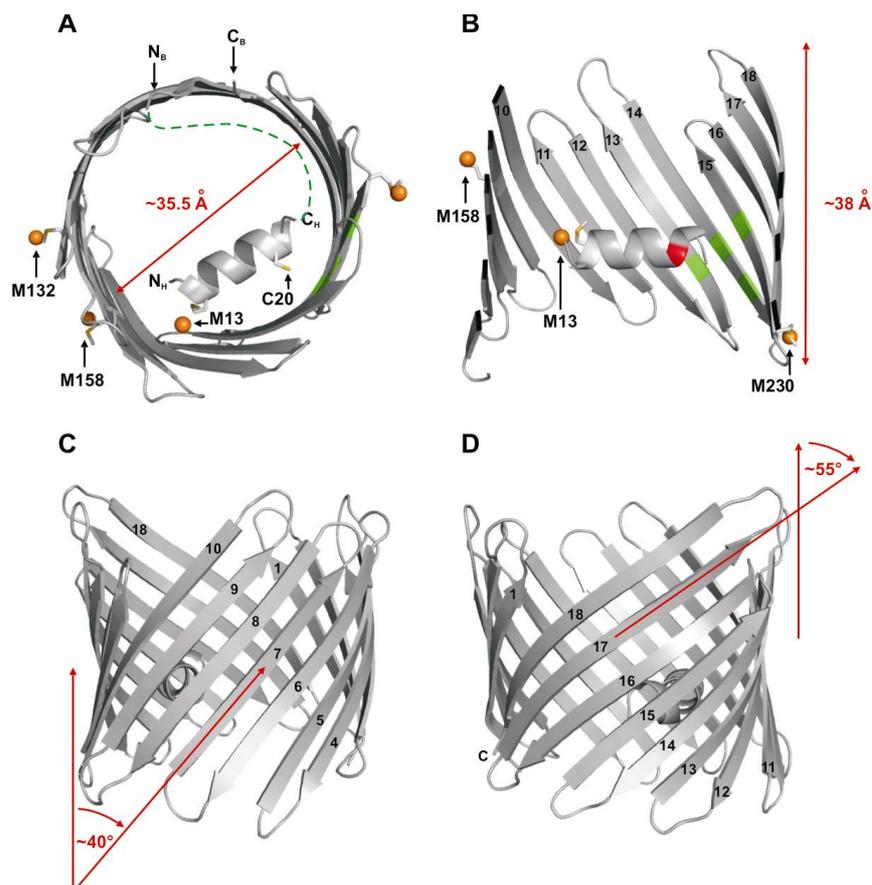


Figure 4-23: Topology model of HVDAC1.

The topology of HVDAC1 is composed of an N-terminal α -helix which folds into an 18 stranded β -barrel. **A:** HVDAC1 in a view from the bottom. The obligatory but so far unobserved linker between the N-terminal α -helix and the first β -strand of the channel wall is represented by the dashed green line. **B:** Representation of the twofold notched region between strand 10 and 17 where the N-terminal α -helix is closest to. Residues which exhibited strong chemical shift perturbations upon spin labeling of C20 (red) are marked in green. **C/D:** Lateral views of the barrel in different orientations. The β -strands of the N-terminal and C-terminal half are tilted by about 40° and 55° , respectively.

This N-terminal α -helix exhibits an amphiphilic surface pattern whereas hydrophobic residues accumulate on one side of the α -helix while the other side is occupied by charged and polar residues. Due to the selenium position of L13M and the observed shift perturbations of the V20M mutant, the nonpolar side faces the channel wall while the charged residues extend into the barrel lumen (Figs. 4-23B, 4-24A).

The surface of HVDAC1 was displayed by the attachment of side chains in their common conformations to the NMR assigned residues. As a result, it turned out that the outer surface of HVDAC1 is strictly unpolar in a central band of about 25 \AA around the barrel (Fig. 4-24 B.1, B.2).

On both sides of its borders the band exhibits a noticeable accumulation of aromatic residues, thereby forming an aromatic girdle (Fig. 4-24B). Charged and polar residues of the outer surface are exclusively distributed in loops as well as above and below the border of the unpolar region (Fig. 4-24B.1).

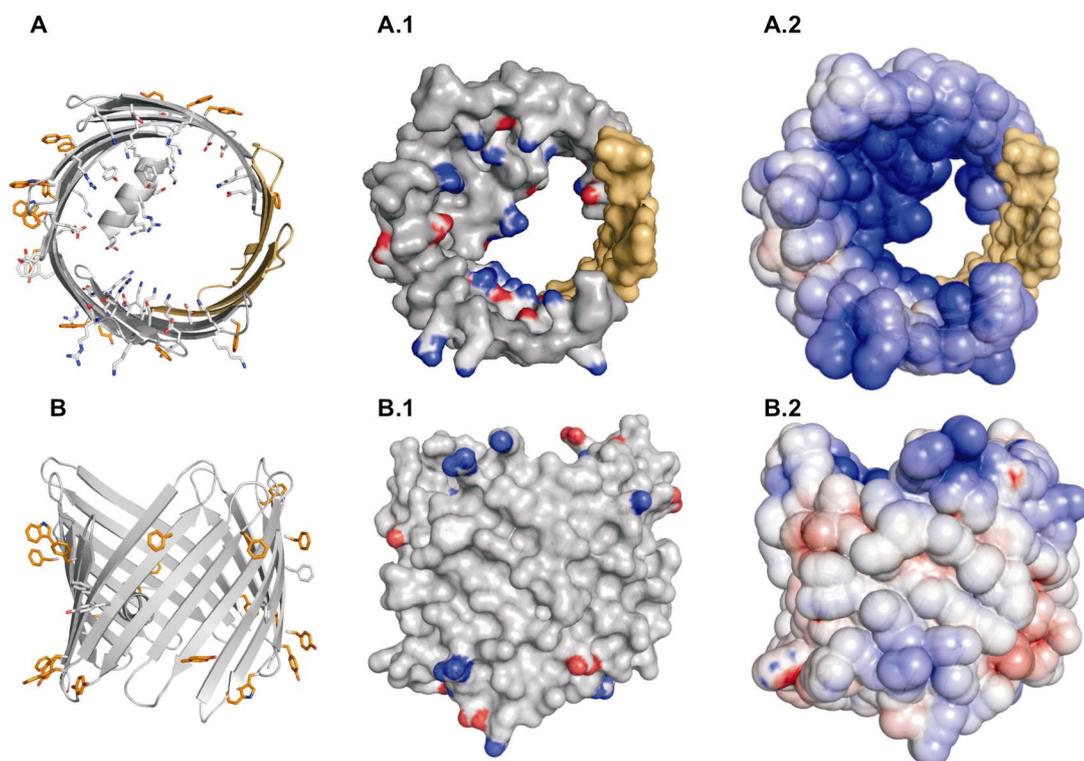


Figure 4-24: Distribution of aromatic and charged residues on the surfaces of HVDAC1.

Amino acid side chains were attached in common rotamers to their appropriate residues in the assigned region. HVDAC1 is illustrated in a top and lateral orientation. The unassigned section of the barrel is represented in dark yellow. **A,B:** Cartoon representation of the channel backbone. Aromatic and charged residues are presented as sticks. Aromatic residues which lie at the border of the unpolar band are coloured in orange. **A.1,B.1:** Charged residue distribution of the channel in a surface representation. **A.2,B.2:** Representations of the solvent accessible surface potential. The surface potential is linearly plotted from -5 (red) to +5 kt/e (blue).

By contrast, the channel interior is almost ubiquitously charged and polar at the barrel wall and on the hydrophilic face of the N-terminal α -helix (Fig. 4-21A,A.1). However, the wall region which is directly covered by the N-terminal α -helix as well as two further grooves in the channel wall are free of charged residues. Concerning the overall solvent accessible surface potential it turns out that the channel interior is continuously positive in the assigned regions (Fig.4-24 A.2).

4.5 Interaction between HVDAC1 other proteins and compounds.

Since the channel is suggested to act as a binding site for other proteins and small compounds, HVDAC1 was tested on its capability to interact with the pro-apoptotic proteins Bid and Bax as well as with ANT and the N-terminal peptide of Hexokinase II. Further examinations were applied concerning the possible binding sites for ATP and the antidepressant fluoxetine (a selective serotonin reuptake inhibitor).

4.5.1 Preparation of mouse Bid and the bovine adenine nucleotide translocator.

4.5.1.1 Expression and purification of mouse BID (mBid)

mBid has been successfully produced in an *E. coli* BL21CodonPlus strain. By this strategy about 97 g wet cells were obtained from 12 l culture. Effective overproduction of mBid was indicated by SDS-PAGE through an eminent protein band of about 25 kDa. Purification by Ni-affinity chromatography and gel filtration finally led to an almost pure mBid fraction (Fig. 4-25A).

Gel filtration suggests that mBid exists predominantly as a dimer but also in a mono- and several oligomeric forms. Since Bid was not found to form homo-dimers so far^[16], only the monomeric fraction was pooled and used in the following experiments. Per litre culture about 2 mg of monomeric mBid were available after purification.

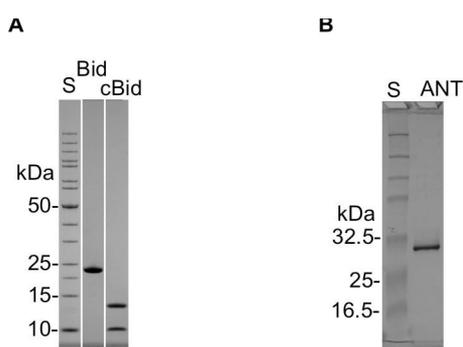


Figure 4-25: Purification of mouse Bid and bovine ANT.

Mouse Bid was over-expressed in *E. coli* and afterwards purified by Ni-affinity and size exclusion chromatography. **A:** Coomassie stained SDS gel of Bid after size exclusion chromatography and cBid after caspase-8 cleavage and Ni-affinity chromatography. Bovine ANT was prepared from bovine heart mitochondria by ion exchange and size exclusion chromatography. **B:** Coomassie-stained SDS gel of purified bovine ANT after gel filtration. (S: Protein marker)

The over-expressed and purified mBid corresponds to the inactivated precursor of the pro-apoptotic form cBid. Naturally, Bid is activated to cBid by caspase-8 cleavage during the mitochondrial cell death cascade. Therefore, a part of the overproduced form was further processed by caspase-8 cleavage *in vitro*. Interestingly, mcBid did not dissociate into two domains despite cleavage by caspase-8 (Fig. 4-25A). This was indicated by the fact that both parts elute simultaneously from the Ni-column although only the N-terminal part was His-tagged. However, an analysis of the mcBid containing fraction by SDS-PAGE shows clearly two bands and is hence indicative for the successful processing by caspase-8.

4.5.1.2 Purification of the adenine nucleotide translocator (ANT) from heart mitochondria

Mitochondria corresponding to about two 2 g of mitochondrial protein could be isolated from 2 kg of a fat freed bovine heart. About 1.2 mg pure bovine ANT could be purified from 160 mg of total mitochondrial protein by ion exchange and size exclusion chromatography (Fig. 4-25B).

4.5.2 Interaction between HVDAC1 and the Bcl-2 family proteins Bid, Bcl-X_L and Bax

A potential interaction between Bid and VDAC has been already suggested due to the mBid induced closure of rat VDAC during conductance measurements^[81]. Based on this proposition HVDAC1 was tested on its probability to bind cBID by chemical- and light-induced crosslinking as well as by NMR.

For crosslinking studies the two proteins were equimolar mixed and either treated by Ru^{II}(bpy)₃²⁺ and an immediate light exposure or by glutaraldehyde. As a result the interaction between HVDAC1 and the N-terminal as well as the C-terminal domain of cBid could be demonstrated by SDS-PAGE (Fig. 4-26A,B) and mass finger print analysis. Glutaraldehyde treatment give also rise to VDAC internal crosslinks as indicated by a noticeable lower molecular weight due to an increased compactness of the channel (Fig. 4-26 C)

Furthermore, both experiments show the formation of HVDAC1 homodimers albeit to a much lower extent in the Ru^{II}(bpy)₃²⁺ experiment (Fig. 4-26 B-C). Higher HVDAC1 homooligomers occurred only in slight traces and exclusively in the glutaraldehyde experiment. Interestingly, in both experiments the formation of HVDAC1 homodimers was significantly decreased in the presence of cBID (Fig. 4-26 B, C). Therefore, at least one of the cBID domains has to bind close to the HVDAC1 dimerisation site.

The glutaraldehyde experiment was also performed in the presence of 2% n-octyl- β -D-glucopyranoside (β -OG) to investigate the intermolecular forces involved in these interactions. As a result, the appearance of the complexes diminished but was still distinctively detectable (Fig. 4-26 C). This suggests that also electrostatic interactions play a role in the formation of homodimeric HVDAC1 and heterodimeric HVDAC1/cBid complexes.

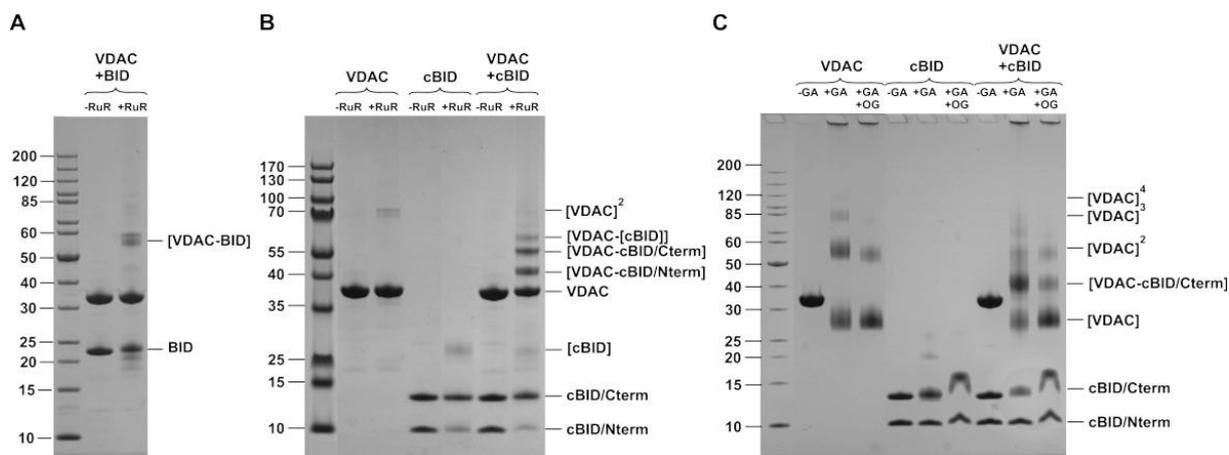


Figure 4-26: Chemical and light induced crosslinking of HVDAC1, mouse Bid and cBid.

HVDAC1 and mouse Bid or cBid were equimolar mixed and either treated by RuII(bpy)₃²⁺ or glutaraldehyde. **A:** Coomassie stained SDS gel of RuII(bpy)₃²⁺ (RuR) treated HVDAC1 and Bid samples (+RuR) and their RuR free (-RuR) controls. **B:** Coomassie stained SDS gel of RuII(bpy)₃²⁺ (RuR) treated HVDAC1 and cBid samples (+RuR) and their RuR free controls -RuR. The protein constituents of the perceptible bands are labelled in accordance to the results of the performed MALDI mass fingerprint analysis. **C:** Coomassie stained SDS gel of glutaraldehyde (+GA) and GA/n-octyl- β -D-glucopyranoside (+GA, +OG) treated VDAC and cBid samples and their controls (-GA).

Moreover, ¹⁵N-TROSY-HSQC spectra of ²H,¹⁵N-labelled HVDAC1 were recorded in the presence of mouse Bid and cBid in order to locate the Bid binding sites on VDAC. The chemical shift and intensity changes thereby detected clustered predominantly in the C-terminal region between the residues L205 and A286 (Fig. 4-27). Beyond this region further effects were detected at the C-terminal end of the N-terminal α -helix for residues R18, K23 and Y25 (Fig. 4-26). Though these residues are far away by sequence, they are located in a close proximity to the primarily affected region due to the spatial position of the N-terminal α -helix. Therefore, the effects observed at the C-terminal end of the N-terminal α -helix are likely to result indirectly from the interaction between Bid and the primarily affected region between L205 and A286.

A more expanded area of interaction was observed by the utilisation of an MTSL labelled Bid version. As a result several further affected residues could be determined. These enclose the region between L205 and A286 almost semicircular towards the last C-terminal and the first N-terminal β -strands of the barrel. Hence, Bid interacts with VDAC in a mode which directly influences the residues around β -strand 14 and moreover the region from there beyond the barrel junction to the first strands of the N-terminal barrel part.

By using cBid instead of Bid, it turns out that the same residues were affected. However, the performed titrations exhibited an interesting difference concerning the amounts of Bid and cBid which had to be applied to induce a significant effect in the ^{15}N -TROSY-HSQC spectra. While an equimolar ratio between cBid and HVDAC1 was already sufficient, Bid had to be applied in fourfold molar excess. Consequently, caspase-8 activation of Bid induces an enhanced affinity of its apoptotic form cBid to HVDAC1.

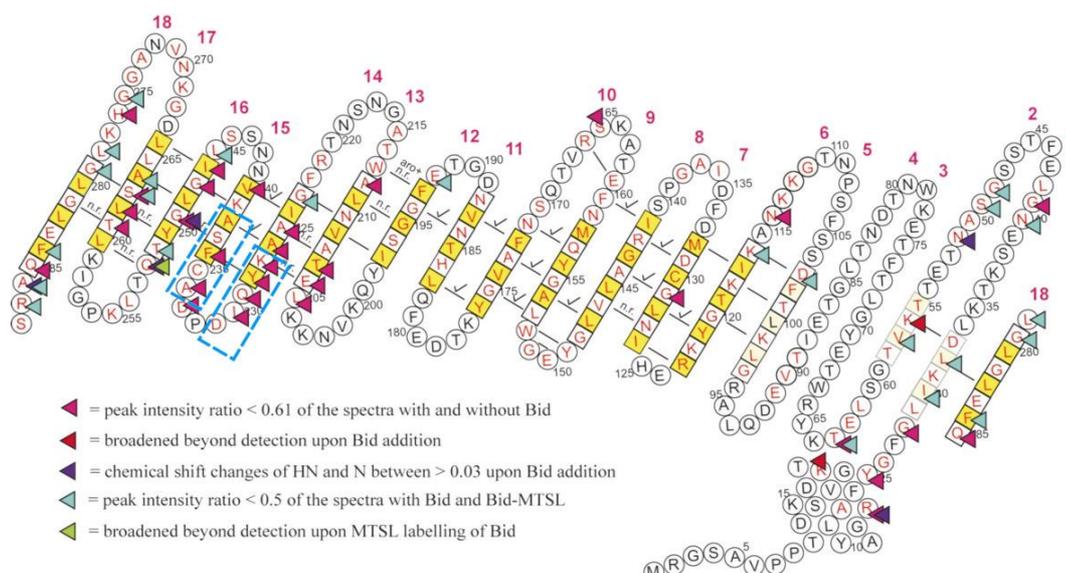


Figure 4-27: Predominant affected residues of HVDAC1 upon addition of Bid and MTSL labelled Bid.

On the topology model of HVDAC1 mapped chemical shift perturbations as induced by Bid and MTSL labelled Bid. The model was renumbered on basis of the 18 β -strands established by X-ray analysis. However, the exact conformation of β -strands 3 and 4 is still not verified and represented as an eventuality. Residues influenced upon Bid addition are marked by red, magenta and blue rectangles. Predominant affected residues are R18, K23, Y25, L205-T207, A212, A225-I230, D233-A234, F236, V240, I246-G247, G249, Q252, T261-S263, H276, Q285-A286. Residues influenced upon Bid-MTSL addition are marked by green and light green rectangles. Bid-MTSL affected residues are I30, L32, N40, G48-S49, V57, T63, D103, K116, E192, G223, L245, T251, Q252, S263-A264, G275, L278-G279, F284, A286, R287. Residues solely influenced by a two helix peptide of Bid (helix 5-6) are indicated by blue boxes around K227-D231 and A234-A238. Utilisation of a synthetic Bid peptide which only consists of helix 6 and 7 affected basically only the blue boxed residues K227-D231 and A234-A238. Almost the same residues were affected by a synthetic Bcl-X_L peptide which consists solely of helix 5 and 6.

Furthermore, the channel was analysed in respect of a helical hairpin motif of Bcl-X_L which was recently shown to interact with HVDAC1^[117]. Since a structural homology between Bcl-X_L and Bid is established^[118], this was also investigated with the corresponding motif of Bid. For this purpose a peptide of the Bcl-X_L hairpin motif and its Bid analog were synthesised and titrated against HVDAC1. According to the NMR chemical shift differences both peptides bind almost identically to a limited area within the described Bid binding site (Fig. 4-27, 4-28). This area comprises the end of β -strand 14 between K227 and D231 and the beginning of β -strand 15 between A234 and A238.

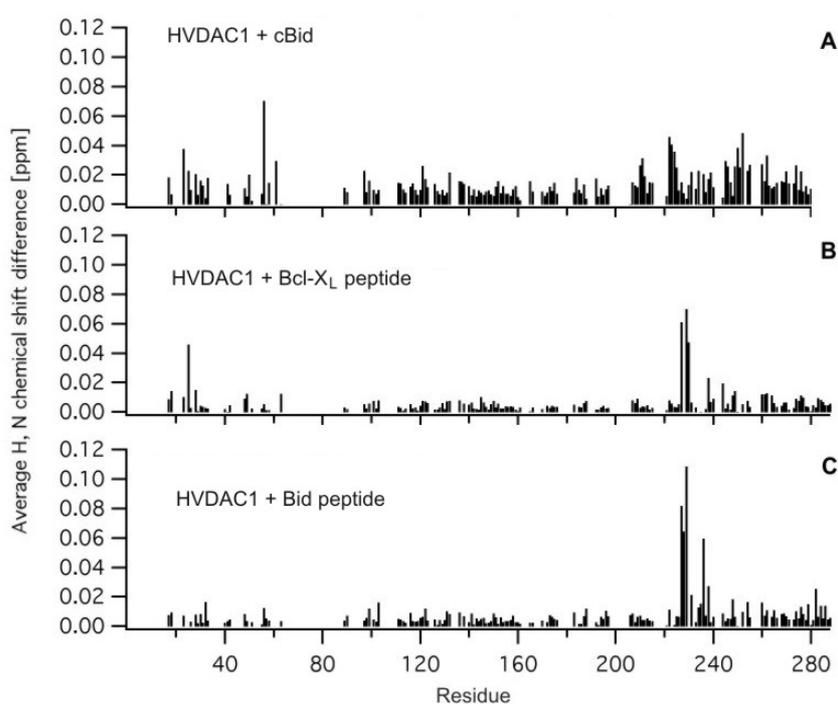


Figure 4-28: HVDAC1 TROSY-HSQC spectra upon addition of cBid or the Bid and Bcl-X_L peptides.

HN and N chemical shift changes upon addition of cBid (A), a peptide covering the Bid helices 6 and 7 (B) and a peptide covering the Bcl-X_L helices 5 and 6 (C). Shift changes are plotted against all assigned HVDAC1 residues. The hairpin motifs of both peptides affect almost the same region in a limited area of the by cBid affected region. Interestingly, the helical hairpin motifs of the proapoptotic protein Bid as well as of the anti apoptotic protein BclX_L interact both with almost same site of HVDAC1.

Among the so far structurally described proteins of the Bcl-2 family also BAX exhibits a topology similar to the fold of Bid and Bcl-X_L. Accordingly, all three comprise the hydrophobic α -helical hairpin motif which become potentially inserted into the membrane upon activation^[119]. Since, it could be assumed that also the pro-apoptotic protein Bax binds to HVDAC1 this was also tested.

A potential interaction between Bax and HVDAC1 was investigated by light induced crosslinking in absence as well as in presence of mouse Bid and cBid. However, in contrast to Bid and cBid no significant interactions between HVDAC1 and Bax could be detected, neither with Bax alone nor in presence of Bid or cBid (Fig. 4-29).

In contrast, interactions between Bax and Bid or Bax and cBid were detectable but not further investigated in the scope of this study. Interestingly, these interactions had, however, no remarkable effect on the interaction between HVDAC1 and Bid or cBid since both complexes remained unaffected by the presence of Bax (Fig. 4-29). A significant affinity of Bid and cBid towards HVDAC1 can therefore be concluded.

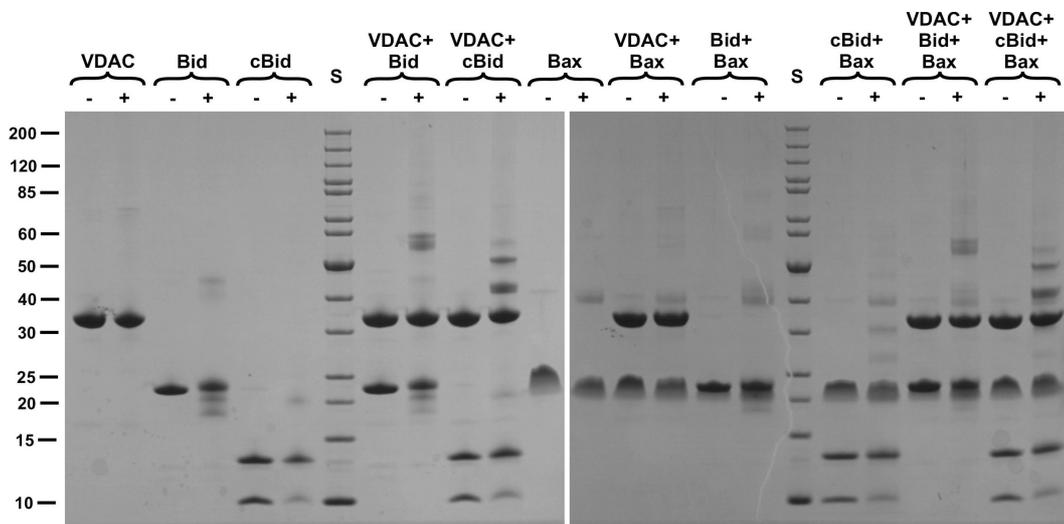


Figure 4-29: Light induced crosslinking of HVDAC1 and the pro-apoptotic protein Bax.

Proteins were mixed in equimolar amounts, treated by Ru^{II}(bpy)₃²⁺ and exposed to light for 0.1 s. All samples were subsequently analysed by SDS-PAGE. The Coomassie-stained SDS gels of this analysis are depicted. Ru^{II}(bpy)₃²⁺ treated samples are indicated by (+), Ru^{II}(bpy)₃²⁺ free controls by (-).

4.5.3 Interaction between HVDAC1, ANT and the N-terminal α -helix of hexokinase II.

VDAC is furthermore supposed to act as a part of a highly organised "energy transport channel" and the permeability transition pore (PTP)^[73]. In both complexes the channel is thought to interact with the adenine nucleotide translocator (ANT) at inner and the cytoplasmic hexokinase at the outer side of the outer mitochondrial membrane. Therefore, HVDAC1 was also tested on its capability to interact with bovine heart ANT. However, such an interaction could not be proven by light induced crosslinking.

Moreover, it was also tested if the addition of Bid or cBid facilitates the formation of the supposed ANT-VDAC complex. But even in presence of Bid or cBid no ANT/HVDAC1 interaction could be ascertained (Fig. 4-30 A).

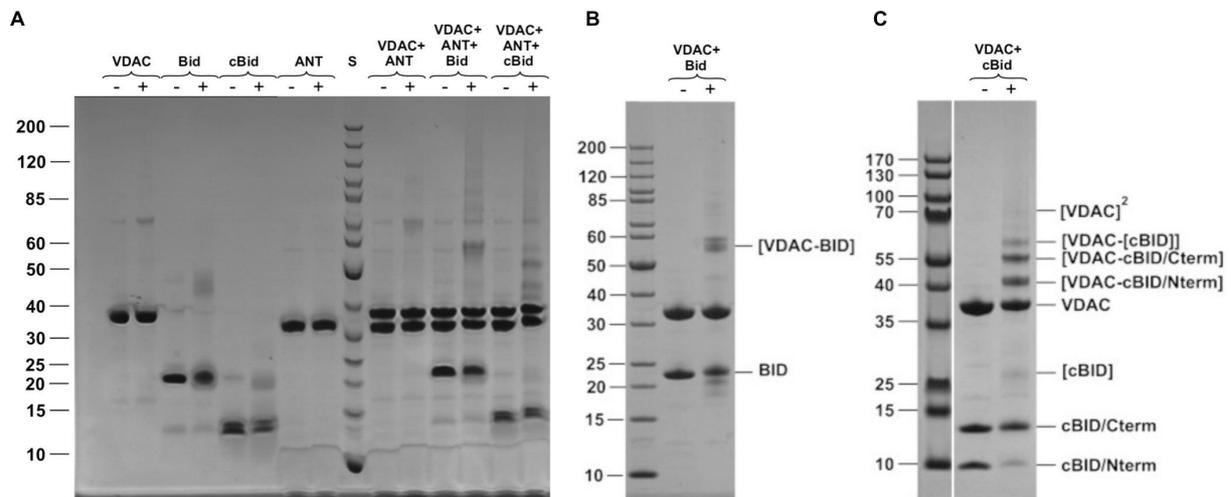


Figure 4-30: Light induced crosslinking of HVDAC1 and bovine heart ANT.

Proteins were mixed in equimolar amounts, treated by $\text{Ru}^{\text{II}}(\text{bpy})_3^{2+}$ and exposed to light for 0.1 s. Treated samples were subsequently analysed by SDS-PAGE. **A:** Coomassie-stained SDS gel of this analysis. $\text{Ru}^{\text{II}}(\text{bpy})_3^{2+}$ treated samples are indicated by (+) the associated $\text{Ru}^{\text{II}}(\text{bpy})_3^{2+}$ free controls by (-). **B,C:** Coomassie-stained SDS gels of VDAC and Bid or cBid interactions for comparison.

Several studies have shown a correlation between the degree of aerobic glycolysis and the level of mitochondrial bound hexokinase in cancer cell lines^[120]. Furthermore, it was shown that in this interaction the mitochondrial receptor is identical to $\text{VDAC}^{\text{C}70\text{[71]}}$. An N-terminal and proteolytic cleavable hexokinase domain was identified to be essential in this interaction^{[121][122]}.

To examine the suggested interaction between hexokinase and HVDAC1, the hydrophobic N-terminal α -helix of hexokinase II was synthesised and tested on HVDAC1 by NMR. As a result, several chemical shift changes were observed in the C-terminal region of HVDAC1 upon addition of the hexokinase II peptide.

Compared to the cBid interaction site the affected region is more broadened and exhibits the strongest shift changes in the area between β -strands 15 and 17 (Fig. 4-31 A, B). Interestingly, even though slightly shifted the N-terminal α -helix of hexokinase II binds basically within the same interaction area than the cBid protein (Fig. 4-31 A, B).

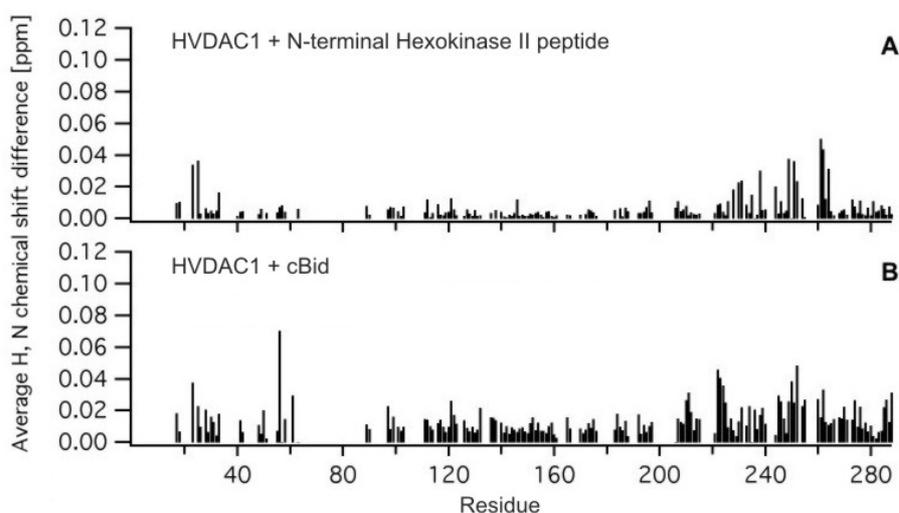


Figure 4-31: HVDAC1 HN and N chemical shift changes upon addition of the N-terminal peptide of hexokinase II.

A: HN and N chemical shift changes of the HVDAC1 ^{15}N -TROSY-HSQC spectrum upon addition of the N-terminal peptide of human hexokinase II. **B-D:** HN and N chemical shift changes upon addition of cBid and the peptides of the Bid and Bcl-X_L hairpin motifs.

4.5.4 Interaction between HVDAC1 and small molecules

4.5.4.1 ADP-titration

Functionally, VDAC is primarily involved in limited exchange of ATP, ADP and small hydrophilic molecules across the outer mitochondrial membrane.

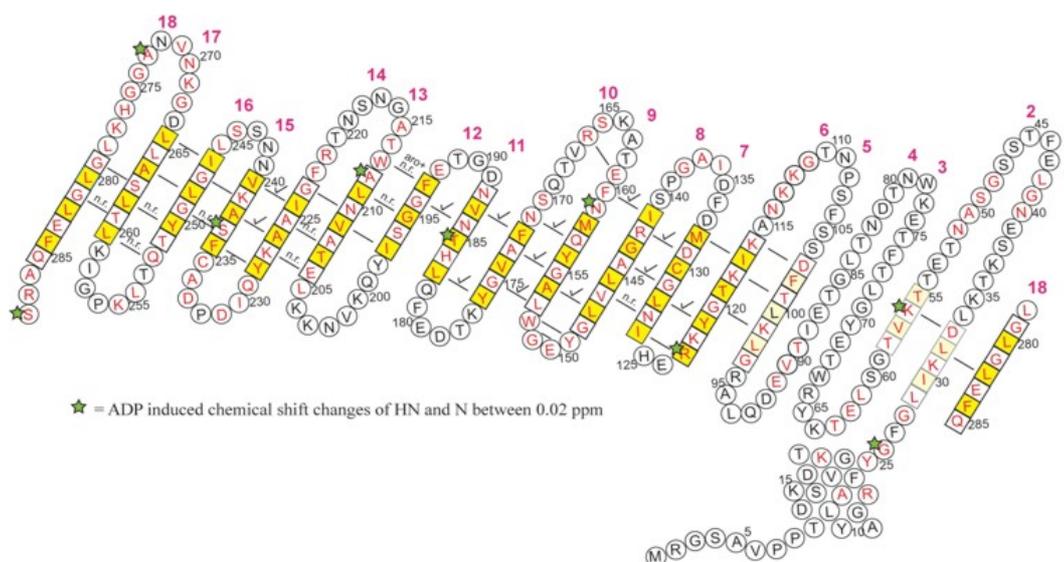


Figure 4-32: By ADP affected residues of HVDAC1.

Residues which showed perturbations above 0.02 ppm are labelled with a green star. Affected residues are G26, K56, R123, N159, T185, A212, S237, A273 and S288.

4.5.4.2 Fluoxetine-titration

Fluoxetine acts as a selective serotonin re-uptake inhibitor and is used as an active pharmaceutical compound in antidepressants such as Prozac[®] and Fluclin[®]. Recently, it was shown that fluoxetine also binds to VDAC, thereby shifting the voltage dependency of the channel to a significant lower potential^[123].

In order to identify a specific binding site, a titration up to the 32-fold excess of fluoxetine was performed and monitored by chemical shift changes in the ¹⁵N-TROSY-HSQC spectra of HVDAC1. Interestingly, most of the chemical shift perturbations were found to be clustered in the last C-terminal loop in-between V271 and L278 (Fig. 4-33) The shift changes thereby observed, identify the last C-terminal loop of HVDAC1 as a specific binding site for fluoxetine.

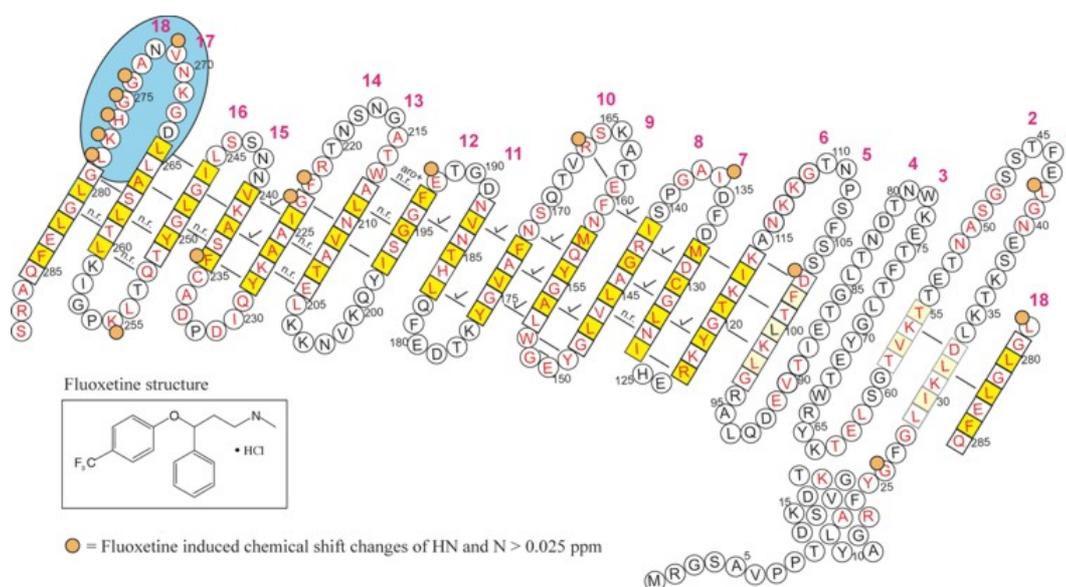


Figure 4-33: By fluoxetine affected residues of HVDAC1.

Residues which showed perturbations above 0.025 ppm upon fluoxetine titration are labelled by yellow circles. The specific fluoxetine binding site between V271 and L278 is highlighted by a blue circle. Further affected residues on the same side of the channel are L42, D103, I136, R166, E192, F222, G223. Other affected residues are G26, F234 and K255.

4.5.4.3 Calcium (II) chloride an gadolinium (III) chloride titration

Ca²⁺ binding to VDAC is reported to exert a regulatory influence on the channel and the permeability transition pore^[124]. Therefore, HVDAC1 was tested for potential Ca²⁺ binding sites by NMR.

Although the titrations were carried out with up to a 32-fold molar excess of Ca^{2+} , no chemical shift or peak intensity changes could be observed in the corresponding ^{15}N -TROSY-HSQC spectra.

As it is further published that Ca^{2+} could prevent VDAC closure induced by lanthanoides or ruthenium red and that this effect might be due to a similar interaction site^[125], also gadolinium (III) chloride was tested. Gd^{3+} is in contrast to Ca^{2+} paramagnetic. Due to the paramagnetic relaxation enhancement much stronger effects on the ^{15}N -TROSY-HSQC spectrum are expected in case of Gd^{3+} interaction. The utilisation of Gd^{3+} resulted in several distinct chemical shift and peak intensity changes predominantly clustered within a continuous region between the β -strands 14 and 18. Interestingly, the Gd^{3+} interaction site resides in the same region as determined for Bid and the hexokinase II peptide.

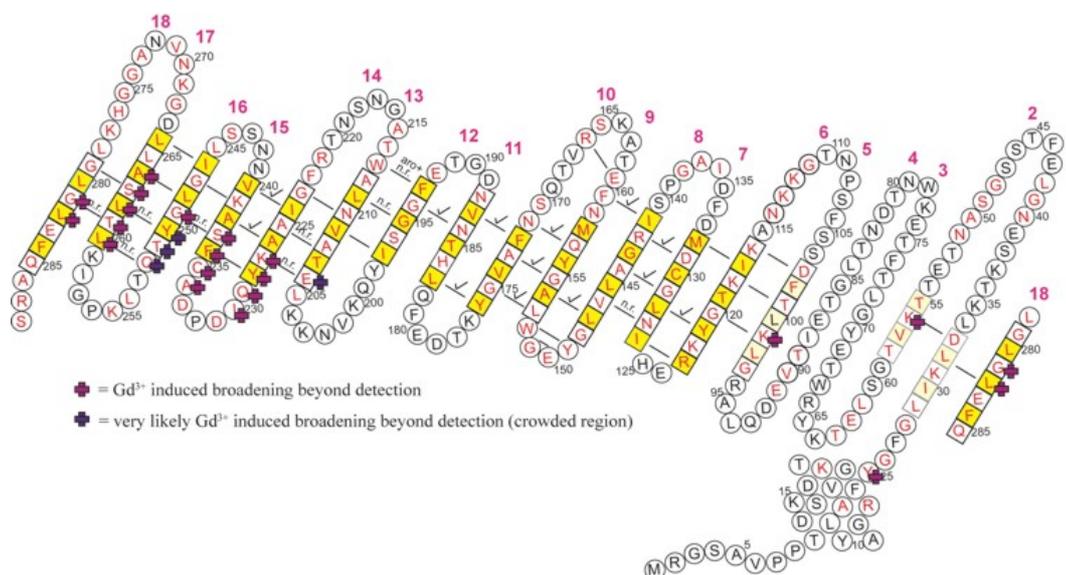


Figure 4-34: By gadolinium (III) chloride affected residues of HVDAC1.

Residues which are broadened beyond detection by an equimolar amount of GdCl_3 are labelled by a red cross. Residues which are due to overlaps not unambiguously broadened beyond detection are labelled by a blue cross. Affected residues are E204, K227-I230, A234-S237, G249-Q252, L260-A264 and Q281-L282.

The fact that several proteins and compounds like Bid, Hexokinase II, Gd^{3+} and fluoxetine bind all in the region between the C-terminal β -strands 13 and 18 reveals this region of HVDAC1 as an important binding domain in the outer mitochondrial membrane and, thus, as an important site for the interplay between mitochondria and the cell.

5 Discussion

Voltage dependent anion-channels especially of mammalian and fungal origin have been extensively studied for the last three decades. During this time many investigations have been concerned with the topology of these channels and led by different approaches to the establishment of several structure models (see chap. 2.3.7). However, besides the structural information resulting from single particle analyses of HVDAC1^[55] and 2D-crystals of human and NcVDAC1^{[55][62][39][126][127][67][66]}, further acceptance only exists for the finding that VDAC proteins most likely adopt the classical β -barrel fold of bacterial outer membrane proteins (see chap. 2.3.6).

The lack of detailed structural information might be due to the usual obstacles in membrane protein structure determination such as the availability of sufficient protein and the maintenance of its structural integrity in a membrane mimicking detergent environment. Limited amounts of the protein are, however, not an issue since wild type^[18] as well as recombinant VDAC are highly available^{[54][53]}. Moreover, the successful formation of two dimensional crystals was shown from both sources^{[40][126]} and is hence indicative for a significant homogeneity of the utilized VDAC proteins. Nevertheless, three dimensional crystals of any VDAC are not described in the literature so far. Since the formation of 2D-crystals is carried out by using phospholipids instead of detergents this might be an indication for a certain instability of the channel in detergent micelles.

Such an assumption was recently substantiated by the observation of a slightly decreased β -sheet content of detergent-solubilised channels^[128]. Moreover, the degree of secondary structure and therefore the quality of the fold was described to vary significantly with the detergent type^[128]. Consequently, the choice of an appropriate detergent seems to be mandatory to induce a stable structural integrity as a prerequisite for the formation of 3D-crystals and NMR studies.

With the objective to test the impact of several detergents on the crystal formation of HVDAC1, a C-terminal His-tagged version of this channel was recombinantly overproduced in *E. coli* and refolded due to the formation of inclusion bodies. Since in *E. coli* efficient protein labelling techniques are already established, this strategy also facilitates the production of differentially labelled NMR samples of HVDAC1.

5.1 Overexpression and refolding of HVDAC1

The possibility to refold *N. crassa*, yeast and human VDAC proteins to functional channels was already demonstrated in previous studies^{[40][54][53]}. Following these studies, a slightly modified and His-tagged version of HVDAC1 was expressed in *E. coli*. Similar to previous results^{[55][53]} this approach led to the formation of milligram quantities of HVDAC1. On the basis of pre-purified inclusion bodies an improved two step refolding and purification strategy was developed with the aim to produce sufficient quantities for structural studies by X-ray crystallography and NMR.

Although protein refolding to an intact and functional topology may not necessarily succeed in general, this seems to be accomplished in the case of recombinant HVDAC1. Evidence for a conformational comparability of refolded and natively isolated VDAC proteins derives from conductance and CD spectral properties. The superposition of CD spectra from wild type NcVDAC^[52] and HVDAC1 yielded almost no differences in their spectral characteristics, but considerably differ from to the CD spectrum of bacterial OmpF (Fig. 5-1A, Tab.5-1). Especially in the β -strand indicative region at around 215 nm, both VDAC spectra are indistinguishable and exhibit an identical magnitude at their minimum of molar ellipticity (Fig. 5-1A, Tab.5-1). Thus, these spectra reveal an equal and in comparison to OmpF increased percentage of sequence which folds into β -sheets.

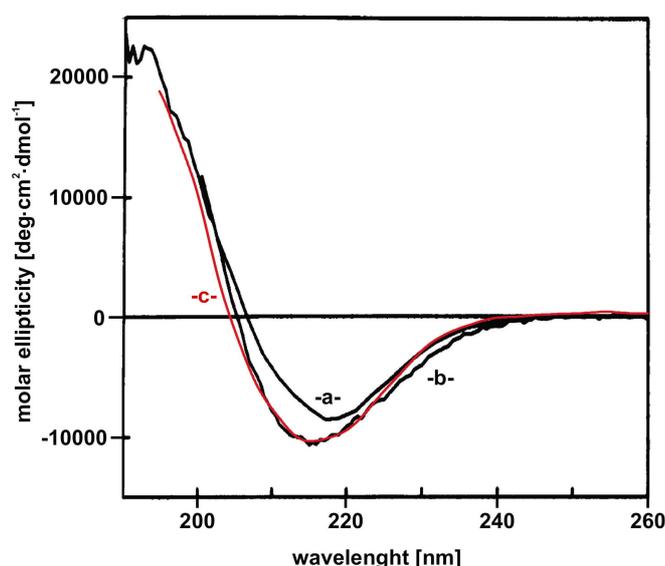


Figure 5-1: Superimposed CD spectra of *N.c.* VDAC1, OmpF and refolded HVDAC1.

Superposition of the recorded HVDAC1 spectrum on published data of *Neurospora crassa* VDAC1 and the bacterial porin OmpF^[52]. (-a-) OmpF in 1% OG; (-b-) NcVDAC in 2% OG; (-c-) HVDAC1 in 0.2% LDAO.

Table 5-1: CD spectral characteristics of HVDAC1-His₆, OmpF and VDAC1 from *Neurospora crassa*.

Protein	$\lambda_{\text{crossover}}$ [nm]	λ_{min} [nm]	min. of molar ellipticity [deg 10 ⁻³ cm ² dmol ⁻¹]
β -sheet [#]	204.5	214.0	-5.2
OmpF [#]	207.0	217.5	-8.5
<i>N.c.</i> VDAC1 [#]	205.5	215.5	-10.0
HVDAC1	204.5	215.0	-10.0

[#]) data adopted from ^[52]

Besides the structural integrity of the refolded channel, HVDAC1 was functionally characterised by its conductance properties. Upon insertion into artificial bilayers all VDAC proteins exhibit a distinctive voltage dependency which is expressed by a change in conductance^[42]. At potentials of about ± 50 mV the conductivity of the channels change characteristically from about 4 nS to 2 nS. The same behaviour was also observed for refolded HVDAC1. Data obtained for HVDAC1 are largely consistent with the known characteristics of several other VDAC proteins (Tab. 5-2).

Table 5-2: Conductance characteristics of VDAC proteins from different sources^[129]

VDAC source	n [#]	V ₀ [mV] [§]	Δ [nS] [*]
Rat liver	2.3	55.0	4.3
Rat kidney	2.5	40.0	4.0
Rat brain	1.0	60.0	4.0
Rabbit liver	1.8	67.0	4.0
Rabbit kidney	2.5	38.0	4.0
Bovine heart	1.6	62.5	n.d
Pig heart	2.0	40.0	3.5
Pig kidney	3.4	35.5	4.0
Paramecium	2.0	32.0	2.4
Yeast	2.0	24.0	4.2
HVDAC1	2.0	57.0	4.3

[#]) number of charges involved in the gating process

[§]) potential at which 50% of the total number of channels are in the closed conformation

^{*}) average single channel conductance

Due to the conductance and CD spectroscopic properties of HVDAC1 it can be assumed that the topology of the refolded channel is conformationally comparable to a natively isolated VDAC protein. Furthermore, the structural and functional integrity of the refolded channel underlines that the addition of the C-terminal His-tag has no bearing on the topology of HVDAC1.

5.2 Structure determination of HVDAC1

The established expression and refolding strategy turned out as a key approach to produce significant amounts of homogeneous and functional HVDAC1 in a detergent solubilised form as prerequisite for the structure determination of membrane proteins. Moreover, the design of this strategy opened the possibility to easily generate labelled and mutated HVDAC1 samples for NMR structural studies and furthermore, to test the impact of a variety of detergents on the formation of 3D-crystals which are of sufficient quality for X-ray crystallography.

In the past, both methods were shown to be suitable to characterise the topology of β -barrel membrane proteins at high resolution. With the objective to generate as much structural information as possible about HVDAC1, NMR spectroscopy and X-ray crystallography were used in a parallel approach. However, in the case of HVDAC1 both techniques reached their limit of applicability and it turned out that neither NMR spectroscopy nor X-ray crystallography alone allowed a complete description of the HVDAC1 topology.

5.2.1 Determination of the 2D topology of HVDAC1 by NMR spectroscopy

Concerning NMR spectroscopy, the main problems in structure determination are attributed to the size of HVDAC1 and furthermore to an enhanced flexibility of its N-terminal domain. So far, three β -barrel protein structures, OmpX^[130], the transmembrane domain of OmpA^[131] and PagP^[132] could be determined by NMR. However, with molecular weights of 16, 19 and 20 kDa all of them are comparatively small and each exhibit a β -barrel of only 8 β -strands. HVDAC1 by contrast, is about 30% bigger in size and composed of an 18 stranded β -barrel. Since NMR spectra become in a progressive rate more difficult to interpret with increasing molecular mass, due to spectral crowding and line broadening as a result of fast transverse relaxation^[133], the size of HVDAC1 is a major problem. In case of a membrane protein this is even more problematic as the molecular weight of the protein becomes further increased by the solubilising detergent. In order to reduce spectral crowding and line broadening, HVDAC1 was produced in a deuterated and selectively labelled version which could be easily attained by the applied production strategy. As a result the recorded ¹⁵N-TROSY-HSQC spectra exhibit an excellent chemical shift dispersion for a protein/detergent complex of this size. Nevertheless, due to strong relaxation, the standard (¹H, ¹³C, ¹⁵N) heteronuclear assignment strategy^[113] was largely impossible to use. One reason for this was the insufficient HVDAC1 concentration of 0.6 mM. In principle, higher HVDAC1 concentrations of up to 1.2 mM were feasible without any significant precipitation but had no improved bearing on the observed signal height.

Therefore, it seems that HVDAC1 starts to form oligomers above concentrations of about 0.6 mM. Such oligomers may be NMR silent due to their increased molecular size which is apparently not large enough to blur the solution to any significant degree. Further problems arose from the fact that spectra of HVDAC1 could not be recorded at temperatures above 37°C since the protein starts to unfold significantly at elevated temperatures. Compared to PagP which was measured at 45°C^[132], the data collection temperature is rather low and accelerate adverse transverse relaxations. The limited temperature during data recording in combination with the size of the protein and the low HVDAC1 concentration obviously impeded the recognition of signals in several advanced heteronuclear NMR spectra.

Alternatively, a variety of selectively labelled samples were used to enable the assignment of HVDAC1. By this approach it was possible to assign about 56% of the sequence and, furthermore, to establish a two dimensional topology model for the last 14 β -strands of HVDAC1. Nevertheless, structural information about the remaining N-terminal part is still limited. In this region, only a few amino acids and two short β -stranded fragments between L29 and D33 and T55 and T58 could be assigned on the basis of specific HVDAC1 mutants. As confirmed by heteronuclear NOEs and a fast amide hydrogen-deuterium exchange, the assignment difficulties in this region are obviously attributed to an enhanced flexibility of the N-terminal part. The observed flexibility might partially arise from a certain instability of the detergent solubilised channel. Evidence is given by a recent study which described the observation of small folding disparities between detergent and phospholipid solubilized HVDAC1^[128] (Tab. 5-3). Compared to diC_{12:0}PC the LDAO solubilized channel exhibited less β -stranded and more α -helical structure which obviously led to a reduced stability of the protein^[128] (Tab.5-3). Since similar secondary structural proportions were also observed for HVDAC1, this might be a reason for the enhanced flexibility of the N-terminal part as observed by NMR.

Table 5-3: Analysis of HVDAC1 CD spectra.

Amphiphile	Protein	α -helix [%]	β -structure (sheet/-turn) [%]	Random coil [%]
diC _{12:0} PC* [§]	HVDAC1	9.6	62.5 (37.4/25.1)	27.9
LDAO [§]	HVDAC1	15.5	54.5 (31.5/23.0)	29.7
LDAO [#]	HVDAC1	17.0	56.0 (36.0/20.0)	27.2

[#])this study, ^{*})in accordance to ^{[128];[§])} 1,2-dilauroyl-; sn; -glycero-3-phosphocholine

Even if the N-terminal flexibility of HVDAC1 seems to be enhanced in detergent it can be assumed that the observed flexibility of the N-terminal part is, to a certain degree, an intrinsic feature of the channel protein owing to its gating properties. It has been demonstrated that a set of charged N-terminally located residues exert influence on the voltage dependency of ScVDAC1^[134]. Moreover, in ScVDAC1 nearly the same residues were further identified to influence exclusively the selectivity of the open, but not of the closed state^[43]. Since most of these residues are located within the N-terminal 84 residues of ScVDAC1 this domain is supposed to move during the gating process^[57]. A significant set of these yeast residues (D16, K19, K61) is also conserved in the sequence of HVDAC1. Moreover, D16 and K19 are highly conserved in all VDAC sequences. Due to these conservations and the similar conductance properties of all VDAC proteins, a common gating process could be assumed. A movement of the N-terminal domain, however, should require a certain flexibility of the N-terminal part such as exactly observed for the first 90 residues of HVDAC1 by NMR.

5.2.2 Determination of the global HVDAC1 architecture by X-ray crystallography

In spite of the enhanced flexibility in solution HVDAC1 exhibits a comparatively high tendency to form 3D crystals in the presence of precipitants. However, the vast majority of these crystals either did not diffract at all or only to low resolution. Medium resolutions between 3.5 and 4 Å were only observed for crystals of cymal-5 solubilised HVDAC1. Although other detergents e.g. OPOE and DDAO led to a similar crystal lattice as observed with cymal-5, these crystals only diffracted to about 8 Å resolution. Hence, this is another example which underlines the decisive influence of the detergent not only on crystal formation, but also on their quality of diffraction^[135]. One can speculate that in case of HVDAC1 the application of cymal-5 potentially suppresses the inherent flexibility of the protein. However, as it turned out by NMR this is apparently not the case. In order to improve the NMR spectra also cymal-5 was tested. Since the spectra of HVDAC1 in LDAO and cymal-5 were almost identical, a stabilising effect of cymal-5 can be excluded. Even cymal-5, at present the best observed detergent, seems not to be the optimal for the stabilisation of HVDAC1. Although the HVDAC1/Cymal-5 crystals were reliably reproducible, most of them only diffracted to a resolution between 5 and 6 Å. Nevertheless, due to a set of selenomethionine and Pt-derivatised crystals of crucial higher quality, experimental phases were determined to about 6 Å. The reliability of this solution is impressively verified by the obtained electron density which unambiguously describes barrel-like structures of the same dimensions as observed for HVDAC1 by EM^{[39][40]}.

The barrel-like structures exhibit a mean diameter of about 35 Å which is quite close to the 37 Å estimated from single particles and 2D crystals of HVDAC1^[40]. With 25 and 20 Å also the pore diameters are in the same range as observed by EM^[40]. Moreover, regarding the overall dimensions a striking similarity between the electron density of HVDAC1 and a 3D surface reconstruction of NcVDAC can be observed (Abb. 5-2).

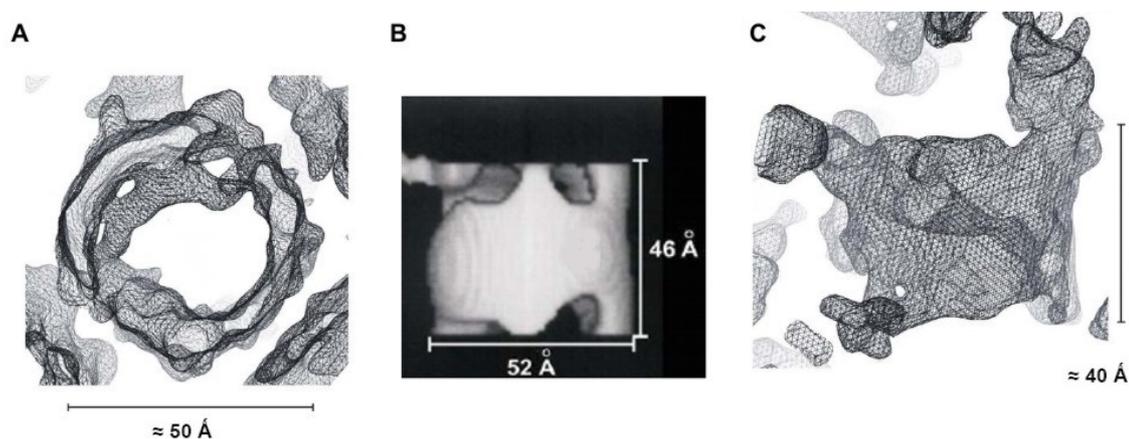


Figure 5-2: Comparison of the overall VDAC dimensions as determined by EM and X-ray crystallography.

A,C: Illustrated sections of the calculated electron density map of HVDAC1-His₆. **B:** Three dimensional surface of the *N. crassa* VDAC reconstructed from tilted EM projections (resolution ~20 Å)^[39].

In contrast to the EM observations of HVDAC1 and NcVDAC, an additional map feature is clearly identifiable in the barrel interior along one side of the channel wall. As confirmed by NMR and X-ray crystallography this density feature describes the location of the N-terminal α -helix of HVDAC1. The lumen internal location of the N-terminal α -helix poses a main difference to the EM data of NcVDAC which suggested that the N-terminal α -helix extends laterally out of the barrel lumen^[39].

As a result of the limited resolution and the poor phases the HVDAC1 density turned out to be insufficient for model tracing. Because of the lack of NCS and different crystal forms density improving techniques such as NCS- and multi crystal averaging were not applicable in this case. By contrast, *B*-factor sharpening as a new application for the improvement of low resolution maps turned out to be more successful^[107]. Although this method increases the noise level, *B*-factor sharpening resulted in electron density maps which allowed unambiguous tracing of β -strands and their tilt angles in several sections of the β -barrel wall. Hence, it becomes possible to build a closed β -barrel of 18 β -strands forming the channel wall of HVDAC1. Nevertheless, as a result of insufficient map detail individual amino acids (except for the detected selenomethionines) could still not be positioned.

5.2.3 Improved model interpretation by the integration of local and global structure information

Due to the incomplete NMR assignment and the low resolution electron density, neither NMR spectroscopy, nor X-ray crystallography allowed an entire structural description of the HVDAC1 topology. However, both methods facilitated independently of each other the achievement of novel structural information about the channel structure, each incomplete but complementary. The NMR model covers about two thirds of the whole barrel accurately and could hence be used to enable a distinct improved interpretation of the X-ray derived β -strand topology. On the basis of the obtained Se positions, the NMR information about the hydrogen bonding network allowed an assignment of individual residues in the X-ray derived β -strand model. However, the long loop which is assigned between the first two β -strands turned out to be largely inconsistent with the observable borders of the X-ray density. As in general the NMR information is relatively insecure in the N-terminal domain of HVDAC1 this part of the NMR proposed 2D-topology was disregarded during the integration of the two models. Apart from that the resulting structure complies with all given restrictions, the interstrand HN-HN NOEs, the selenium sites of M132, M158 and M230 and moreover with the borders of the X-ray density.

5.3 Structural basis of HVDAC1

The structure of HVDAC1 is composed of an 18-stranded anti-parallel β -barrel preceded by an amphiphatic α -helix. This α -helix runs almost perpendicular to the channel axis along the mid-level of the inner channel wall defined between β -strands 10 and 15. Due to the inwardly folded α -helix the lumen of HVDAC1 becomes significantly narrowed midway through the membrane. Interestingly, this topology coincides with none of the VDAC models which were developed in the past (see Chap. 2.3.7). Although the HVDAC1 structure agrees to a certain extent in some of the predicted β -stranded regions with each of these models, they considerably disagree in their entire topology (Fig.5-3). This variation mainly emerges from the positions and lengths of largely extended loops which turned out to be part of the β -stranded channel wall of HVDAC1.

The secondary chemical shift analysis, the amide proton exchanging behaviour against D_2O and the HN-HN NOE connectivities clearly demonstrate that large parts of the formerly proposed loop regions fold in fact into membrane embedded β -strands. Moreover, all of the additional assigned β -strands of HVDAC1 exhibit the amphiphatic sequence pattern which is typical for β -barrel membrane proteins (Tab. 5-4).

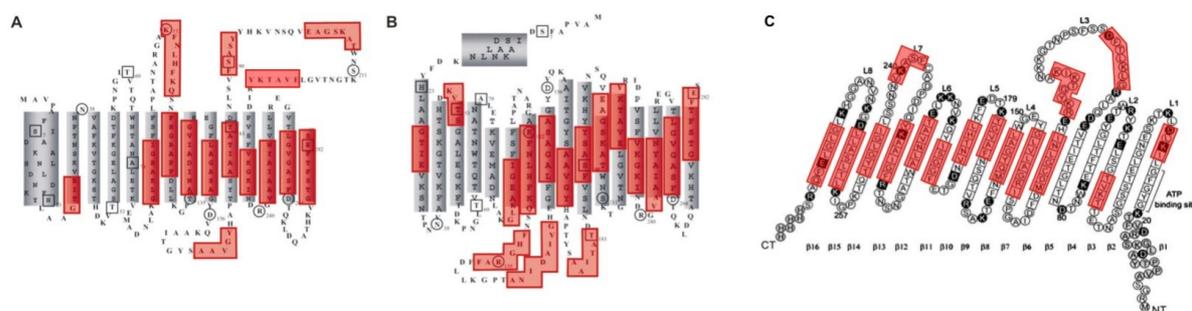


Figure 5-3: Comparison between the NMR derived topology of HVDAC1-His₆ with previous proposed VDAC models
 Superposition of identified transmembrane β -strands on the proposed topology of previously developed models. **A:** 13-stranded model of *N. crassa* VDAC1^[59]. **B:** 16-stranded model of *N. crassa* VDAC1^[136]. **C:** 16-stranded model HVDAC1. The sequence assigned positions of in HVDAC1 identified transmembrane β -strands are depicted as transparent red boxes.

Table 5-4: Amphipathic sequence pattern of NMR identified β -strands of the barrel wall which were in previously models primarily assigned to extended loop regions.

	<i>N. c.</i> 13-stranded* ^[59]	<i>N. c.</i> 16-stranded* ^[136]	human 16-stranded ^[55]
1	A K F N L H F K	F H G R A F F	G L K L T F D
2	Y S A A V G Y	A N I D A I V	K I K T G Y K
3	F S A S Y Y	A A I T A D	G L K L T F D
4	V E A G \hat{S} K A T W		
5	L E V A T K Y		

*) *N.c.* sequences which correspond by alignment to the respective β -strands of HVDAC1-His₆.

\hat{S}) Often serins were also found to reside on the outer surfaces of β -barrel membrane proteins.

Since charge altering point mutations concerning the N-terminal α -helix and the first following β -strands affect only the ion selectivity of the open state^[56], it can be assumed that the observed topology of HVDAC1 resembles the open and anion selective state. Based on its spacial orientation, the charged face of the amphipathic α -helix points passage straitened into the channel and would hence be explain its distinct influence on the open state selectivity.

Regarding the assumable interaction between the α -helix and its adjacent part of the channel a mutual stabilization is obvious. Therefore the open state conformation of the observed structure would be also in line with the fact that the channel's open state is shown to be destabilized by the truncation of the N-terminal α -helix^{[54][68]}.

However, from the observed topology, it can not be deduced if a simple rearrangement of the N-terminal α -helix or rather the removal of a transmembrane part and subsequent relocking of the remaining barrel is responsible for the transition to the low conductance state. Even if the latter seems to be quite unusual such a mechanism is still supported by the NMR observed flexibility of the α -helix and the first four β -strands.

5.3.1 The HVDAC1 architecture is common to all VDAC proteins

VDAC proteins are ubiquitously present in the outer mitochondrial membranes of all mitochondria containing organisms. When reconstituted into planar lipid membranes, the vast majority of all characterised VDAC1 homologs exhibit similar conductance selectivity and electro-physiological characteristics (see chap. 2.3.3). Moreover, EM studies of two dimensional HVDAC1^[40] and NcVDAC^[137] crystals revealed similar dimensions for both proteins. Thus, it can be suggested that these proteins also adopt a similar fold. However, across the kingdoms VDAC proteins are quite different on the level of their primary sequences. For instance, the sequences of HVDAC1 and *Triticum aestivum* (wheat) VDAC1 are similar to just about 20%. Nevertheless, both proteins exhibit comparable electro-physiological properties and are capable to complement the *Δpor1* yeast mutant^{[138][139][140]}.

5.3.1.1 The secondary structural distribution is conserved across all VDAC proteins

In order to evaluate the supposition that all of these proteins adopt the same fold as HVDAC1, a significant set of eleven metazoan, six plant and two fungal originated VDAC1 homologs were aligned (Fig. 5-4). As it turned out, all VDAC1 sequences exhibit the typical intrinsic sequence pattern of transmembrane β -strands at analog positions as verified for HVDAC1 (Fig. 5-4). The only discrepancy concerns a single residue in the fifth strand of yeast VDAC1. In this strand an Asn occupies the claimed position of an unpolar residue and, thus, breaks the rule of the strand intrinsic sequence pattern. However, an Asn residue at such a position is not further abnormal and for instance with Asn25 also observable in the structure of the bacterial transmembrane β -barrel protein OprD^[141]. Regarding the sequence gaps as a inevitable consequence of the alignment, it is noticeable that all of the inserted gaps are located in loop regions of HVDAC1 (Fig. 5-4). Furthermore, the mean tilt angle of the HVDAC1 β -strands of 45° almost exactly corresponds to the 46° of PvVDAC1 and PvVDAV2 as determined by FTIR measurements^[50].

Moreover, secondary structure predictions reveal the existence of an N-terminal α -helix in all VDAC proteins^[42]. According to the HVDAC1 structure, this region indeed folds into an α -helix and resides inside the β -barrel along one part of the channel wall. As verified by the HVDAC1 density and the NMR structural analysis of an N-terminal HVDAC1 peptide^[143], the α -helical region comprises a stretch of 15 residues (T5-K19) which are N-terminally preceded by a highly conserved Pro residue (Fig. 5-4).

Interestingly, this region is one among the most conserved areas of all VDAC proteins. Hence, it can be deduced that the corresponding regions of all other VDAC proteins also fold into an α -helical conformation. Due to the positional conservation of congeneric amino acids these α -helices are all amphipathic. According to the alignment always an Asp or Glu residue in the 4th position and a Lys or Arg residue in the 9th position point towards the same direction as the highly conserved Asp in the 11th position. The resulting [DE]-x(2)-[KR]-x(3)-D motif constructs the charged face of the amphipathic α -helices in all aligned VDAC1 homologs. On the opposite face of this charge pattern the N-terminal α -helices are consistently occupied by unpolar or hydrophobic residues, thereby establishing the amphipathic nature of the N-terminal α -helices. The channel wall area which is directly covered by the N-terminal α -helix resides mid level along β -strands 10 to 14 (Fig 5-4). At the level of the α -helix the channel lining contains no charged residues but is otherwise rather polar than hydrophobic. Nevertheless, in close proximity to the center of the α -helix a Tyr or Phe residue of β -strand 12 is highly conserved in all VDAC proteins and is certainly involved in the structural stabilisation of the N-terminal α -helix (Fig 5-4).

5.3.1.2 The HVDAC1 structure in respect to the effects of charge altering point mutations

Due to its position the N-terminal α -helix constitutes the central element in the channel. Hence, the extensive conservation of this region is not surprising and most likely co-responsible for the common selectivity properties of all VDAC1 proteins. In fact, it was shown that the open state selectivity of ScVDAC1 alters upon mutation of the highly conserved Asp residue in the 11th position of the α -helix^[56]. Such selectivity changes were also shown upon mutation of a further highly conserved Lys residue at the beginning of the α -helix connecting linker as well as for a set of predominantly positive charged residues along the pore lining^[56]. Even if the latter are not conserved, they are exclusively located in pore delimiting regions (Fig. 5-4).

By contrast, the vast majority of all mutations which left the selectivity of ScVDAC1 unaffected, are either located in loops or in the α -helix shielded wall segment (Fig.5-4). Within the region which is shielded by the N-terminal α -helix, there are only two residues, one in β -strand 11 and one in β -strand 15, which nevertheless influence the open state selectivity of ScVDAC1 upon mutation (Fig. 5-4). However, according to the HVDAC1 structure both are in intimate vicinity of the N-terminal α -helix. Due to their position a certain influence on the α -helix can be deduced and sufficiently explains the observed selectivity changes upon mutation.

5.3.1.3 VDAC proteins exhibit a positively charged channel lining

Assuming that all VDAC proteins adopt the same topology as HVDAC1, two further three-dimensional models of a plant VDAC (*T. aestivum* isoform1) and a fungal VDAC (*N. crassa*) were generated. The models thereby obtained, consistently exhibit a continuously unpolar outer surface (Fig. 5-5). While that is expected for an integral membrane protein, it is noticeable that in spite of low sequence similarity, all of them also coincide in a positive surface potential along the pore lining (Fig. 5-5). The positive potential expands in consequence the overall pass-through for anions and at the same restricts time the cation accessible lumen due to repulsion forces. This might be the reason for the slightly enhanced anion selectivity of all VDAC1 homologs in the open state.

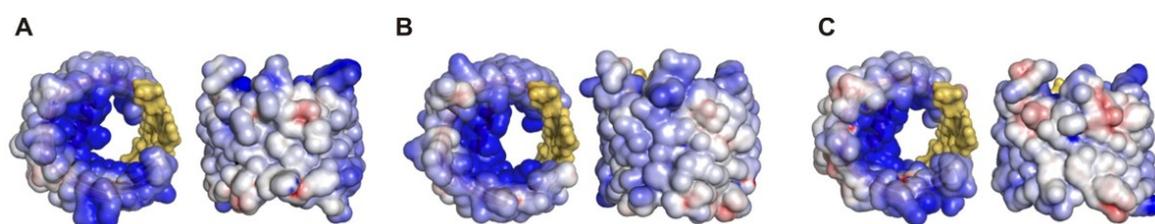


Figure 5-5: Generated models of different VDAC1 homologs.

Models of the VDAC1 homologs from *A. thaliana* (B) and *N. crassa* (C) were generated on the basis of the HVDAC1 structure (A).

5.3.1.4 A conserved indentation pattern is characteristic of all VDAC proteins

The 3D surface reconstruction of NcVDAC describes three large indentations on one side of the barrel edge^[39]. Two of them are in close vicinity to each other and solely separated by a narrow rise, a third one resides in the wall oppositely to this rise (Fig. 5-6A). In almost the same manner the characteristic pattern of the first two indentations is also detectable on the surface of HVDAC1 (Fig. 5-6B,C).

The indentations of both VDAC structures are of the same size and in both one is broader and less indented while the second is narrower and of a deeper indent (Fig. 5-6A,B). Hence, the characteristic indentation pattern corroborates the assumption that HVDAC1 and NcVDAC adopt a concurrent topology. The congruent appearance of the characteristic indentation pattern at the β -barrel edges of both proteins enable the unambiguous integration of the HVDAC1 structure and the EM model of NcVDAC. According to the derived orientation, the third indentation of NcVDAC resides in the in the region of the first four N-terminal β -strands (Fig 5-6 A,B).

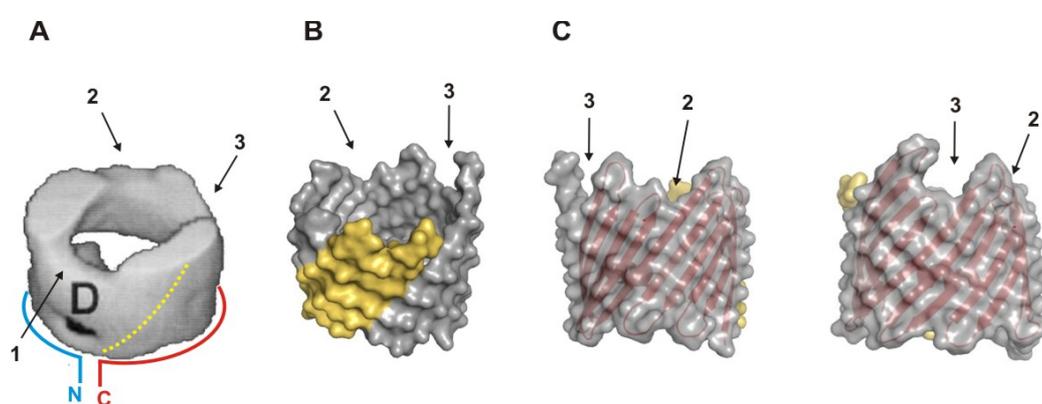


Figure 5-6: Characteristic surface indentations of HVDAC1 and NcVDAC.

The generated surface of HVDAC1 (B,C) exhibit a similar indentation pattern as observed in EM reconstructions of NcVDAC (A). (A) EM surface of NcVDAC reconstructed from tilted crystal projections^[39]. Two of the indentations are in close vicinity (2, 3), a third indentation (1) is recognisable oppositely of the rise separating the adjacent two. The position of the barrel closure is illustrated in accordance with the corresponding position in the X-ray derived model of HVDAC1. The unassigned region of the β -barrel is marked in yellow. (B,C). Surface of HVDAC1. The characteristic grooves are labelled in accordance to the EM surface.

In HVDAC1 the two characteristic notches between β -strands 9 and 18 emerge from two shortened pairs of β -strands (β 11, β 12; β 15, β 16) which each are adjacent by longer β -sheets (β 9, β 10; β 13, β 14; β 17, β 18) (Fig 5-5B,C). With regard to the distribution of β -strands and their connecting loops, the alignment in the corresponding region is highly consistent to all VDAC proteins (Fig 5-4).

Therefore, the characteristic indentation pattern is a highly conserved feature of all VDAC proteins and might play role for the oriented docking of cytoplasmic kinases and other VDAC interacting proteins.

5.3.2 HVDAC1 reveals a common β -barrel fold

In the past, the structures of numerous bacterial β -barrel membrane proteins led to the establishment of a set of common rules^[47] which predominantly seem to be equally valid for HVDAC1. Also in HVDAC1 the β -barrel consists of an even number of anti-parallel β -strands which are consecutively linked by loops in an all next neighbourhood conformation.

5.3.2.1 HVDAC1 retains the sidedness of bacterial β -barrel membrane proteins

Regarding the loops, all bacterial β -barrel membrane proteins exhibit long loops on the extracellular and short loops or beta turns on the periplasmic side of the membrane. This asymmetric length distribution is as well distinctive to HVDAC1. However, due to the current ambiguity about the direction in which VDAC inserts into the mitochondrial outer membrane it can not be revealed if the longer loops face the mitochondrial intermembrane space or the cytoplasm. When reconstituted into artificial membranes NcVDAC was found to insert in random orientation^[144]. Also in 2D crystals of HVDAC1 always two HVDAC1 monomers in both orientation were detected^[40]. In terms of the natural orientation of the channel in the outer mitochondrial membrane several studies were addressed to evaluate the spatial position of the N-terminal α -helix by antibodies directed against this epitope. But depending on the study, the N-terminal α -helix was proposed to reside on the cytoplasmic surface^{[136][62][67][43]} as well as on the IMS surface^{[19][145]} of the outer membrane. As it turned out the N-terminal α -helix is deeply buried in the channel interior and hence the α -helix might be already an inadequate target to address the question of the channel's orientation in the outer mitochondrial membrane. Nevertheless, according to the endosymbiotic theory it is quite likely that the longer loops of the HVDAC1 face to the cytoplasmic side of the outer mitochondrial membrane. This assumption would be also consistent with the observation which was made with an antibody directed against the C-terminal end of NcVDAC whereupon the C-terminus was assigned to the IMS side of the mitochondrial outer membrane^[145].

5.3.2.2 HVDAC1 conserves the spatial distribution of specific amino acids along the surface

Bacterial β -barrel membrane proteins reveal a preferential occurrence of certain amino acid classes in spatial regions. Along the membrane normal five spatial regions were defined^[146] (Fig. 5-7). These are the core domain and the extracellular and periplasmic adjoined headgroups and cap regions, respectively.

Within the core domain of HVDAC1, all of the individual β -strands exhibit the intrinsic sequence pattern typical for transmembrane β -barrel proteins. Parallel to the bacterial β -barrel membrane proteins, this pattern generates a nonpolar ribbon at the outer surface which covers the ambient membrane interior. Concurrently, the pattern creates a polar and in HVDAC1 a predominantly positively charged channel lining. However, with about 15 Å the hydrophobic ribbon around the β -barrel is relatively narrow compared to the hydrophobic thickness of bacterial β -barrel membrane proteins which averages 23 Å^[147].

The headgroup regions of HVDAC1 contain a noticeable accumulation of aromatic residues which is a distinctive feature of all known membrane proteins and referred to as aromatic girdle. Out of all possible aromatic residues within the 14 assigned β -strands of HVDAC1 five of seven Tyr, nine of ten Phe and all Trp residues reside in the two headgroup regions (Fig 5-7A). The unassigned part of the HVDAC1 sequence further contains two Trp, two Tyr and two Phe residues. In all probability some of them should also be located in one of the two headgroup regions in order to stabilise the remaining four transmembrane β -strands.

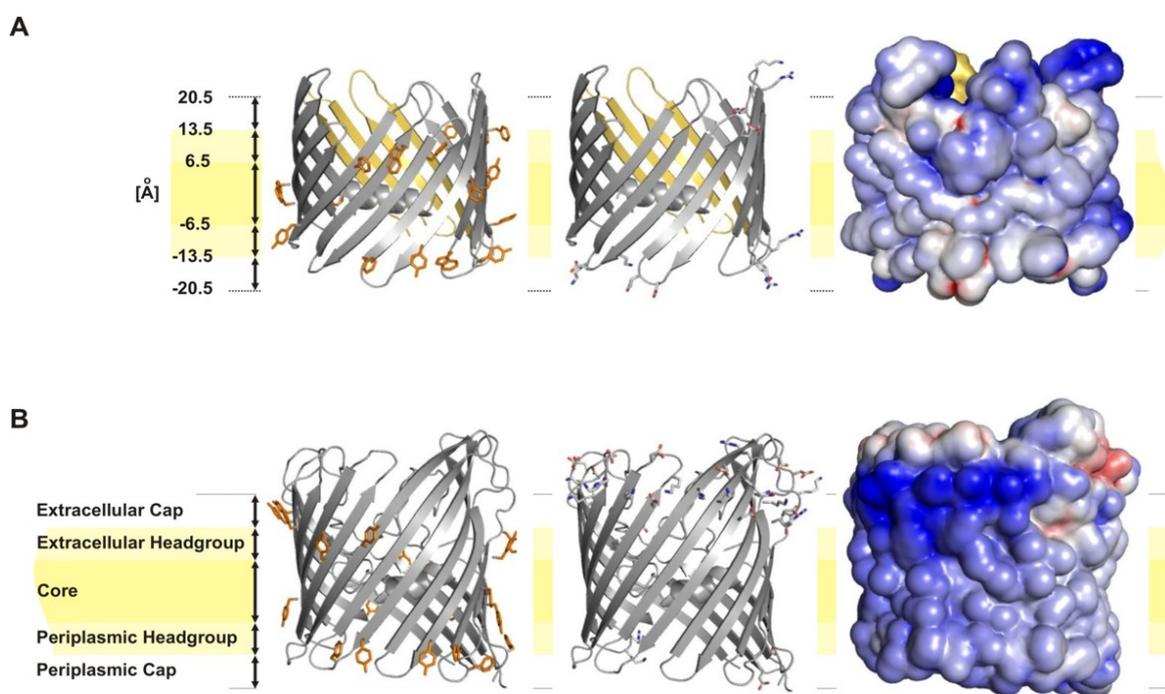


Figure 5-7: Residue specific distribution of HVDAC1 and OMP32.

Based on the preferred locations of the individual amino acid types on the outer surface of common β -barrel proteins five spatial regions were defined along the membrane normal^[146]. **(A)** HVDAC1 residue specific distribution of aromatic (left) and charged (middle) residues. **(B)** OMP32 residue specific distribution of aromatic (left) and charged (middle) residues.

In comparison, OMP32 reveals one of two Trp, nine of sixteen Tyr and eight of seventeen Phe residues in the two headgroup regions (Fig. 5-4B). In HVDAC1 as well as in Omp32 the remaining aromatic residues reside either at the inner surface or in loop regions, but not at the outer surface of the core region.

Concerning the headgroup regions also in HVDAC1 all Tyr residues are restricted to the C-terminal end of the individual β -strands. However, regarding the spatial preference of the aromatic residues, a distinct difference could be observed. Remarkably, all of the Tyr residues reside in the headgroup region of the short loops and β -turns of HVDAC1. In most of the bacterial relatives, by contrast, they exist in both headgroup regions. Phe residues on the other hand show a preference for the periplasmic headgroup region in bacterial β -barrel membrane proteins, but predominantly exist on the side of the longer loops in HVDAC1. Furthermore, bacterial β -barrel membrane proteins exhibit a second ring of predominantly positive charged residues next to the extracellular headgroup region (Fig 5-7B). This second ring obviously interacts with the negatively charged lipopolysaccharide headgroups on the extracellular surface of the outer bacterial membrane. HVDAC1 by contrast, lacks such a strongly charged region on the corresponding side of the longer loops (Fig.5-7A). In fact, this barrel edge of HVDAC1 is rather uncharged and contains only a few predominant positively charged residues. A slightly higher distribution of predominantly negative charged residues can be observed on the opposite edge of HVDAC1, but also this side is rather uncharged. Solely at the inner barrel wall and along the N-terminal α -helix of HVDAC1 a larger distribution of predominantly positive charged residues is detectable.

5.3.2.3 HVDAC1 is specifically adapted to the outer mitochondrial membrane

According to the observable similarities, the HVDAC1 structure largely coincides with the known construction principle of bacterial β -barrel membrane proteins. The emerging differences concern the site-specific distribution of the Phe and Tyr residues as well as the lack of a positively charged moiety on the side of the longer loops. Furthermore, compared to bacterial β -barrel membrane proteins, HVDAC1 exhibits a smaller hydrophobic thickness and moreover a smaller height overall. Both features are attributed to the average length of the HVDAC1 β -strands. Although HVDAC1 and for instance OMP32 exhibit similar average tilt angles of 45° and 43° ^[47] the average β -strand lengths are quite different with about 9 and 12.6^[47] residues, respectively. Together with the in general short loops of HVDAC1 this results in a channel height lower than observed for Omp32 and other bacterial β -barrel membrane proteins.

All of these differences might be attributed to a differing membrane composition and probably also to a smaller membrane thickness of the mitochondrial outer membrane to which HVDAC1 is specifically adapted to.

5.3.3 The structural design of HVDAC1 is reminiscent of the bacterial porin architecture

Interestingly, the topology of HVDAC1 is reminiscent of the common porin architecture (Fig. 5-8). Porins like OmpC or Omp32 are bacterial membrane proteins which mediate like VDAC an exchange of small molecules across the outer membrane^[49]. Bacterial porins are composed of 16- or 18-stranded β -barrels and an α -helical structure which resides in a position such as observed for HVDAC1. Due to the position, the α -helix effects a significant pore constriction and accounts for the selectivity characteristics of this membrane protein type. However, unlike HVDAC1, the α -helix of the porins is part of a long inward folded domain which in all porins arise from the third extracellular loop L3^[49]. Nevertheless, the position and the influence of the α -helix onto the overall barrel architecture of HVDAC1 is reminiscent of the L3 loop present in bacterial porins. Therefore, this structural design seems to be a hallmark feature of metabolite guiding outer membrane proteins.

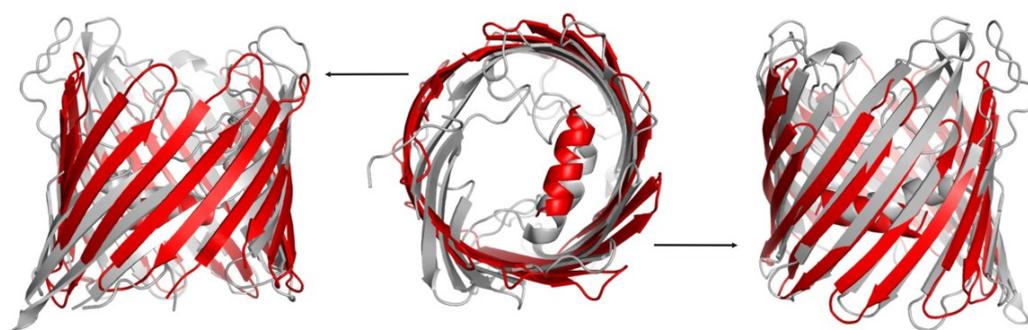


Figure 5-8: Superposition of HVDAC1 and Omp32

The global architecture of HVDAC1 is reminiscent of Omp32. HVDAC1 (red), Omp32^[148] (grey). Superposition was carried out in COOT^[110].

An N-terminally elongated β -barrel, as observed for HVDAC1, is not exceptional for β -barrel membrane proteins. Apart from the porins many other bacterial β -barrel membrane proteins accomplish pore restrictions by N-terminal domains.

All of them belong to a class of outer membrane transport proteins such as the metal transporter FhuA^[149], the autotransporter NalP^[150] or FhaC^[151] which belongs to the Omp85 like two-partner secretion system. However, the geometry of these domains is more complex and not comparable to HVDAC1. A similar combination between an N-terminal α -helix and a β -barrel is otherwise only observable for PagP^{[152][132]}, an outer membrane acyltransferase which is involved in endotoxin synthesis^[152]. But unlike observed for HVDAC1, the N-terminal α -helix of this enzyme resides outside the β -barrel in the periplasmic space and does not fulfill a pore restricting function.

5.3.4 The alternative pore restriction seems to be attributed to the voltage dependent behavior

Although the HVDAC1 topology is reminiscent of the bacterial porins, HVDAC1 is restricted by an N-terminal extension as seen in bacterial outer membrane transporters and not by L3 as seen in functionally related porins. This difference in topology might be attributed to the reversible conductance and selectivity states which VDAC proteins are capable to undergo in a voltage dependent manner. Voltage-controlled conductivity and selectivity alterations of porins reconstituted in lipid bilayers are also known^[153], however, the induction of such changes requires about three to fivefold increased voltages compared to VDAC. OmpF for instance, was shown to exhibit a slightly cation selective open state which changed to a closed conformation at a membrane potential of about 150 mV^[154]. VDAC proteins, by contrast, exhibit no closure, but a conductance reduction of about 50% already takes place in response to potentials in a range of about 30 mV (ScVDAC) and 50 mV (HVDAC1), respectively (Tab. 5-2). Even if they do not close completely the reduction from about 4 to 2 nS is dramatic with respect to OmpF which just reveals an open state conductance of approximately 0.8 nS. In case of OmpF, it turned out that channel closure is not an issue of L3 movement, but rather the result of multiple positional changes of fixed charges along the pore lining^[154]. To a certain extent this might also apply to VDAC since in ScVDAC1 some of the voltage sensitivity and conductance altering point mutations were found to reside in β -strands of the pore forming channel wall^[57]. Nevertheless, most of them are located within the first 84 residues of ScVDAC1 and therefore in the region which is supposed to move during voltage induced conductance alteration^[57]. Except for the N-terminal α -helix the corresponding ScVDAC1 residues are not definitely assignable to the HVDAC1 structure, but nevertheless it is already clear that these residues reside within the first four β -strands of the barrel wall.

Since, compared to OmpF, relatively small voltages are already sufficient to induce the supposed structural alterations and, thus, the conductance state of VDAC a certain flexibility of the N-terminal domain must be assumed.

Therefore, it seems that in contrast to the L3 loop the alternative pore restriction by an N-terminal α -helix provides the relatively rigid construction principle of a β -barrel membrane protein with the required flexibility as necessary for the conductance alterations in VDAC proteins. Moreover, the functional replacement of L3 by a relative small N-terminal α -helix reduces the amount of substantial and potentially stabilizing protein domains in the barrel interior for the benefit of an enhanced flexibility.

5.3.5 HVDAC1 exhibits a comparatively large pore diameter

Furthermore, the N-terminal α -helix and its potential linker restrict the pore of HVDAC1 to a lower extent than the L3 loops in bacterial porins of comparable size. Bacterial porins, like Omp32 and OmpF, exhibit relatively small pore diameters of $5 \times 7 \text{ \AA}$ and $7 \times 11 \text{ \AA}$, respectively. Also 18-stranded porins, like the sucrose porin^[155], show a barely larger or in case of the maltoporin^[156] even a smaller pore size than the 16-stranded OmpF. By contrast, HVDAC1 exhibits an unusual large pore diameter due to the pore restriction by its comparatively small N-terminal domain. Although the exact pore boundary of HVDAC1 can not be defined in the present model, it can be pre-estimated that the passage of HVDAC1 exceeds at least three to four fold the pore size of OmpF (Fig.5-9). Since a large part of the vast pore is solely bordered by a comparatively thin channel wall which is otherwise not further stabilised by internal domains like the L3 loop this might be a further issue for the enhanced flexibility of HVDAC1.

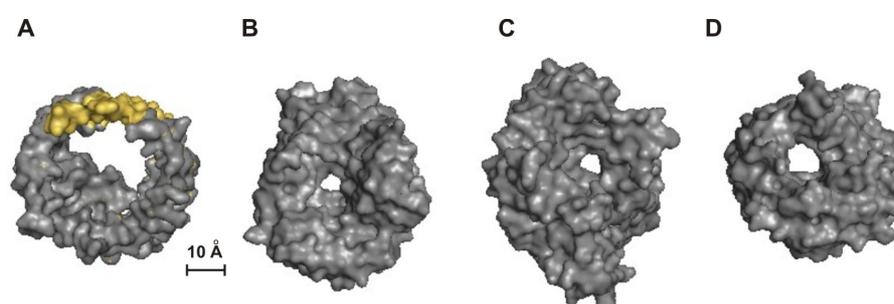


Figure 5-9: Pore diameter of HVDCA1 and different bacterial porins.

A: HVDAC1 (18 strands). Residues in the unassigned region (yellow) are represented by alanine residues. B: Omp32 (16 strands) C: MalA (18 strands) D: OmpF (16 strands).

5.3.6 Oligomeric structure of HVDAC1

Bacterial porins are known to form remarkably detergent and protease stable homotrimers^[157]. By contrast, oligomeric complexes of similar stability are not observable for VDAC proteins. However, at least in detergent also VDAC proteins are supposed to form dynamic oligomers. Evidence for multiple oligomeric states of HVDAC1 were deduced from crosslinking^{[117][158]} and FRET^[158] studies. In these studies HVDAC1 could be observed in dimeric, trimeric and tetrameric states in detergent^{[117][158]}. Moreover, chemical cross-linking of rat VDAC in isolated rat liver mitochondria let assume that in the outer mitochondrial membrane predominantly the dimeric, but also trimeric and tetrameric states exist^[158]. Potential dimers of HVDAC1 were also observed in the unit cell of two dimensional HVDAC1 crystals^[40]. But since the two monomers lack any twofold symmetry, it was assumed that the two HVDAC1 molecules are inserted in opposite directions^[40]. Nevertheless, it seems that HVDAC1 tends to form oligomeric complexes of variable extent. However, while the existence of such oligomers is frequently mentioned, their structural basis is still unknown.

5.3.6.1 HVDAC1 dimerises via the β -barrel junction

By chemical and light induced cross-linking HVDAC1 dimers were also observed in this study. Remarkably, upon Bid or cBid addition these dimers were observed to a much lesser extent. Therefore, it is quite likely that at least one of the dimerisation sites resides close to the interaction site of Bid and cBid. Interestingly, in HVDAC1 crystals one of the crystal contacts is accomplished across the β -barrel junctions of two HVDAC1 monomers which are related by a twofold symmetry axis (Fig. 5-3A,F). Concerning their channel axes, the connected barrels are equally orientated and hence the resulting dimer might emerge in the outer mitochondrial membrane as well. Around the β -barrel junctions of both monomers, this interaction is mediated by at least three contact sides (Fig. 5-3D,F). Along a vertical line, two of them reside at the opposite β -barrel edges, another one takes place halfway between them (Fig. 5-10D). Out of the three contact sites, two belong to the C-terminal parts of each HVDAC1 monomer. Both of them reveal a hydrophobic nature and involve the residues L254 (L3), I258 (β 17) and L260 (β 17) at one of the barrels edges and the residues I280 (β 18) and I282 (β 18) at the central interaction site (Fig. 5-10D,F,G). The remaining interaction takes place between the first N-terminal β -strands (β 1) and, because of the position at the β -barrel edge, most probably also between the first loops (L1) (Fig 5-10D,F,E). Due to the lack of assignment in this region, the molecular nature of this interaction can not be revealed.

However, the fact that the dimer persists in mild detergent solutions suggests that also electrostatic interactions play a role. Since electrostatic interactions between the C-terminal parts are absent, it is most likely that at least one of the N-terminal interactions is of electrostatic nature.

Interestingly, the detected dimerisation site resides in immediate vicinity to the NMR confirmed interaction sites of Bid and cBid (Fig. 5-10F). Hence, binding of one of these proteins certainly interferes with the dimerisation of HVDAC1. Consequently, in presence of Bid or cBid HVDAC1 dimerisation should be abolished and this is exactly what was observed by chemical and light induced cross-linking. Therefore, one can conclude that the dimers observed in the crystal exist as well in low concentrated HVDAC1 solutions and putatively also in the outer mitochondrial membrane. Thus, the determined interaction site at the β -barrel junction of HVDAC1 should be authentic and of physiological relevance with regard to the interactions between HVDAC1 Bid, Bcl-XL and HK II.

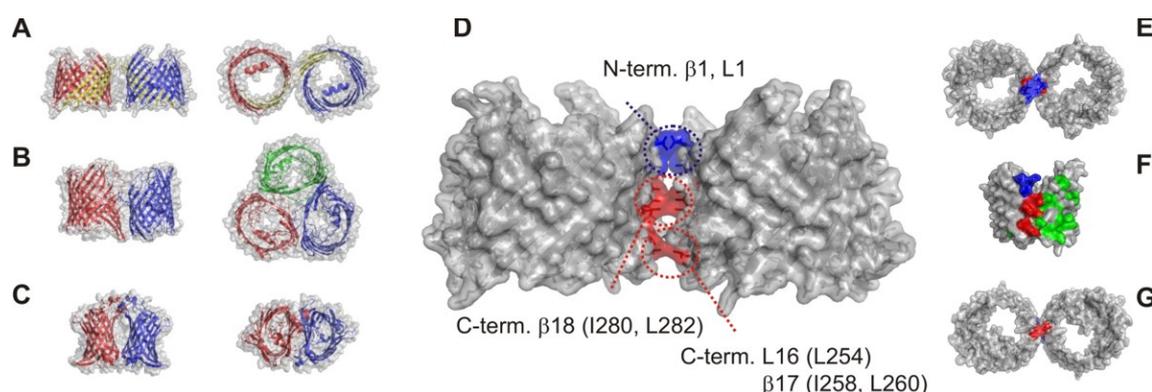


Figure 5-10: HVDAC1 dimerisation.

One of the contact sites in HVDAC1 crystals is accomplished across the β -barrel junctions of two HVDAC1 monomers related by twofold symmetry. **A**, HVDAC1 dimer as observed in the crystal. **B**, Omp32 trimer. **C**, OmpLA dimer. **D**, HVDAC1 contact site in a side view and **E**, **G**, from the two top sites along the channel axis. **F**, involved interaction area at the β -barrel junction of HVDAC1. Blue, N-terminal located interaction site. Red, C-terminal located interaction sites. Green, Bid interaction site on HVDAC1.

5.3.6.2 Implications on the stability of HVDAC1

While in trimeric porins and in the dimeric phospholipase OmpLA the β -barrels are remarkably flattened at the interactions sites, this is not the case at the dimerisation site of HVDAC1 (Fig. 5-10A-C).

Due to this flattening, the interaction sites of the bacterial multimers are considerably enlarged compared to HVDAC1 and consequently cause the observed stability of their oligomeric structure. The circular form of HVDAC1, by contrast, allows only a narrow band of interaction along the channel normal. This reduced area should cause a rather weak interaction between the monomers and hence might be the reason for the dynamic equilibrium between monomeric and dimeric forms of HVDAC1.

Since the β -barrel junctions of both HVDAC1 monomers are involved in this interaction, the as flexible determined N-terminal part of HVDAC1 should become stabilised by this dimerisation. In all probability, this dimer led to the successful crystallisation of the protein in a low concentrated detergent environment. For NMR studies, the protein had to be kept in a 30-fold higher concentrated detergent solution. Since dimer formation mainly bases on hydrophobic contacts, which might be disrupted by the high detergent concentration, the β -barrel junction of HVDAC1 became destabilised and led to the observed flexibility of the N-terminal part especially at elevated temperatures as necessary for NMR measurements.

5.4 Interaction between VDAC1 pro- and anti-apoptotic proteins and hexokinase II

Beyond the pore function, VDAC proteins are described to play an important role in the communication between mitochondria and the cell^[25]. In this context, VDAC proteins are involved via several complexes in the energy maintenance of the cytosol and the mitochondrial phase of apoptosis (see Chap. 2.3.8). Regarding the latter, particularly the interplay between the channel, cytoplasmic hexokinases and pro- and anti-apoptotic proteins like Bid and Bcl-XL turn out to be critical for the survival/death decision of the cell. Ultimate target in this decision is a set of inevitably cell death promoting factors which are retained by the outer mitochondrial membrane. Thus, the regulative purpose of this interplay is to enforce or to antagonize the factor-releasing perturbations of the outer mitochondrial membrane. Bid, for instance, targets upon proteolytic activation the outer mitochondrial membrane and induces the release of further apoptogenic factors. That Bid and VDAC interact during this process derives from the observation that a truncated version of Bid is capable to induce the closure of the channel^[81]. Channel closure reduces significantly the permeability of the outer membrane^[60] and is assumed to lead, if persistent, to the breakdown of mitochondrial homeostasis and outer membrane integrity^[159]. Interestingly, this can be averted by Bcl-XL, an anti-apoptotic protein which is shown to keep VDAC in its open configuration^{[159][82]}.

Moreover, in cancer cell lines, it turned out that the interaction between hexokinases (HK-1, HK-2) and the outer mitochondrial membrane does not only satisfy the increased energy needs of the cell but also effectively antagonizes apoptosis, thereby suppressing cell death^{[160][161]}. Both hexokinase isoforms were shown to interact with VDAC via a 15 amino acid long sequence at their N-terminal end^[162] and prevent PTPC opening upon interaction^[163]. However, while the interplay between VDAC and these proteins as well as the subsequent effects are demonstrated the molecular nature of these interactions is quite unresolved so far.

Regarding Bcl-XL and VDAC, a recent NMR study reported that the membrane inserted hairpin motif of Bcl-XL contributes significantly to the direct interaction between the two proteins^[117]. The involved parts of VDAC, though, remained unclear due to unassigned chemical shift changes. However, taking advantage of the partially assigned HVDAC1 spectrum the determination of a specific Bcl-XL interaction site could be established on HVDAC1. Based on the transfer of the most distinctive shift changes, Bcl-XL primarily interacts intra-membranally with the channel wall region around the conserved mitochondrial porin signature pattern PS00558^[142] (Fig. 5-13).

5.4.1 The signature pattern forms the structural scaffold for MOM targeting proteins

Besides the N-terminal α -helix, this pattern is highly significant for VDAC and allows with minor exceptions the reliable detection of this channel in a large number of different eukaryotic genomes. The region of the signature pattern encompasses the C-terminal fifth of the 14th β -strand, the whole 15th β -strand and the N-terminal two thirds of the 16th β -strand (Fig. 5-11A,B).

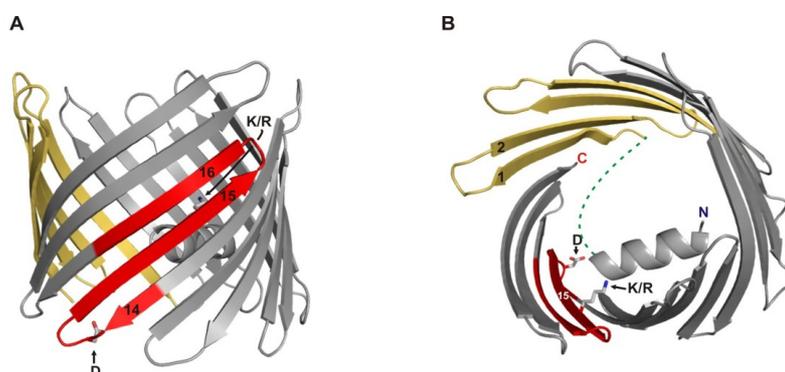


Figure 5-11: Structural position of the PROSITE signature pattern.

The location of the eukaryotic mitochondrial porin signature pattern in between strand 14 and 16 is highlighted in red. Arrows refer to the highly conserved D and K/R position in the PROSITE pattern. ([YH]-x(2)-D-[SPCAD]-x-[STA]-x(3)-[TAG]-[KR]-[LIVMF]-[DNSTA]-[DNS]-x(4)-[GSTAN]-[LIVMA]-x-[LIVMY])

Since the 15th and 16th β -strand are shorter than the adjacent β -strand, this pattern causes one of the structurally conserved barrel edge indentations. Two residues of this pattern are largely conserved. One is the highly conserved Asp residue in the loop between β -strands 14 and 15, the other is an inward facing Lys or Arg residue in the C-terminal part of β -strand 15. With regard to the barrel lumen the signature pattern resides in close vicinity to the contact site between the C-terminal end of the N-terminal helix and its barrel connecting linker (Fig. 5-11B).

Interestingly, the Bid induced shift changes in the HVDAC spectrum almost reveal the identical region as predominantly affected by Bcl-XL (Fig. 5-13). Apart from the extent of affected residues, their areal distribution indicate that both antagonists interact intra-membranal with an identical region of HVDAC1 - the region around the conserved PROSITE signature pattern (Fig. 5-13). The evolutionary conservation of the VDAC signature pattern is, hence, owed to the interaction between the channel and pro- and anti-apoptotic proteins like Bid and Bcl-XL. Moreover, these findings indicate on a structural basis that VDAC serves as a specific receptor for these pro- and anti-apoptotic proteins. However, this receptor function can not be transferred to all other members of the Bcl-2 homology family since several other members of this family are shown to permeabilise independently of VDAC the outer mitochondrial membrane, for instance by the formation of large autonomous pores^[164].

Moreover, the interaction between HVDAC1 and hexokinase II (HK II) was probed by the utilisation of a synthetic peptide which resembles the N-terminal 15 residues of HK II. This peptide is highly hydrophobic and predicted to form a transmembrane α -helix which inserts into the mitochondrial outer membrane^[165]. Interestingly, the interaction site of the HK II peptide on HVDAC1 resides again in the C-terminal region between β -strands 14 and 17 and overlaps noteworthy with the Bid and Bcl-XL interaction sites (Fig. 5-13). Therefore, the structural scaffold around the evolutionary conserved Ps00558 pattern not only offers the docking of apoptotic proteins, but also of HK II and most probably HK I to the outer mitochondrial membrane. Since the existence of a unique binding site inevitably led to steric competition between cell death suppressing (HK II, Bcl-XL) and cell death promoting (Bid) proteins, this finding gives a structural explanation for the observation that upregulation of HK II and Bcl-XL as often observed in tumors effectively protects from MOMP and consequently from apoptosis^[166].

5.4.2 Bid and Bcl-XL target the porin signature pattern via an α -helical hairpin motif

The fact that Bid and Bcl-XL target the identical binding site on HVDAC1 could not be expected at first sight due to their low sequence similarity (Fig. 5-12).

However, in spite of their low sequence similarity, Bid and Bcl-XL belong to the same structural class and exhibit quite similar folds in their soluble conformation^[167] (Fig. 5-12). The central element of these proteins consists of a hydrophobic α -helical hairpin motif surrounded by five (Bcl-XL) or six (Bid) amphiphatic α -helices^{[118][167][168]} (Fig. 5-12). Several studies proposed that binding to the membrane surface promotes the insertion of these α -helical hairpin motifs into the outer mitochondrial membrane^{[169][170][171][172]}.

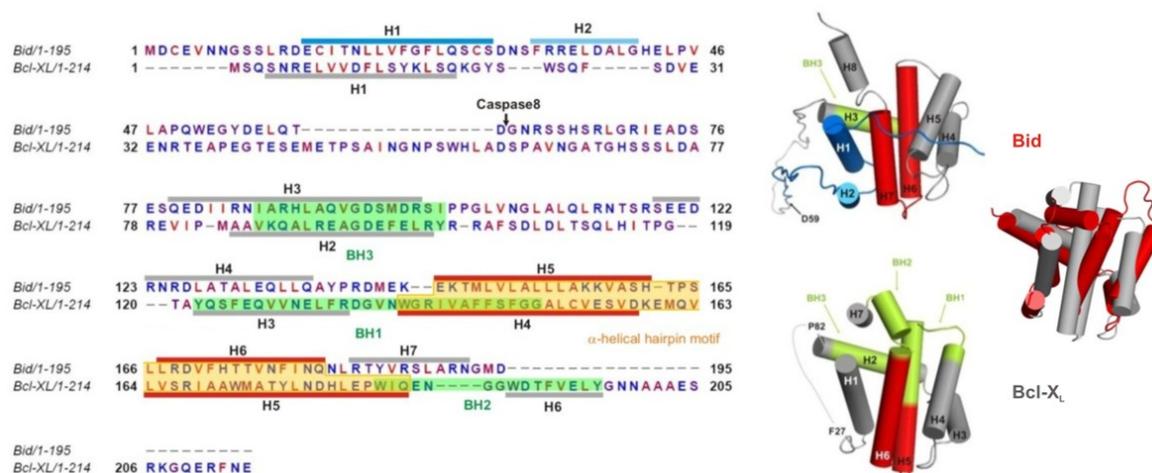


Figure 5-12: Similar fold of the Bcl-2 family members Bid and Bcl-XL.

A Rmsds of 4.90 Å over 69 residues and seven helices^[167] is indicative for a common structural fold of both proteins in their soluble conformation in spite of low sequence similarity.

In fact, the assumed insertion of the α -helical hairpin motifs provides the structural basis for the inter-membranal interaction between the PROSITE signature pattern of HVDAC1 and Bid or Bcl-XL. This is clearly demonstrated by two peptides designed to mimic the α -helical hairpin motifs of Bid and Bcl-XL, respectively. Both peptides primarily affected the N-terminal region of the PROSITE pattern around the highly conserved Asp 231 and therefore they reveal this region of HVDAC1 as a general anchoring point for Bid and Bcl-XL in the outer mitochondrial membrane. However, due to the fact that the as crucial considered Bcl-2 homology domains of Bid and Bcl-XL are not involved in the interaction with the PROSITE pattern, it is rather unlikely that the observed interaction alone is sufficient for the opposite influence of the two antagonists on the integrity of the outer mitochondrial membrane. Nevertheless, the observed interaction might certainly function as a structural basis for further processes which finally control the permeability of the outer mitochondrial membrane. As such, the verified interaction might have a complex-stabilizing function as well as an influence on the targeting and the membrane insertion of Bid and Bcl-XL.

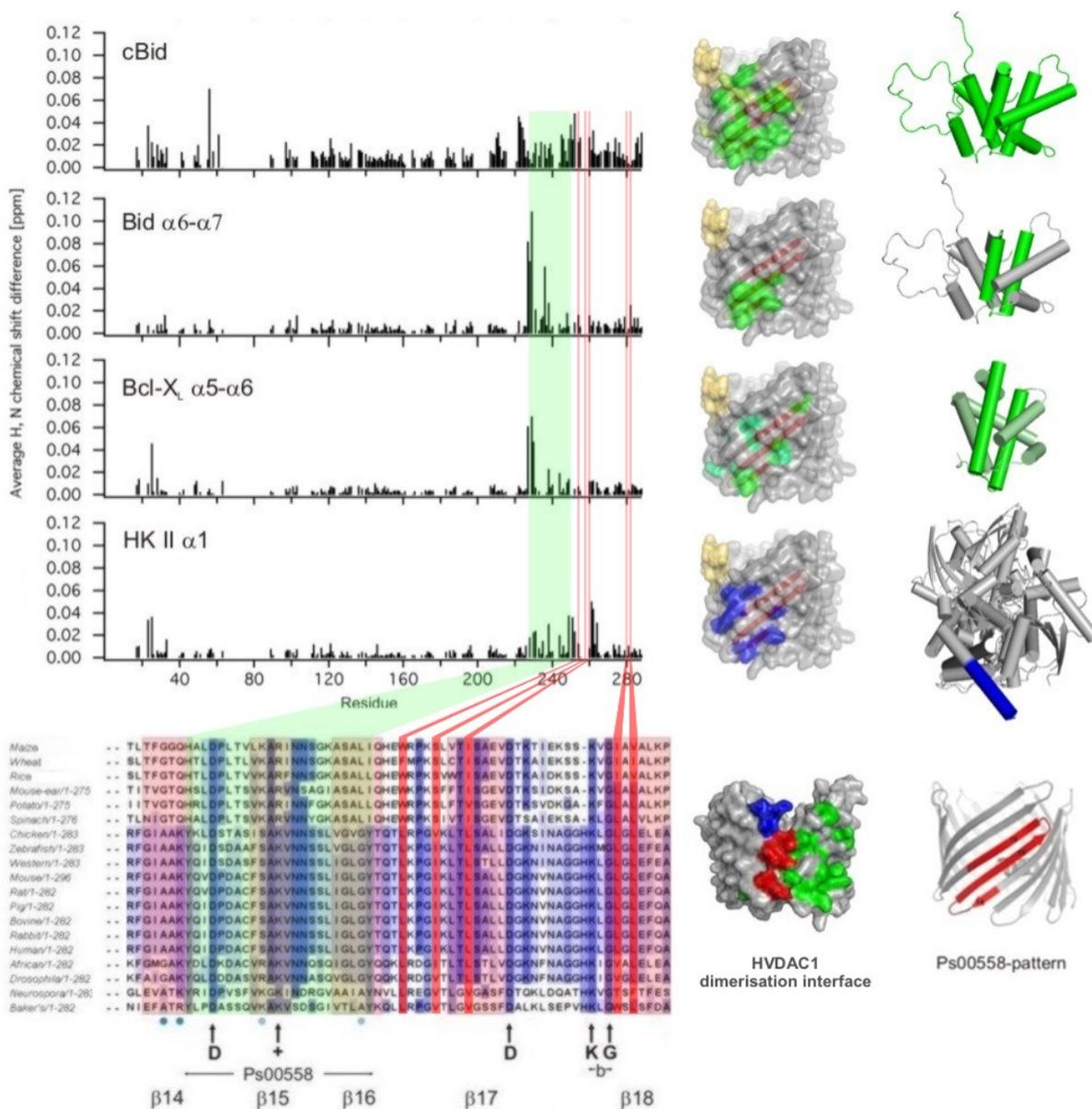


Figure 5-13: The inter-membranal interaction sites between HVDAC1, Bid, Bcl-XL and hexokinase II.

Normalised weighted average ¹H/¹⁵N chemical shift changes observed in ²H/¹⁵N-labeled HVDAC1 spectra upon addition of cBid, a Bid peptide comprising helices 6 and 7, a Bcl-XL peptide comprising helices 5 and 6 and a peptide comprising the 15 N-terminal amino acids of hexokinase II. The chemical shift changes are plotted against the aligned C-terminal regions of several VDAC sequences. Remarkably, all interaction partners induced overlapping shift changes in the region of the mitochondrial porin signature pattern PS00558^[142] (highlighted in green). Residues which exhibit shift changes > 0.015 ppm are consequently highlighted on the HVDAC1 surface (cBid, Bid and Bcl-XL peptides green; HK II peptide blue). In case of Bcl-XL, additional affected residues which are based on the transfer of recently published shift changes^[117] are indicated in pale green. The spatial position of the used α -helical peptides of BID, Bcl-XL and HK II are correspondingly highlighted in the entire protein structures (PDB-codes: 2bid, 1r2d, 1bg3). The broadened interaction sites of cBid and the HK II peptide partially extend across the C-terminal dimer interface of HVDAC1 (highlighted in red).

5.4.3 The channel wall as a signal transducing element

That in this processes the channel not only serves as an anchor point in the outer mitochondrial membrane, but also gets influenced by these interactions, becomes obvious by further distinct shift changes at the C-terminal end of the N-terminal α -helix and its connecting linker (Fig. 5-13). Since the N-terminal α -helix and its connecting linker are deeply buried in the hydrophilic pore of the channel, these changes are evidently induced by a structural movement of the adjacent barrel wall between β -strands 14 and 18 upon interaction with Bid, Bcl-XL or HK II. Thus, via the channel wall these proteins exert an influence on a region which in ScVDAC was unambiguously shown to be crucial for the selectivity and therefore for the conductance behaviour of the channel. Interestingly, although all of the interacting peptides target an identical region on HVDAC1, they exhibit almost no sequence similarity besides a basic or positively charged moiety which becomes deepest embedded into the membrane and obviously targets the highly conserved Asp residue within the PROSITE pattern. Due to the otherwise observed sequence discrepancy, it can be assumed that the binding modes along the observed interaction site of HVDAC1 vary slightly between the different peptides. Such a variation is also reflected by the different shift change patterns along the general interaction site of HVDAC1 (Fig. 5-13). The existence of varying binding modes might differentially influence the involved channel wall and therefore the transduction to selectivity influencing regions of the channel. As a consequence, the channel might alter its conductance behaviour in subjection to the nature of the interacting protein. However, due to the fact that the as crucial considered Bcl-2 homology domains of Bid and Bcl-XL are not involved in the interaction with the PROSITE pattern, it is rather unlikely that the observed interaction alone is sufficient for the opposite influence of the two antagonists on the integrity of the outer mitochondrial membrane. Nevertheless, the observed interaction might certainly function as a structural basis for further processes which finally control the permeability of the outer mitochondrial membrane. As such, the verified interaction might have a complex-stabilizing function as well as an influence on the targeting and the membrane insertion of Bid and Bcl-XL.

5.4.4 Influence of the oligomeric state of HVDAC1

Moreover, in case of Bid the interaction area extends towards the C-terminal end of the channel. Surprisingly, this part of the β -barrel is also important for dimer formation, as revealed by the HVDAC1 electron density (5-13).

Thus, the sites of homo- and hetero-oligomerisation overlap and the formation of the HVDAC1/Bid complex sterically blocks the dimerization of HVDAC1, as indeed observed by chemical crosslinking experiments (see Chap. 4.5.2). Since dimerisation seems to be necessary for the mutual stabilization of HVDAC1 monomers, the interaction with Bid should entail an enhanced flexibility of the channel which potentially favours the formation of membrane permeabilising complexes such as the permeability transition pore or an oligomeric pore complex of increased size.

6 References

- 1 Reichert A. S., Neupert W.: Mitochondriomics or what makes us breathe. *Trends Genet.* 2004, 20: 555-562.
- 2 Lill R., Kispal G.: Maturation of cellular Fe-S proteins: An essential function of mitochondria. *Trends Biochem. Sci.* 2000, 25: 352-356.
- 3 Vandecasteele G., Szabadkai G., Rizzuto R.: Mitochondrial calcium homeostasis: Mechanisms and molecules. *IUBMB Life* 2001, 52: 213-219.
- 4 Green D. R., Kroemer G.: The pathophysiology of mitochondrial cell death. *Science* 2004, 305: 626-629.
- 5 Trifunovic A.: Mitochondrial dna and ageing. *Biochim. Biophys. Acta* 2006, 1757: 611-617.
- 6 Wallace D.C.: Mitochondrial diseases in man and mouse. *Science* 1999, 283: 1482-1488.
- 7 Andersson S. G. E., Karlberg O., Canback B., Kurland C. G.: On the origin of mitochondria: A genomics perspective. *Philos. Trans. R. Soc. Lond., B, Biol. Sci.* 2003, 358: 165-77.
- 8 Dyall S.D., Brown M.T., Johnson P.J.: Ancient invasions: From endosymbionts to organelles. *Science* 2004, 304: 253-257.
- 9 Mannella C. A.: The relevance of mitochondrial membrane topology to mitochondrial function. *Biochim. Biophys. Acta.* 2006, 1762: 140-147.
- 10 Perkins G., Renken C., Martone M. E., Young S.J., Ellisman M., Frey T.: Electron tomography of neuronal mitochondria: Three-dimensional structure and organization of cristae and membrane contacts. *J. Struct. Biol.* 1997, 119: 260-272.
- 11 Lill R., Kispal G.: Mitochondrial ABC transporters. *Res. Microbiol.* 2001, 152: 331-340.
- 12 O'rourke B.: Mitochondrial ion channels. *Annu. Rev. Physiol.* 2007, 69: 19-49.
- 13 Palmieri L., Lasorsa F. M., Voza A., Agrimi G., Fiermonte G., Runswick M. J., Walker J. E., Palmieri F.: Identification and functions of new transporters in yeast mitochondria. *Biochim. Biophys. Acta.* 2000, 1459: 363-369.
- 14 Neupert W., Herrmann J.: Translocation of proteins into mitochondria. *Annu. Rev. Biochem.* 2007, 76: 723-749.
- 15 De Kroon A. L., Dolis D., Mayer A., Lill R., de Kruijff B.: Phospholipid composition of highly purified mitochondrial outer membranes of rat liver and *Neurospora crassa*. Is cardiolipin present in the mitochondrial outer membrane?. *Biochim. Biophys. Acta* 1997, 1325: 108-116.
- 16 Daum G.: Lipids of mitochondria. *Biochim. Biophys. Acta* 1985, 822: 1-42.
- 17 Tzagoloff A.: *Mitochondria*. Plenum Press, New York; 1982.
- 18 Schmitt S., Prokisch H., Schlunck T., Camp D. G., Ahting U., Waizenegger T., Scharfe C., Meitinger T., Imhof A., Neupert W., Oefner P. J., Rapaport D.: Proteome analysis of mitochondrial outer membrane from *Neurospora crassa*. *Proteomics* 2006, 6: 72-80.
- 19 Konstantinova S. A., Mannella C. A., Skulachev V. P., Zorov D. B.: Immunoelectron microscopic study of the distribution of porin on outer membranes of rat heart mitochondria. *J. Bioenerg. Biomembr.* 1995, 27: 93-99.
- 20 Goncalves R. P., Buzhynskyy N., Prima V., Sturgis J. N., Scheuring S.: Supramolecular assembly of VDAC in native mitochondrial outer membranes. *J. Mol. Biol.* 2007, 369: 413-418.
- 21 Parsons D.F., Williams G.R., Chance B.: Characteristics of isolated and purified preparations of the outer and inner membranes of mitochondria. *Ann. N. Y. Acad. Sci.* 1966, 137: 643-666.
- 22 Colombini M.: Candidate for the permeability pathway of the outer mitochondrial membrane. *Nature* 1979, 279: 643-645.
- 23 Lemasters J. J., Holmuhamedov E.: Voltage-dependent anion channel (VDAC) as mitochondrial governor - Thinking outside the box. *Biochim. Biophys. Acta* 2006, 1762: 181-190.
- 24 Ahting U., Thun C., Hegerl R., Typke D., Nargang F. E., Neupert W., Nussberger S.: The TOM core complex: The general protein import pore of the outer membrane of mitochondria. *J. Cell. Biol.* 1999, 147: 959-968.

- 25 Shoshan-Barmatz V., Israelson A., Brdiczka D., Sheu S. S.: The voltage-dependent anion channel (VDAC): Function in intracellular signalling, cell life and cell death. *Curr. Pharm. Des.* 2006, 12: 2249-2270.
- 26 Colombini M.: VDAC: The channel at the interface between mitochondria and the cytosol. *Mol. Cell. Biochem.* 2004, 256: 107-115.
- 27 Sampson M. J., Lovell R. S., Craigen W. J.: The murine voltage-dependent anion channel gene family. Conserved structure and function. *J. Biol. Chem.* 1997, 272: 18966-18973.
- 28 Benz R.: Structure and function of mitochondrial (eukaryotic) porins. WILEY-VCH GmbH & Co. KGaA, Weinheim; 2004.
- 29 Gellerich F. N., Schlame M., Bohnensack R., Kunz W.: Dynamic compartmentation of adenine nucleotides in the mitochondrial intermembrane space of rat-heart mitochondria. *Biochim. Biophys. Acta* 1987, 890: 117-126.
- 30 Cortese J. D., Voglino A. L., Hackenbrock C. R.: Ionic strength of the intermembrane space of intact mitochondria as estimated with fluorescein-BSA delivered by low pH fusion. *J. Cell. Biol.* 1991, 113: 1331-1340.
- 31 Porcelli A. M., Ghelli A., Zanna C., Pinton P., Rizzuto R., Rugolo M.: pH difference across the outer mitochondrial membrane measured with a green fluorescent protein mutant. *Biochem. Biophys. Res. Commun.* 2005, 326: 799-804.
- 32 Lemeshko V. V.: Theoretical evaluation of a possible nature of the outer membrane potential of mitochondria. *Eur. Biophys. J.* 2006, 36: 57-66.
- 33 Benz R., Wojtczak L., Bosch W., Brdiczka D.: Inhibition of adenine nucleotide transport through the mitochondrial porin by a synthetic polyanion. *FEBS Lett.* 1988, 231: 75-80.
- 34 Zizi M., Forte M., Blachly-Dyson E., Colombini M.: NADH regulates the gating of VDAC, the mitochondrial outer membrane channel. *J. Biol. Chem.* 1994, 269: 1614-1616.
- 35 Mangan P. S., Colombini M.: Ultrasteep voltage dependence in a membrane channel. *Proc. Natl. Acad. Sci.* 1987, 84: 4896-4900.
- 36 Lee A.C., Xu X., Colombini M.: The role of pyridine dinucleotides in regulating the permeability of the mitochondrial outer membrane. *J. Biol. Chem.* 1996, 271: 26724-26731.
- 37 Zimmerberg J., Parsegian V. A.: Polymer inaccessible volume changes during opening and closing of a voltage-dependent ionic channel. *Nature* 1986, 323:36-39.
- 38 Mannella C. A.: Minireview: On the structure and gating mechanism of the mitochondrial channel, VDAC. *J. Bioenerg. Biomembr.* 1997, 29: 525-531.
- 39 Guo X. W., Smith P. R., Cognon B., D'Arcangelis D., Dolginova E., Mannella C. A.: Molecular design of voltage-dependent, anion-selective channel in the mitochondrial outer membrane. *J. Struct. Biol.* 1995, 114: 41-59.
- 40 Dolder M., Zeth K., Tittmann P., Gross H., Welte W., Wallimann T.: Crystallization of the human, mitochondrial voltage-dependent anion-selective channel in the presence of phospholipids. *J. Struct. Biol.* 1999, 127: 64-71.
- 41 Thomas L., Kocsis E., Colombini M., Erbe E., Trus B. L., Steven A.C.: Surface topography and molecular stoichiometry of the mitochondrial channel, VDAC, in crystalline arrays. *J. Struct. Biol.* 1991, 106: 161-171.
- 42 Young M., Bay D., Hausner G., Court D.: The evolutionary history of mitochondrial porins. *BMC Evol. Biol.* 2007, 7:31.
- 43 Peng S., Blachly-Dyson E., Colombini M., Forte M.: Determination of the number of polypeptide subunits in a functional VDAC channel from *Saccharomyces cerevisiae*. *J. Bioenerg. Biomembr.* 1992, 24: 27-31.
- 44 Wimley W.C.: The versatile beta-barrel membrane protein. *Curr. Opin. Struct. Biol.* 2003, 13: 404-411.
- 45 Koebnik R., Locher K.P., Van Gelder P.: Structure and function of bacterial outer membrane proteins: Barrels in a nutshell. *Mol. Microbiol.* 2000, 37: 239-253.
- 46 Snijder H. J., Ubarretxena-Belandia I., Blaauw M., Kalk K. H., Verheij H. M., Egmond M. R., Dekker N., Dijkstra B.W.: Structural evidence for dimerization-regulated activation of an integral membrane phospholipase. *Nature* 1999, 401: 717-721.

- 47 Schulz G. E.: The structure of bacterial outer membrane proteins. *Biochim. Biophys. Acta* 2002, 1565: 308-317.
- 48 Dong C., Beis K., Nesper J., Brunkan-Lamontagne A. L., Clarke B. R., Whitfield C., Naismith J. H.: Wza the translocon for *E. coli* capsular polysaccharides defines a new class of membrane protein. *Nature* 2006, 444: 226-229.
- 49 Schulz G.E.: Transmembrane beta-barrel proteins. *Adv. Protein Chem.* 2003, 63: 47-70.
- 50 Abrecht H., Goormaghtigh E., Ruyschaert J. M., Homble F.: Structure and orientation of two voltage-dependent anion-selective channel isoforms. An attenuated total reflection fourier-transform infrared spectroscopy study. *J. Biol. Chem.* 2000, 275: 40992-40999.
- 51 Ahting U., Thieffry M., Engelhardt H., Hegerl R., Neupert W., Nussberger S.: Tom40, the pore-forming component of the protein-conducting TOM channel in the outer membrane of mitochondria. *J. Cell. Biol.* 2001, 153: 1151-1160.
- 52 Shao L., Kinnally K.W., Mannella C. A.: Circular dichroism studies of the mitochondrial channel, VDAC, from *Neurospora crassa*. *Biophys. J.* 1996, 71: 778-786.
- 53 Shi Y., Jiang C., Chen Q., Tang H.: One-step on-column affinity refolding purification and functional analysis of recombinant human VDAC1. *Biochem. Biophys. Res. Commun.* 2003, 303: 475-482.
- 54 Koppel D.A., Kinnally K.W., Masters P., Forte M., Blachly-Dyson E., Mannella C.A.: Bacterial expression and characterization of the mitochondrial outer membrane channel. Effects of N-terminal modifications. *J. Biol. Chem.* 1998, 273: 13794-13800.
- 55 Engelhardt H., Meins T., Poynor M., Adams V., Nussberger S., Welte W., Zeth K.: High-level expression, refolding and probing the natural fold of the human voltage-dependent anion channel isoforms I and II. *J. Membr. Biol.* 2007, 216(2-3): 93-105.
- 56 Blachly-Dyson E., Peng S., Colombini M., Forte M.: Selectivity changes in site-directed mutants of the VDAC ion channel: Structural implications. *Science* 1990, 247: 1233-1236.
- 57 Song J., Midson C., Blachly-Dyson E., Forte M., Colombini M.: The sensor regions of VDAC are translocated from within the membrane to the surface during the gating processes. *Biophys. J.* 1998, 74: 2926-2944.
- 58 Blachly-Dyson E., Peng S. Z., Colombini M., Forte M.: Probing the structure of the mitochondrial channel, VDAC, by site-directed mutagenesis: A progress report. *J. Bioenerg. Biomembr.* 1989, 21: 471-483.
- 59 Song J., Midson C., Blachly-Dyson E., Forte M., Colombini M.: The topology of VDAC as probed by biotin modification. *J. Biol. Chem.* 1998, 273: 24406-24413.
- 60 Rostovtseva T.K., Tan W., Colombini M.: On the role of VDAC in apoptosis: Fact and fiction. *J. Bioenerg. Biomembr.* 2005, 37: 129-142.
- 61 Bay D. C., Court D. A.: Origami in the outer membrane: the transmembrane arrangement of mitochondrial porins. *Biochem Cell. Biol.* 2002, 80: 551-562.
- 62 Guo X. W., Mannella C. A.: Conformational change in the mitochondrial channel, VDAC, detected by electron cryo-microscopy. *Biophys. J.* 1993, 64: 545-549.
- 63 Casadio R., Jacoboni I., Messina A., De Pinto V.: A 3D model of the voltage-dependent anion channel (VDAC). *FEBS Lett* 2002, 520: 1-7.
- 64 Rauch G., Moran O.: On the structure of mitochondrial porins and its homologies with bacterial porins. *Biochem. Biophys. Res. Commun.* 1994, 200: 908-915.
- 65 Forte M., Guy H. R., Mannella C. A.: Molecular genetics of the VDAC ion channel: Structural model and sequence analysis. *J. Bioenerg. Biomembr.* 1987, 19: 341-350.
- 66 Mannella C. A.: Conformational changes in the mitochondrial channel protein, VDAC, and their functional implications. *J. Struct. Biol.* 1998, 121: 207-218.
- 67 Mannella C. A., Guo X. W.: Interaction between the VDAC channel and a polyanionic effector. An electron microscopic study. *Biophys. J.* 1990, 57: 23-31.
- 68 Popp B., Court D. A., Benz R., Neupert W., Lill R.: The role of the N and C termini of recombinant *Neurospora* mitochondrial porin in channel formation and voltage-dependent gating. *J. Biol. Chem.* 1996, 271: 13593-13599.

- 69 Shoshan-Barmatz V., Gincel D.: The voltage-dependent anion channel: Characterization, modulation, and role in mitochondrial function in cell life and death. *Cell. Biochem. Biophys.* 2003, 39: 279-292.
- 70 Fiek C., Benz R., Roos N., Brdiczka D.: Evidence for identity between the hexokinase-binding protein and the mitochondrial porin in the outer membrane of rat liver mitochondria. *Biochim. Biophys. Acta.* 1982, 688: 429-440.
- 71 Linden M., Gellerfors P., Nelson B.D.: Pore protein and the hexokinase-binding protein from the outer membrane of rat liver mitochondria are identical. *FEBS Lett.* 1982, 141: 189-192.
- 72 Ostlund A.K., Gohring U., Krause J., Brdiczka D.: The binding of glycerol kinase to the outer membrane of rat liver mitochondria: Its importance in metabolic regulation. *Biochem. Med.* 1983, 30: 231-245.
- 73 Beutner G., Ruck A., Riede B., Welte W., Brdiczka D.: Complexes between kinases, mitochondrial porin and adenylate translocator in rat brain resemble the permeability transition pore. *FEBS Lett.* 1996, 396: 189-195.
- 74 Vyssokikh M., Brdiczka D.: VDAC and peripheral channelling complexes in health and disease. *Mol. Cell. Biochem.* 2004, 256-257: 117-126.
- 75 Wallimann T., Wyss M., Brdiczka D., Nicolay K., Eppenberger H. M.: Intracellular compartmentation, structure and function of creatine kinase isoenzymes in tissues with high and fluctuating energy demands: The 'phosphocreatine circuit' for cellular energy homeostasis. *Biochem. J.* 1992, 281: 21-40.
- 76 Brdiczka D., Kaldis P., Wallimann T.: In vitro complex formation between the octamer of mitochondrial creatine kinase and porin. *J. Biol. Chem.* 1994, 269: 27640-27644.
- 77 Saelens X., Festjens N., Vande Walle L., van Gorp M., van Loo G., Vandenabeele P.: Toxic proteins released from mitochondria in cell death. *Oncogene* 2004, 23: 2861-2874.
- 78 Li P., Nijhawan D., Budihardjo I., Srinivasula S. M., Ahmad M., Alnemri E. S., Wang X.: Cytochrome c and dATP-dependent formation of Apaf-1/caspase-9 complex initiates an apoptotic protease cascade. *Cell* 1997, 91: 479-489.
- 79 Kroemer G., Galluzzi L., Brenner C.: Mitochondrial membrane permeabilization in cell death. *Physiol. Rev.* 2007, 87: 99-163.
- 80 Shimizu S., Narita M., Tsujimoto Y.: Bcl-2 family proteins regulate the release of apoptogenic cytochrome c by the mitochondrial channel VDAC. *Nature* 1999, 399:483-487.
- 81 Rostovtseva T. K., Antonsson B., Suzuki M., Youle R. J., Colombini M., Bezrukov S. M.: Bid, but not Bax, regulates VDAC channels. *J. Biol. Chem.* 2004, 279: 13575-13583.
- 82 Vander Heiden M. G., Li X. X., Gottlieb E., Hill R. B., Thompson C. B., Colombini M.: Bcl-XL promotes the open configuration of the voltage-dependent anion channel and metabolite passage through the outer mitochondrial membrane. *J. Biol. Chem.* 2001, 276: 19414-19419.
- 83 Crompton M., Barksby E., Johnson N., Capano M.: Mitochondrial intermembrane junctional complexes and their involvement in cell death. *Biochimie* 2002, 84: 143-152.
- 84 Brenner C., Grimm S.: The permeability transition pore complex in cancer cell death. *Oncogene* 2006, 25: 4744-4756.
- 85 Kuwana T., Mackey M. R., Perkins G., Ellisman M. H., Latterich M., Schneider R., Green D. R., Newmeyer D. D.: Bid, Bax, and lipids cooperate to form supramolecular openings in the outer mitochondrial membrane. *Cell* 2002, 111:331-342.
- 86 Desagher S., Osen-Sand A., Nichols A., Eskes R., Montessuit S., Lauper S., Maundrell K., Antonsson B., Martinou J. C.: Bid-induced conformational change of Bax is responsible for mitochondrial cytochrome c release during apoptosis. *J Cell Biol* 1999, 144:891-901.
- 87 Patzelt H., Ulrich A. S., Egbringhoff H., Dux P., Ashurst J., Simon B., Oschkinat H., Oesterheld D.,: Towards structural investigations on isotope labelled native bacteriorhodopsin in detergent micelles by solution-state NMR spectroscopy. *J. Biomol. NMR* 1997, 10: 95-106.
- 88 Van Duyne G. D., Standaert R. F., Karplus P. A., Schreiber S. L., Clardy J.: Atomic structures of the human immunophilin Fkbp-12 complexes with Fk506 and rapamycin. *J. Mol. Biol.* 1993, 229: 105-124.
- 89 Antonsson B., Montessuit S., Sanchez B., Martinou J. C.: Bax is present as a high molecular weight oligomer/complex in the mitochondrial membrane of apoptotic cells. *J. Biol. Chem.* 2001, 276: 11615-11623.

- 90 Clarke S.: A major polypeptide component of rat liver mitochondria: Carbamyl phosphate synthetase. *J. Biol. Chem.* 1976, 251: 950-961.
- 91 Benz R., Brdiczka D.: The cation-selective substate of the mitochondrial outer membrane pore: Single-channel conductance and influence on intermembrane and peripheral kinases. *J. Bioenerg. Biomembr.* 1992, 24: 33-39.
- 92 Fancy D.A., Kodadek T.: Chemistry for the analysis of protein-protein interactions: Rapid and efficient cross-linking triggered by long wavelength light. *Proc. Natl. Acad. Sci.* 1999, 96: 6020-6024.
- 93 Bayrhuber M.: Structural and functional characterisation of the mitochondrial membrane protein human voltage-dependent anion channel (HVDAC) and the membrane protein-targeting conotoxin conkunitzin-S1 by solution NMR. *PhD thesis*. Mathematisch-Naturwissenschaftliche Fakultäten der Georg-August-Universität zu Göttingen, 2007.
- 94 Zhu G., Kong X. M., Sze K. H.: Gradient and sensitivity enhancement of 2D TROSY with water flip-back, 3D NOESY-TROSY and TOCSY-TROSY experiments. *J. Biomol. NMR* 1999, 13: 77-81.
- 95 Ying J. F., Chill J. H., Louis J. M., Bax A.: Mixed-time parallel evolution in multiple quantum NMR experiments: Sensitivity and resolution enhancement in heteronuclear NMR. *J. Biomol. NMR* 2007, 37: 195-204.
- 96 Zhu G., Xia Y. L., Nicholson L. K., Sze K. H.: Protein dynamics measurements by TROSY-based NMR experiments. *J. Magn. Reson.* 2000, 143: 423-426.
- 97 Delaglio F., Grzesiek S., Vuister G. W., Zhu G., Pfeifer J., Bax A.: NMRPipe - A multidimensional spectral processing system based on UNIX pipes. *J. Biomol. NMR* 1995, 6: 277-293.
- 98 Arndt U. W., Wonacott A. J.: *The rotation method in crystallography*. North-Holland Publishers, Amsterdam; 1977.
- 99 Leslie A. G. W.: Recent changes to the Mosflm package for processing film and image plate data. *Joint CCP4 and ESF-EACBM Newsletter on Protein Crystallography* 1992, 26.
- 100 Kabsch W.: Automatic processing of rotation diffraction data from crystals of initially unknown symmetry and cell constants. *J. Appl. Cryst.* 1993, 26: 795-800.
- 101 Pflugrath J. W.: The finer things in X-ray diffraction data collection. *Acta Crystallogr. D Biol. Crystallogr.* 1999, 55: 1718-1725.
- 102 Evans P. R.: Scala. *Joint CCP4 and ESF-EACBM Newsletter on Protein Crystallography* 1997, 33: 22-24.
- 103 Schneider T. R., Sheldrick G. M.: Substructure solution with SHELXD. *Acta Crystallogr. D Biol. Crystallogr.* 2002, 58: 1772-1779.
- 104 Bricogne G., Vornrhein C., Flensburg C., Schiltz M., Paciorek W.: Generation, representation and flow of phase information in structure determination: Recent developments in and around Sharp 2.0. *Acta Crystallogr. D Biol. Crystallogr.* 2003, 59: 2023-2030.
- 105 Abrahams J. P., Leslie A. G.: Methods used in the structure determination of bovine mitochondrial F1-ATPase. *Acta Crystallogr. D Biol. Crystallogr.* 1996, 52: 30-42.
- 106 Cowtan K.: 'DM' an automated procedure for phase improvement by density modification. *Joint CCP4 and ESF-EACBM Newsletter on Protein Crystallography* 1994, 31: 34-38.
- 107 DeLaBarre B., Brunger A. T.: Considerations for the refinement of low-resolution crystal structures. *Acta Crystallogr. D Biol. Crystallogr.* 2006, 62: 923-932.
- 108 Vagin, A Teplyakov, A: MOLREP: An automated program for molecular replacement. *J. Appl. Cryst.* 1997, 30: 1022-1025.
- 109 Jones T. A., Zou J. Y., Cowan S. W., Kjeldgaard M.: Improved methods for building protein models in electron density maps and the location of errors in these models. *Acta Crystallogr. A* 1991, 47: 110-119.
- 110 Emsley P., Cowtan K.: Coot: Model-building tools for molecular graphics. *Acta Crystallogr. D Biol. Crystallogr.* 2004, 60: 2126-2132.
- 111 Edgar R. C.: Muscle: A multiple sequence alignment method with reduced time and space complexity. *BMC Bioinformatics* 2004, 5: 113.
- 112 Herrmann K.: Non-ionic-cationic micellar properties of dimethyldodecylamine oxide. *J. Phys. Chem.* 1962, 66: 295-300.

- 113 Bax A., Grzesiek S.: Methodological advances in protein NMR. *Acc. Chem. Res.* 1993, 26: 131-138
- 114 Metzler W. J., Constantine K. L., Friedrichs M. S., Bell A. J., Ernst E. G., Lavoie T. B., Mueller L.: Characterization of the three-dimensional solution structure of human profilin: ^1H , ^{13}C , and ^{15}N NMR assignments and global folding pattern. *Biochemistry* 1993, 32: 13818-13829.
- 115 McLachlan A. D.: Gene duplications in the structural evolution of chymotrypsin. *J. Mol. Biol.* 1979, 128: 49-79.
- 116 Wang K., Yin X. M., Chao D. T., Milliman C. L., Korsmeyer S. J.: Bid: A novel BH3 domain-only death agonist. *Genes Dev* 1996, 10: 2859-2869.
- 117 Malia T. J., Wagner G.: NMR structural investigation of the mitochondrial outer membrane protein VDAC and its interaction with antiapoptotic Bcl-XL. *Biochemistry* 2007, 46: 514-525.
- 118 Chou J. J., Li H., Salvesen G. S., Yuan J., Wagner G.: Solution structure of Bid, an intracellular amplifier of apoptotic signaling. *Cell* 1999, 96: 615-624.
- 119 Kuwana T., Newmeyer D. D.: Bcl-2-family proteins and the role of mitochondria in apoptosis. *Curr. Opin. Cell. Biol.* 2003, 15: 691-699.
- 120 Nakashima R. A.: Hexokinase-binding properties of the mitochondrial VDAC protein: Inhibition by DCCD and location of putative DCCD-binding sites. *J. Bioenerg. Biomembr.* 1989, 21: 461-470.
- 121 Finney K. G., Messer J. L., DeWitt D. L., Wilson J. E.: Monoclonal antibodies against rat brain hexokinase. Effects on catalytic function and binding to the outer mitochondrial membrane. *J. Biol. Chem.* 1984, 259: 8232-8237.
- 122 Polakis P. G., Wilson J. E.: An intact hydrophobic N-terminal sequence is critical for binding of rat brain hexokinase to mitochondria. *Arch. Biochem. Biophys.* 1985, 236: 328-337.
- 123 Thinnes F. P.: Does fluoxetine (PROZAK) block mitochondrial permeability transition by blocking VDAC as part of permeability transition pores?. *Mol. Genet. Metab.* 2005, 84: 378.
- 124 Israelson A., Abu-Hamad S., Zaid H., Nahon E., Shoshan-Barmatz V.: Localization of the voltage-dependent anion channel-1 Ca^{2+} -binding sites. *Cell Calcium* 2007, 41: 235-244.
- 125 Gincel D., Zaid H., Shoshan-Barmatz V.: Calcium binding and translocation by the voltage-dependent anion channel: A possible regulatory mechanism in mitochondrial function. *Biochem. J.* 2001, 358: 147-155.
- 126 Mannella C. A.: Phospholipase-induced crystallization of channels in mitochondrial outer membranes. *Science* 1984, 224: 165-166.
- 127 Mannella C. A.: Electron microscopy and image analysis of the mitochondrial outer membrane channel, VDAC. *J. Bioenerg. Biomembr.* 1987, 19: 329-340.
- 128 Shanmugavadivu B., Apell H., Meins T., Zeth K., Kleinschmidt J. H.: Correct folding of the beta-barrel of the human membrane protein VDAC requires a lipid bilayer. *J. Mol. Biol.* 2007, 368: 66-78.
- 129 De Pinto V., Ludwig O., Krause J., Benz R., Palmieri F.: Porin pores of mitochondrial outer membranes from high and low eukaryotic cells: Biochemical and biophysical characterization. *Biochim. Biophys. Acta* 1987, 894: 109-119.
- 130 Fernandez C., Hilty C., Wider G., Guntert P., Wuthrich K.: NMR structure of the integral membrane protein OmpX. *J. Mol. Biol.* 2004, 336: 1211-1221.
- 131 Arora A, Abildgaard F, Bushweller JH, Tamm LK: Structure of outer membrane protein a transmembrane domain by NMR spectroscopy. *Nat. Struct. Biol.* 2001, 8: 334-338.
- 132 Hwang P. M., Choy W., Lo E. L., Chen L., Forman-Kay J. D., Raetz C. R. H., Prive G. G., Bishop R. E., Kay L.E.: Solution structure and dynamics of the outer membrane enzyme PagP by NMR. *Proc. Natl. Acad. Sci.* 2002, 99: 13560-13565.
- 133 Kainosho M., Torizawa T., Iwashita Y., Terauchi T., Mei Ono A, Guntert P.: Optimal isotope labelling for NMR protein structure determinations. *Nature* 2006, 440: 52-57.
- 134 Thomas L., Blachly-Dyson E., Colombini M., Forte M.: Mapping of residues forming the voltage sensor of the voltage-dependent anion-selective channel. *Proc. Natl. Acad. Sci.* 1993, 90: 5446-5449.
- 135 Ostermeier C., Michel H.: Crystallization of membrane proteins. *Curr. Opin. Struct. Biol.* 1997, 7: 697-701.

- 136 De Pinto V. D., Palmieri F.: Transmembrane arrangement of mitochondrial porin or voltage-dependent anion channel (VDAC). *J. Bioenerg. Biomembr.* 1992, 24: 21-26.
- 137 Mannella C. A., Forte M., Colombini M.: Toward the molecular structure of the mitochondrial channel, VDAC. *J. Bioenerg. Biomembr.* 1992, 24: 7-19.
- 138 Blachly-Dyson E., Zambronicz E. B., Yu W. H., Adams V., McCabe E. R., Adelman J., Colombini M., Forte M.: Cloning and functional expression in yeast of two human isoforms of the outer mitochondrial membrane channel, the voltage-dependent anion channel. *J. Biol. Chem.* 1993, 268: 1835-1841.
- 139 Blumenthal A., Kahn K., Beja O., Galun E., Colombini M., Breiman A.: Purification and characterization of the voltage-dependent anion-selective channel protein from wheat mitochondrial membranes. *Plant. Physiol.* 1993, 101: 579-587.
- 140 Elkeles A., Breiman A., Zizi M.: Functional differences among wheat voltage-dependent anion channel (VDAC) isoforms expressed in yeast. Indication for the presence of a novel VDAC-modulating protein?. *J. Biol. Chem.* 1997, 272: 6252-6260.
- 141 Biswas S., Mohammad M. M., Patel D. R., Movileanu L., van den Berg B.: Structural insight into OprD substrate specificity. *Nat. Struct. Mol. Biol.* 2007, 14: 1108-1109.
- 142 Hulo N., Bairoch A., Bulliard V., Cerutti L., Cuche B., Castro E., Lachaize C., Langendijk-Genevaux P., Sigrist C.: The 20 years of Prosite. *Nucleic. Acids. Res.* 2007, 36: D245-249.
- 143 De Pinto V., Tomasello F., Messina A., Guarino F., Benz R., La Mendola D., Magri A., Milardi D., Pappalardo G.: Determination of the conformation of the human VDAC1 N-terminal peptide, a protein moiety essential for the functional properties of the pore. *ChemBiochem.* 2007, 8: 744-756.
- 144 Marques E. J., Carneiro C. M., Silva A. S., Krasilnikov O. V.: Does VDAC insert into membranes in random orientation?. *Biochim. Biophys. Acta* 2004, 1661: 68-77.
- 145 Stanley S., Dias J. A., D'Arcangelis D., Mannella C. A.: Peptide-specific antibodies as probes of the topography of the voltage-gated channel in the mitochondrial outer membrane of *Neurospora crassa*. *J. Biol. Chem.* 1995, 270: 16694-16700.
- 146 Lomize A. L., Pogozheva I. D., Lomize M. A., Mosberg H. I.: Positioning of proteins in membranes: A computational approach. *Protein Sci.* 2006, 15: 1318-1333.
- 147 Jackups R. J., Liang J.: Interstrand pairing patterns in beta-barrel membrane proteins: The positive-outside rule, aromatic rescue, and strand registration prediction. *J. Mol. Biol.* 2005, 354: 979-993.
- 148 Zeth K., Diederichs K., Welte W., Engelhardt H.: Crystal structure of Omp32, the anion-selective porin from *comamonas acidovorans*, in complex with a periplasmic peptide at 2.1 Å resolution. *Structure* 2000, 8: 981-992.
- 149 Ferguson A. D., Hofmann E., Coulton J. W., Diederichs K., Welte W.: Siderophore-mediated iron transport: Crystal structure of FhuA with bound lipopolysaccharide. *Science* 1998, 282: 2215-2220.
- 150 Oomen C. J., van Ulsen P., van Gelder P., Feijen M., Tommassen J., Gros P.: Structure of the translocator domain of a bacterial autotransporter. *EMBO J.* 2004, 23: 1257-1266.
- 151 Clantin B., Delattre A., Rucktooa P., Saint N., Meli A. C., Loch C., Jacob-Dubuisson F., Villeret V.: Structure of the membrane protein FhaC: A member of the Omp85-TpsB transporter superfamily. *Science* 2007, 317: 957-961.
- 152 Ahn V. E., Lo E. I., Engel C. K., Chen L., Hwang P. M., Kay L. E., Bishop R. E., Prive G. G.: A hydrocarbon ruler measures palmitate in the enzymatic acylation of endotoxin. *EMBO J* 2004, 23: 2931-2941.
- 153 Schindler H., Rosenbusch J. P.: Matrix protein from *Escherichia coli* outer membranes forms voltage-controlled channels in lipid bilayers. *Proc. Natl. Acad. Sci.* 1978, 75: 3751-3755.
- 154 Phale P. S., Schirmer T., Prilipov A., Lou K. L., Hardmeyer A., Rosenbusch J. P.: Voltage gating of *Escherichia coli* porin channels: Role of the constriction loop. *Proc. Natl. Acad. Sci.* 1997, 94: 6741-6745.
- 155 Schirmer T., Keller T. A., Wang Y. F., Rosenbusch J. P.: Structural basis for sugar translocation through maltoporin channels at 3.1 Å resolution. *Science* 1995, 267: 512-514.
- 156 Forst D., Welte W., Wacker T., Diederichs K.: Structure of the sucrose-specific porin ScrY from salmonella typhimurium and its complex with sucrose. *Nat. Struct. Biol.* 1998, 5: 37-46.

- 157 Hirsch A., Breed J., Saxena K., Richter O. M., Ludwig B., Diederichs K., Welte W.: The structure of porin from *Paracoccus denitrificans* at 3.1 Å resolution. *FEBS Lett.* 1997, 404: 208-210.
- 158 Zalk R., Israelson A., Garty E. S., Azoulay-Zohar H., Shoshan-Barmatz V.: Oligomeric states of the voltage-dependent anion channel and cytochrome c release from mitochondria. *Biochem. J.* 2005, 386: 73-83.
- 159 Vander Heiden M. G., Chandel N. S., Li X. X., Schumacker P. T., Colombini M., Thompson C. B.: Outer mitochondrial membrane permeability can regulate coupled respiration and cell survival. *Proc. Natl. Acad. Sci.* 2000, 97: 4666-4671.
- 160 Gottlob K., Majewski N., Kennedy S., Kandel E., Robey R. B., Hay N.: Inhibition of early apoptotic events by Akt/Pkb is dependent on the first committed step of glycolysis and mitochondrial hexokinase. *Genes Dev.* 2001, 15: 1406-1418.
- 161 Pastorino J. G., Shulga N., Hoek J. B.: Mitochondrial binding of hexokinase II inhibits Bax-induced cytochrome c release and apoptosis. *J. Biol. Chem.* 2002, 277: 7610-7618.
- 162 Xie G. C., Wilson J. E.: Rat brain hexokinase: The hydrophobic N-terminus of the mitochondrially bound enzyme is inserted in the lipid bilayer. *Arch. Biochem. Biophys.* 1988, 267: 803-810.
- 163 Azoulay-Zohar H., Israelson A., Abu-Hamad S., Shoshan-Barmatz V.: In self-defence: Hexokinase promotes voltage-dependent anion channel closure and prevents mitochondria-mediated apoptotic cell death. *Biochem. J.* 2004, 377: 347-355.
- 164 Martinou J. C., Green D. R.: Breaking the mitochondrial barrier. *Nat. Rev. Mol. Cell. Biol.* 2001, 2: 63-67.
- 165 McDonnell J. M., Fushman D., Milliman C. L., Korsmeyer S. J., Cowburn D.: Solution structure of the proapoptotic molecule Bid: A structural basis for apoptotic agonists and antagonists. *Cell* 1999, 96: 625-634.
- 166 Muchmore S. W., Sattler M., Liang H., Meadows R. P., Harlan J. E., Yoon H. S., Nettlesheim D., Chang B. S., Thompson C. B., Wong S. L., Ng S. L., Fesik S. W.: X-ray and NMR structure of human Bcl-XL, an inhibitor of programmed cell death. *Nature* 1996, 381: 335-341.
- 167 Franzin C. M., Choi J., Zhai D., Reed J. C., Marassi F. M.: Structural studies of apoptosis and ion transport regulatory proteins in membranes. *Magn. Reson. Chem.* 2004, 42: 172-179.
- 168 Garcia-Saez A. J., Mingarro I., Perez-Paya E., Salgado J.: Membrane-insertion fragments of Bcl-XL, Bax, and Bid. *Biochemistry* 2004, 43: 10930-10943.
- 169 Kim P. K., Annis M. G., Dlugosz P. J., Leber B., Andrews D. W.: During apoptosis Bcl-2 changes membrane topology at both the endoplasmic reticulum and mitochondria. *Mol. Cell.* 2004, 14: 523-529.
- 170 Losonczi J. A., Olejniczak E. T., Betz S. F., Harlan J. E., Mack J., Fesik S. W.: NMR studies of the anti-apoptotic protein Bcl-XL in micelles. *Biochemistry* 2000, 39: 11024-11033.
- 171 Mulchak A. M., Wilson J. E., Padmanabhan K., Garavito R. M.: The structure of mammalian hexokinase-1. *Nat. Struct. Biol.* 1998, 5: 555-560.
- 172 Abu-Hamad S., Zaid H., Israelson A., Nahon E., Shoshan-Barmatz V.: Hexokinase-I protection against apoptotic cell death is mediated via interaction with the voltage-dependent anion channel-1: Mapping the site of binding. *J. Biol. Chem.* 2008, 283(19): 13482-90.

7 Abbreviations

Å	angstrom
AES-media	algal extract supplemented media
ANT	adenine nucleotide translocator
ATR-FTIR	attenuated total reflection fourier transform infrared spectroscopy
AU	adsorption units
Bax	Bcl2 associated protein X
Bcl-2	B cell lymphoma protein number 2
Bid	BH3 interacting domain death agonist
CD	circular dichroism
CMC	critical micellar concentration
DMSO	dimethylsulfoxide
DTT	dithiothreitol
<i>E. coli</i>	<i>Escherichia coli</i>
EM	Electron microscopy
ESRF	european synchrotron facility
F _{calc}	calculated structure factor computed from the model
F _{obs}	observed structure factor from recorded diffraction pattern
G	conductance
HK	hexokinase
HSQC	heteronuclear single quantum coherence
HVDAC1	human voltage dependent anion channel isoform I;
IMM	inner mitochondrial membrane
IMS	inter membrane space;
IPTG	isopropyl-beta-D-thiogalactopyranoside
LB-medium	Luria Broth
M9-media	minimal media
MAD	multiple wavelength anomalous diffraction
MIMS	mitochondrial inter-membrane space
MOM	mitochondrial outer membrane;
MOMP	mitochondrial outer membrane permeabilization
MTSL	(1-oxy-2,2,5,5-tetramethyl-D-pyrroline-3-methyl)-methanethiosulfonate
NMR	nuclear magnetic resonance
<i>nS</i>	nano Siemens
OMM	outer mitochondrial membrane
Omp	outer membrane protein
PDB	protein data base
PMSF	phenylmethylsulphonylfluoride
PRE	paramagnetic relaxation enhancement
PTPC	permeability transition pore complex;
Rmsd	root mean square deviation
RT	room temperature
RuR	Tris(bipyridyl)-ruthenium(II)dichlorid
SAD	single wavelength anomalous diffraction
SAM	sorting and assembly machinery
SDS	sodium dodecyl sulfate
SDS-PAGE	sodium dodecylsulfate polyacrylamide gel electrophoresis
SeMet	seleno-methionine
SLS	swiss light source
TB-medium	terrific broth
TEMED	N,N,N',N'-tetramethylethylenediamine
TFA	trifluoroacetic acid
Tris-HCl	tris (hydroxymethyl) aminomethane hydrochloride
TROSY	transverse relaxation optimized spectroscopy

8 Acknowledgement

I am deeply grateful to the head of the department Prof. Dr. Dieter Oesterhelt for the opportunity to do my Ph.D. in his department, which provided an excellent scientific environment with an outstanding equipment and exceptional scientists, and of course for his encouragement and useful remarks.

I am sincerely grateful to my direct supervisor Dr. Kornelius Zeth for the design of this project, his stimulating suggestions, continuous support and advice.

I owe my most sincere gratitude to Dr. Monika Bayrhuber and her supervisors Dr. Markus Zweckstetter and Prof. Dr. Christian Griesinger from the Max Planck Institute for Biophysical Chemistry in Göttingen for the most productive collaboration on the HVDAC1 project during the last four years. Without the irrepressible optimism and continuing tenacity of Dr. Monika Bayrhuber the NMR part of this work would have been impossible.

I would like to express my deep and sincere gratitude to Dr. Clemens Vornrhein from Global Phasing Ltd. Cambridge, UK for his patience and continuing crucial help regarding the crystallographic work on HVDAC1.

I am deeply and sincerely grateful to Christl Weyrauch for her excellent support, her understanding, patience, and most importantly, her friendship over the years.

I owe gratitude to Dr. Melissa Poynor and Prof. Dr. Stefan Nussberger from the University of Stuttgart and Elisabeth Weyher-Stingl and Reinhard Mentele from the MPI of Biochemistry for their help and excellent support during conductance measurements, CD spectroscopy and mass spectrometry.

I like to sincerely thank Brigitte Kessler for training me in the production of selectively labeled samples for NMR measurements.

My deep and warm thanks go to Dr. Martin Grininger, Dr. Patrik Johannson and Dr. Wilfried Staudinger for many valuable suggestions and the time they spent in my favor to read this manuscript.

I would like to thank Verena for her support, encouragement and quiet patience and that she was always there for me.

Finally I want to thank my family which provided me with unending encouragement, loving care and support which gave me the strength to finish this thesis.

Lebenslauf

Persönliche Daten

Name: Thomas Wilhelm MEINS
Geburtsdatum: 01. Oktober 1973
Geburtsort: München
Staatsangehörigkeit: deutsch

Ausbildung

1980-1984 Grundschule Pürgen
1984-1985 Teilhauptschule I Landsberg/Lech
1985-1995 Dominikus Zimmermann Gymnasium Landsberg/Lech
1995-1996 Grundwehrdienst LwAusbRgt 3 Roth, LTG 61 Penzing
1996-2002 Studium der Biologie an der Universität Bayreuth
Diplomarbeit mit dem Titel "*Acetyl-CoA Synthase aus Carboxidotherrmus hydrogenoformans*" am Lehrstuhl für Mikrobiologie unter der Betreuung von Prof. Dr. Ortwin Meyer
2003-2007 Max-Planck-Institut für Biochemie, Martinsried
Doktorarbeit mit dem Titel "Structural basis of the mitochondrial voltage-dependent anion channel VDAC I" in der Abteilung für Membranbiochemie unter der Betreuung von Prof. Dr. Dieter Oesterhelt
seit 09/2007 Sanofi-Aventis R&D, Vitry sur Seine (Frankreich)

München, am 08. September 2008

.....
Thomas Meins

